ELECTRIC TAXIING - POWER SYSTEM ANALYSIS

ON THE CONCEPT OF ELECTRIC TAXIING FOR MIDSIZE COMMERCIAL AIRCRAFT: A POWER SYSTEM AND ARCHITECTURE INVESTIGATION

By MAXIMILIAN THEOBALD EWALD HEINRICH, B.Sc.

A Thesis Submitted to the School of Graduate Studies in Partial Fulfilment of the Requirements for the Degree Master of Applied Science

McMaster University

McMaster University MASTER OF APPLIED SCIENCE (2015) Hamilton, Ontario (Mechanical Engineering)

TITLE: On the Concept of Electric Taxiing for Midsize Commercial Aircraft: A Power System and Architecture Investigation

AUTHOR: Maximilian Theobald Ewald Heinrich, B.Sc. (McMaster University)

SUPERVISOR: Professor Dr. Ali Emadi

NUMBER OF PAGES: xix, 193

“You cannot teach a man anything, you can only help him to find it within himself. “

Galileo Galilei (*1564, † 1642), Physicist and Astronomer

To my father, teacher, role model and friend.

I enjoyed every single moment I spent with you

PAGE LEFT INTENTIONALLY BLANK

ABSTRACT

This research introduces a high-performance electric taxiing system (ETS) as a modern solution to improve the on-ground operations of today's aircraft, which are conventionally powered through the main engines. The presented ETS is propelled by electric motors, integrated into the main landing gear of a state-of-the-art midsize commercial aircraft, and powered by an additional not quantified electrical energy storage system. The proposed system can therefore operate autonomously from any aircraft-internal power source, i.e. Auxiliary Power Unit or equivalent. The main objective of this work is to assess the energy consumption of the introduced ETS while considering energy recuperation due to regenerative braking. The ETS powertrain is sized to match modern conventional taxi performances that were seen in 36 self-recorded takeoff- and landing taxi driving profiles. A custom ETS simulation model was developed and simulated across all available driving profiles to confirm the desired powertrain performance and to predict the system's energy consumption. For the purpose of enhancing the validity of these energy consumption predictions, a suitable motor controller is then designed by the use of MATLAB Simulink. An easy-to-implement switch loss model was created to predict the ETS motor controller efficiency map. Finally, the former energy consumption predictions were revised for the implementation of the motor controller and an estimated traction motor efficiency map. The results exhibit that the revised ETS simulation model was capable of refining the energy consumption. It was found that the ETS will consume up to 9.89 kWh on average if the full potential of the traction motors energy recuperation capabilities are being used. The simulation outcomes further demonstrate that regenerative braking offers great potential in ETS applications since more than 14 % of required traction energy could be regenerated to yield the above mentioned average energy consumption.

ACKNOWLEDGEMENT

I would like to dedicate this thesis to my family, friends, teachers, supporters, former and current colleagues, rivals, and critics. Without your influence, your warm support whenever I came across a critical point in my life, your love, your guidance, your sense of humor, your challenges, and the criticism, I would never have become the person I am today. Furthermore, without all your influence you had on my life, I would have never been able to accomplish this thesis. I am truly grateful to have each one of you on my side and I am very excited to see where this journey takes me.

Explicitly I would like to express my deepest gratitude to my mother Sibylle, and my brother and closest friend Tobias for their influence, trust, and confidence in my capabilities. Additionally I want to thank, Thomas & Christine Kelch, Christian Hörner, Dr. Pierre Magne, Dr. Ali Emadi, Dr. Berker Bilgin, Cody “Kolibri” Rhebergen, Joel “Joey” Roeleveld, Kamran “Kam” Arshad, Ephrem “Papi” Chemali and William “Will” Long for all their support, advice and guidance throughout the last two years.

Additionally, I want to thank my close friend, colleague, and project-partner Fabian Kelch. Without you the time in Canada would not have been the same. I enjoyed working, living, laughing and managing our lives abroad with you. I could not have done all this work without you and the support of your incredible family.

Special thanks also go to Fabrizio Re from the DLR in Germany for his support and the outstanding groundwork he did in the field of electric taxiing, Dan Manolescu for supporting me with fine tuning this thesis and introducing me to the sports culture in Canada, Peter Feldkamp for his amazing support and his devotion during a time in my life where things were not going as expected, Thomas Speck for his influence on my early decision to choose engineering as the right paths for me and his passion for science he shared with everyone in the classroom during my final three years in high school, Dr. Frank Straube who paved the way for me in order to gather valuable technical knowledge alongside my undergraduate studies which offered me various incredible and unexpected opportunities in life, the Mandych family for all the wonderful moments I could spent with you, for your benevolence and for your warmth. Furthermore, I want to give my thanks to Dr. Matthias Preindl for his crucial support in the final phase of my power electronic converter design and efficiency evaluation, Clement Barthelmembs for his patience in teaching me the basics of electrical systems and the operational principles of inverters, Lea Dorn Gomba for her comprehensive feedback on my inverter model design work, Fei Peng for his support in ensuring my inverter model would work properly and for helping me out with basic controller design, Bernhard Bollrath and the Siemens OCD team in Berlin as well as Michael Seimetz and his team at Daimler AG in Stuttgart, Germany for the great experiences I gained by working with each and every one of you. Additionally I wish to thank my lab mates, particularly Alexandre Lepagnot, Axel Frecaut, Julien Lanouziere, Michael Adam, and the entire MARC team for the great two years I spent with all of you.

Finally, it must be mentioned that this research would not have been possible without the support and funding from the Canada Excellence Research Chairs program “CERC".

Hamilton, ON, Canada - August 2015

Maximilian T. E. Heinrich

Table of Contents

List of Figures

List of Tables

Abbreviations

AC	Alternating Current
AFPM	Axial Flux Permanent Magnet (machine)
APP	Accelerator Pedal Position
APU	Auxiliary Power Unit
Back-EMF	Counter or Back Electromagnetic Force
BPP	Braking Pedal Position
Cmd	Command
DC	Direct Current
DTC	Direct Torque Control (control method to control electric machines)
EASA	European Aviation Safety Agency
EMI	Electromagnetic Interference
ESS	Energy Storage System
eTaxi	Electric Taxi / Electric Taxiing / Green Taxiing
ETDS	Electric Traction Drive System (Electric Motors with respective Power Electronics)
ETS	Electric Taxiing System
FG (NG)	Front Gear (sometimes called: Nose Gear)
FOC	Field-Oriented Control (synonymous term to Vector Control)
FOD	Foreign Object Damage
IATA	International Air Transport Association
ICAO	International Civil Aviation Organization
IGBT	Insulated Gate Bipolar Transistor (Switching Device)
MLG	Main Landing Gear

MOSFET	Metal-Oxide-Semiconductor Field-Effect Transistor
MoU	Memorandum of Understanding
MTOW	Maximum takeoff Weight (of an aircraft)
PMSM	Permanent Magnet Synchronous Machine (Electric Motor)
rms (value)	Sometimes written "RMS". Describes the effective value of an AC signal which can be a current or a voltage for instance. The abbreviation "rms" stands for "root mean square". This value is used to quantify the power dissipation of a signal in a resistive load.
SPWM	Sinusoidal Pulse-Width Modulation (Control Technique for Motor Controllers)
SVPWM	Space Vector Pulse-Width Modulation (Control Technique for Motor Controller, belongs to the family of Vector Controls)
VC	Vector Control (control method to control electric machines)
VSI	Voltage Source Inverter

1 INTRODUCTION TO ELECTRIC TAXIING

This chapter introduces electric taxiing as a possible solution for modern aircraft to save fuel and reduce greenhouse gas emissions while conducting on ground taxi operations at airports. The necessity for improved aircraft's operation efficiency, not only during the flight phase but also while operating on-ground, is expressed. Hereafter, the taxi operation itself will be detailed and important terms are introduced that will be used throughout this thesis. Subsequently, possible solutions to improve aircraft taxiing are presented which serves as a market research section that introduces novel and green taxi solutions for commercial aviation. The final section within this chapter focuses on electric taxiing systems and their applications, limitations and opportunities.

1.1 The Change to more Efficient Aircraft

Today's global population growth and the human-made technological progress offer incredible advantages to every one of us. Technologies allow us, for instance, to communicate with people all across the world without any time delay by using a phone or the internet, making the distance between two people a negligible criterion for successful communication. Another paramount example of technologic advancement is modern transportation. Over the last two centuries, the development of modern transportation means, such as air, rail, road, and water-transportation, has significantly improved all our lives. Modern transportation allows rapid transport of goods and humans around the globe which reduces transportation time to a minimum when compared to outmoded transportation solutions.

Besides all the assets humans profit from, new technologies also entail certain drawbacks. One of the major drawbacks of the technological progress within the 21st century is the increase of emissions and the pollution of our planet

[1]. This amongst other factors negatively affects the climate, vegetation and nature, fauna, and it also endangers the state of health of human.

In the beginning of the 21st century such undesirable effects on our planet gained major attention when the international treaty “Kyoto Protocol to the United Nations Framework Convention on Climate Change” or in short: “Kyoto Protocol”- by the United Nations entered into force in early 2005. The protocol introduces emission limitations to each country. It further demands participating countries to increase their energy efficiency in relevant economic sectors (Article 1.a.i), promote research and development on alternative and novel ways to use energy (Article 1.a.iv) and to limit the emissions of greenhouse gases in the transportation sector (Article 1.a.vii) [2].

Based on this milestone in addressing the need for a reduction on our current and future emissions footprint, a variety of economic sector-specific regulations, standards and guidelines were introduced. Among these economic areas, the transportation sector experienced a revolution towards increased efficient solutions. These new efficient solutions shall improve the respective craft’s energy consumption, decreasing the dependency on fossil fuels for propulsion needs, and reducing emissions such as greenhouse gases in addition to noise [1], [3], [4], [5].

Comprehensive guidelines, standards and certification requirements had been introduced by international organizations and applied to the aviation/ aerospace sector. The International Civil Aviation Organization (ICAO), which is a special agency of the United Nations and the International Air Transport Association (IATA), released regulations to enforce adequate emission reductions and improve aircraft’s operational efficiency on a global level. In 2009 the ICAO Program of Action on International Aviation and Climate Change announced the plan to increase annual fuel efficiency 2 % by 2050 [6], which directly affects the amount of allowable greenhouse gas emissions. In addition to these aircraft performance related requirements, operational safety constitutes an ever occurring field of concern. The European Commission Directorate General for Mobility and Transport announced similar top level goals for the future European aviation industry. Within their vision report “Flightpath 2050” for the year 2050, the European Union targets ambitious environmental goals such as a 75% decrease in CO_2 emission per passenger kilometer, a 90% reduction in NO_x emissions, lowering noise levels of operating aircraft, and emission-free aircraft taxiing [7].

Based on the recent concerns related to aircraft emissions that have been mentioned previously, modern aircraft face the challenge to use less fuel, emit less greenhouse gases and less noise while ever increasing in size to allow the transport of increased passenger and cargo capacities. This results in many different, new fields of research to help achieving such market demands. These fields range from improved main engine fuel efficiency to novel materials and composites to decrease the overall weight of the aircraft’s structure to more electrified on-board systems that yield to an enhanced overall power management when compared to today’s conventional aircraft. The latter approach of increasing the degree of electrification within the aircraft is commonly called “More Electric Aircraft” (MEA) and has gained significant importance in the development of future aircraft [8], [9].

When facing the need of improving aircraft operational efficiency, it is important to understand that such an undertaking a multilayered approach and it is indeed not sufficient to solely target the aircraft flight operations. Since on-ground operation is an integral part of each aircraft’s operating cycle, it must be considered as well.

This thesis will investigate and analyze an electrified traction system for modern and future aircraft in order to improve on-ground energy consumption and reducing emissions, such as greenhouse gas and noise, while increasing ground safety and decreasing cost.

1.2 The On-Ground Operations (Taxiing)

This section aims to introduce the different flight phases in order to establish a common knowledge for any subsequent chapter. It is important to be familiar with these phases within one complete aircraft's flight mission to comprehend the scope of this study and to further follow through the analysis part of this master's thesis.

Every standard commercial aircraft's mission is divided into several flight phases which define part of the aircraft's operation. The phases can be further divided in on-ground and airborne operations. Note that the flight phases in case of emergency and special operations have not been considered in this overview.

The most common flight phases for normal aircraft operation are defined by the CAST/ICAO Common Taxonomy Team (CICTT). In order to provide a more structured breakdown on the CICTT's flight phase breakdown the phases described in [10] are slightly modified, supplemented by common knowledge, and categorized according to the operation field in order to provide a more general view on state-of-the-art aircraft missions. The flight phases are summarized in Table 1-1.

The first phase in every modern aircraft mission is the departure standing phase in which the crew of an aircraft prepares the plane for starting its mission. Key actions within phase 1 (STD) are fueling the aircraft, loading cargo, passengers and other necessary actions in order to prepare the aircraft for its upcoming mission. After the aircraft is ready to start its mission, a tractor connects what is known as a "tow bar" to the front wheels of the aircraft in order to push the craft away from the gate; this process is called pushback/ towing to clear the airports gate. Usually the pilot starts up the main engines shortly before or while the aircraft is being pushed back for the purpose of initializing the takeoff taxi phase. The main engines require a certain warm up time to allow operation for the remaining flight phases which can be 3-5 min depending on the main engine type and its generation [11], [12]. Therefore in order to not waste excessive time on the ground, which also affects the timely operation of other arriving aircraft due to congestion at the gate, it is desirable to achieve the shortest possible idle time between the end of the pushback phase and the beginning of the taxi out or takeoff taxi phase (Phase 3).

Table 1-1 – State of the Art Aircraft Flight Phase Breakdown

Operation Field	**Flight Phase**
On-Ground	1. Standing Departure (STD)
	2. Pushback/ Towing (PBT)
	3. Taxi Out (TXO)
On-Ground → Airborne (Transition)	4. Takeoff (TOF)
Airborne	5. Initial Climb (ICL)
	6. En Route (ENR)
	7. Maneuvering (MNV)
	8. Approach (APR)
Airborne → On-Ground (Transition)	9. Landing/ Touchdown (LDG)
On-Ground	10. Post-Impact Phase/ Braking (PIM)
	11. Taxi In (TXI)
	12. Gate Arrival/ Standing (STA)

After the main engines reach their desired operating point (end of warm up phase) and once the aircraft gets confirmation to proceed to the taxi phase, the tractor will be decoupled from the aircraft and the aircraft transitions in to the taxi out phase. Here the aircraft begins to move under its own power. The aircraft moves on "taxiways" to the respective runway at which it is scheduled to leave the airport. At the point where the aircraft reaches the runway, the takeoff taxi phase (Phase 3) merges into the takeoff phase as soon as the aircraft gets the permission for takeoff from the airport flight control located in the tower. The takeoff phase (Phase 4) is a transition phase between on-ground and airborne operation. The takeoff phase is considered complete once the aircraft has reached an altitude of 35 feet above the airport's runway [10], [13].

After the takeoff, the aircraft will then proceed to its actual flight operation (Phases 5-8) which will not be described in detail since this study targets the aircraft on-ground operation. At the end of its airborne operation the plane touches the runway of its destination airport (Phase 9 – Landing/ Touchdown) which marks the transition between in-flight and final on-ground operation. After touching the ground, which is generally a short phase compared to all other operation phases, the aircraft immediately enters into the braking or post-impact phase to ensure that the aircraft slows down to adequate taxi speeds before leaving the runway.

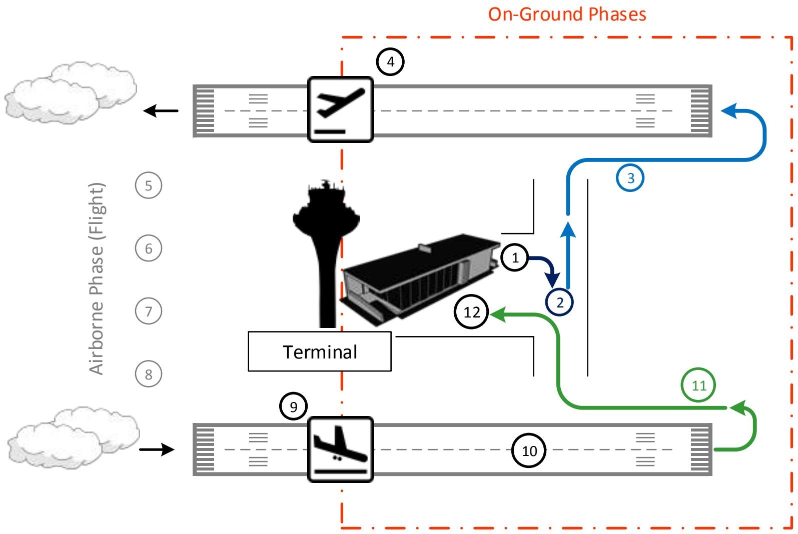

Figure 1-1 – Standard Flight Phases for Modern Aircraft

After the braking phase, the aircraft leaves the runway and enters the taxiway for its touchdown taxi. The aircraft will continue to move independently, powered by its main engines, to its final holding position. The taxi in phase

(Phase 11) is defined as the process between exiting the runway, after touchdown braking, to moving on ground until its final holding position is reached. Touchdown or landing taxiing is sometimes used synonymous to taxi in. Finally, the gate arrival/ standing phase (Phase 12) is reached once the aircraft holds at its desired parking location on the arrival airport. In this phase the plane unloads passengers, cargo and its crew. Moreover, the airplane will also be prepared for its next mission, which will once again start at Phase 1.

Since the objective of this study is to improve the aircraft on-ground operation energy consumption while reducing the emissions, phases 1, 2, 3 as well as 10, 11, and 12 from Table 1-1 are of particular interest for any further investigation. All flight phases are shown in Figure 1-1.

1.3 Improving Aircraft On-Ground Operations

As previously mentioned in the section The Change to more Efficient Aircraft, the aerospace sector, as well as all other transportation sectors, faces the demand to operate more efficiently for the sake of complying with future market requirements. More precisely, future airplanes will face pressure to use less fuel and emit fewer emissions. On the example of carbon dioxide emissions it can be shown that one kilogram of burned modern Jet-A equals to 3.16 kg of CO_2 [14]. Thus, a more efficient aircraft operation will directly affect the carbon dioxide emissions. In order to achieve respective operating improvements as well as reducing costs in prospective aircraft, the transition to more electrified aircraft systems is currently being explored [9] [15] [16] [17].

Indeed, to achieve such a transition to improved aerospace systems, it is mandatory to analyze the complete aircraft operational behavior; which also includes the on-ground operation. Namely speaking, a special focus must be put on the taxi out and taxi in phase and the standing phases at the gate before takeoff and after landing, respectively. The objective of this thesis is to provide an alternative solution for modern and future commercial aircraft's on-ground operation with a special focus on improving the taxi-operation.

The ultimate solution found for the given problem has the positive side effect in that it does not solely improve energy consumption and reduces emissions while taxiing on ground. This system also enables an improvement in aircraft dynamics as well as yielding reduced taxi costs, shorter taxi times, and less noise [18].

Today's on-ground aircraft operations are purely main engine based. That means that the main engines, designed for the actual flight phases, which have been shortly discussed in the former section, are utilized as the power source to move the aircraft on ground. It is furthermore important to know that modern aircraft main engines are designed for flight operations at high power levels and not for idle operation at low power operating points. As a result, using the main engines for on ground operations leads to increased fuel burn since the main engines are forced to operate in a highly inefficient manner [19]. This in turn contributes to the current issue of emitting disproportionately high emissions and affects fuel consumption negatively. Hence, novel and more efficient solutions for the ground activities of aircraft need to be considered to ensure that future goals can be reached.

Several innovative concepts were developed in somewhat more than the last decade to allow a more improved ground operation of modern aircraft. Such systems and technologies will be discussed in the following sections. Finally, the system is introduced which has been selected for this study.

1.3.1 Advanced On-Ground Propulsion Systems Market Research

A number of different systems and innovative concepts have emerged within the last decade. All of the presented systems that intend to achieve improved fuel economy and lower greenhouse gas emissions as well as lowering the noise while taxiing, are based off of advanced electrified systems. Such systems follow different approaches and are shortly discussed and analyzed within this section.

1.3.1.1 Off-Board Systems

Many systems that were recently discussed or presented are off-board systems that target the improvement of the taxi phase by using an external system which most frequently targets advanced tractors or equivalent modern towing systems. Some approaches target the full taxi phase being conducted by a conventional tractor instead of traditional taxiing of the aircraft, others propose to replace conventional tractors by the use of more efficient electric or hybrid electric tractors only for the push back phase. Further taxi systems suggest electrified towing vehicles that tow the aircraft for the whole taxi process.

Hybrid-Electric Tractor for Taxiing “TaxiBot”

The TaxiBot is a hybrid-electric tug for “Narrow Body” or Single Aisle as well as “Wide Body” commercial aircraft. The taxiing system has been designed by Israel Aerospace Industries (IAI) together with TLD, Lufthansa LEOS as part of the Deutsche Lufthansa AG, Siemens AG, Airbus S.A.S., and the Boeing Company. The tractor possesses a diesel engine hybrid electric powertrain to allow proper taxiing performance up to today’s conventional taxi speeds [20]. Two different versions are available:

The Narrow-Body TaxiBot is placed in the small up to medium size aircraft sector; usable for Airbus A318 to A321 or Boeing B737 to B757 aircraft [21].

The second version called “Wide-Body TaxiBot” targets medium to large size commercial airplanes such as Airbus A340 to A380 as well as Boeing B767 to B747 aircraft [21].

This system will be used for the push-back phase as well as the taxi phases. The pushback will be conducted similar to today’s pushback with the only difference of not using a tow or push bar. The Bot will surround the aircraft’s front gear and load the front wheel assembly on a platform within the tractor. The driver of the tractor will steer the tractor only for pushback. Once the aircraft left the pushback phase behind, the pilot will be able to steer and control the TaxiBot due to the interface of the TaxiBot with the Front Gear of the aircraft and the Pilots Control Module (PCM). The pilot will then taxi the aircraft to its desired takeoff runway where the TaxiBot will be detached and the driver within the Bot regains control of the tractor to either return the tractor to the gate or wait for a landing aircraft to taxi it back to the gate [18].

Figure 1-2 - TaxiBot Hybrid-Electric Taxi Vehicle by IAI, picture copyright by DPA

This system is the most advanced and mature across all modern off-board taxi system solutions and is already available for today’s commercial aircraft operations after being certified by the European Aviation Safety Agency (EASA) for commercial use in fall 2014 [22], [23]. The Wide-Body, high performance, TaxiBot is currently within its testing and certification phase.

Electric Schlepper "eSchlepper"

The so called "eSchlepper" is an electrically powered towing vehicle that targets towing operations for large size aircraft of up to 600 tonnes of maximum takeoff weight (MTOW). Lufthansa LEOS announced its development in autumn 2013 and made public that the Lufthansa Technik division is going to partner with the Swedish company Kalmar Motor AB.

Figure 1-3 - eSchlepper by Lufthansa LEOS [22]

The system will not target the actual taxi operation but will focus on increasing the efficiency for maintenance hangar towing operations on ground. However, the system is still in its development process and it remains to be seen when the system enters the testing phase [22], [24].

Taxiing Vehicle by Airbus

Airbus reveals the vision of a completely autonomous operating taxi vehicle that is powered by renewable energy and will taxi the aircraft in and out. The idea is that the taxi vehicle waits for the aircraft when landing at the end of the arrival runway to directly transition into the landing taxi phase without any significant time delay. The vehicles are controlled in a way that they would find the most optimal and shortest taxi way to allow the lowest taxi times possible.

Options to navigate the vehicles on ground are to use either electromagnetic currents flowing through the taxiways on ground or a wireless high power network [25].

Figure 1-4 - Concept of an Autonomous Taxi Vehicle by Airbus [25]

This on-ground system appears to be still in the concept and preliminary research phase. No reports on initial system testing or more precise descriptions on the actual system architecture as well as its functionality are available as of today.

Trace Towbot

The Towbot from the Texas-based company Trace Towbots allows towing and taxing for small size aircraft with a weight up to 50,000 lbs (22,7 tonnes). The small, fully electric taxi robot is remote controlled and will be connected to the nose gear wheels. The strongest Towbot called “Bomberbot TB 9000” is powered by a 24 V DC Electric Motor and can be charged by an integrated battery charger. The rated maximum towing/ taxi speed is indicated with 1.7 feet per second (0.52 m/s or 1.9 km/h). The technology is already available and can be purchased through the company Trace Towbot [26].

Unfortunately the currently available Towbots do not allow taxiing of midsize or even large-scale commercial aircraft.

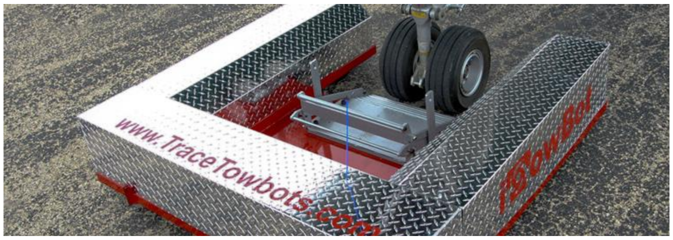

Figure 1-5 - Taxi and Towing Robot for Small Aircraft (TowBot) [26]

Conclusion

Based on the presented market research on off-board solutions for more efficient on-ground operation, it can be summarized that the only system that allows taxiing as well as pushback for any size of aircraft is the TaxiBot system. The eSchlepper does not target the actual taxi or pushback phase for its target application but focuses on more efficient maintenance hangar towing operations. The Airbus system is a promising concept for the future but nothing that can be expected to enter the market in the near future. The Towbot is only available for small scale aircraft and is not a suitable candidate for the scope of this thesis. Thus, only the TaxiBot is a serious candidate to improve overall ground operations since it allows both pushback as well as taxiing of any commercial aircraft type.

1.3.1.2 On-Board Systems

On the other hand, several on-board taxi systems were presented and developed within the last decade. Such systems are commonly located within the aircraft front or main landing gear in order to propel the aircraft on the aerodrome’s ground. The systems that have been presented thus far are all electric propulsion systems that house wheel hub motors within the aircraft gears to electrically power the aircraft for taxiing. These systems are commonly named “Electric Taxiing Systems” (short: ETS).

Electric Taxiing Systems/ Green Taxi Systems (On-Board)

This concept aims to integrate electric hub motors into the aircraft's undercarriage in order to allow completely independent taxiing on ground. Such systems enable major performance and cost related advantages that include, but are not limited to, a reduction in the operation time of the main engines. Additional benefits include improvements on the airplane's manoeuvrability, and decreasing the overall on-ground operation time [3]. Since the on-board installed electric motors provide the power that allows the aircraft to move on-ground, the system is called "Electric Taxi" or "Electric Taxiing" (short: eTaxi). Sometimes the terms "Green Taxiing" or "Green Taxi" as well as "Electric Green Taxi" are used synonymous in the literature.

The electric motors are commonly designed as in-wheel motors which are located in the Front/ Nose Gear (FG) or the Main Landing Gear (MLG) of a selected aircraft. The energy source for this system depends on the corresponding ETS system requirements for an aircraft that is to be equipped with such novel system. Different applications propose a variety of solutions for suitable energy storage systems that feed the motors with electrical power through the motor controllers.

Some systems use a modified Auxiliary Power Unit (APU) that is already installed in every standard commercial aircraft and which is commonly situated in the rear of the aircraft to start the main engines, provide energy for the air conditioning, and supply electrical power to electronic devices on-board for the time when the aircraft has not started its main engines. Other systems suggest conventional battery-based Electrical Energy Storage Systems (ESS) or even Fuel Cells to provide sufficient electrical energy to allow independent aircraft taxiing.

Within the last decade, multiple companies and research facilities have proposed a number of different electric taxiing systems (ETS). Some of them are about to enter the market within the next few years whereas other systems have been designed and tested but do not seem to be commercially available anytime soon. The most prominent systems which have so far the highest degree of maturity are discussed below:

In 2005, the Gibraltar-based company WheelTug conducted the first public proof of concept of an Electric Taxiing System. The WheelTug system was engineered as a Front Gear Electric Taxiing System. Five years later a second test series was performed with a Boeing B737-800 at the airport in Prague after the system was revised and fine-tuned by the company [27]. The goal of this testing series was to obtain further design and system requirements when operating at difficult weather conditions, i.e. snow and ice on the taxiways. Following a successful first ground test of the Front Gear ETS on a Boeing B737-700 in 2012 at Prague airport, the system is now in its final design stage in order to get to market [28], [29], [30].

The Electric Green Taxiing System (EGTS) which is a joint venture of Honeywell International Inc.'s Aerospace Division as a company with expertise in the field of aircraft Auxiliary Power Units and Safran S.A. as a leading company in aircraft undercarriage systems is the most prominent and mature system on the market so far. Both companies signed an agreement to launch a program targeting the design of modern on-board Electric Taxiing Systems that are retrofittable to existing aircraft architectures in 2011. The ETS is integrated into the Main Landing Gear, powered by a modified, and thus, more powerful APU, and targets the application in single aisle airplanes. After a first product test demonstration at the Paris Air Show in 2013, Airbus S.A.S. signed a memorandum of understanding (MoU) to target the use of EGTS in its single aisle A320 aircraft family [3], [18], [31].

Figure 1-6 - EGTS System tested in an Airbus A320 [32]

A third competitor for electric taxiing systems is the “Green Taxi” system from Magnet Motor GmbH by L3-Communications. The system which is equipped with permanent magnet motors is, similarly to the EGTS system from Honeywell and Safran, integrated into the rims of Main Landing Gear wheel assemblies of single aisle aircraft. The power supply for the electric machines is provided by the aircraft APU. An initial system demonstration test was performed on an Airbus A320-200 on the Frankfurt Airport, Germany in December 2011 in partnership with Lufthansa Technik AG and Airbus Industries [33].

The German Aerospace Center (DLR) presented a Front Gear Electric Taxi System which is powered by a Fuel Cell. The system contains two permanent magnet electric motors, one motor for each front gear wheel, as well as a switchable planetary gearbox system to switch between two different gear ratios. The high gear ratio setting allows transmitting the requested torque to the wheels while taxiing on ground at lower speeds and the low gear ratio (direct drive) setting is used for pre-touchdown wheel spin up to reduce tire wear. The system has been developed and tested together with Airbus S.A.S. and the Lufthansa Technik AG in Germany. Initial system tests were undertaken on an Airbus A320 single aisle aircraft at the Hamburg Finkenwerder Airport, Germany in 2011 [18], [34].

Delos Aerospace is another company that provides solutions for electric taxiing with an on-board system. The system targets the complete on-ground motion of the aircraft which includes pushback and taxi. The system also allows for electromagnetic braking after touchdown by replacing the conventional friction brakes on an aircraft. The braking process enables electrical power regeneration since electric motors would be driven in generator mode. A suitable on-board ESS will then capture the regenerated energy and use it for taxiing on ground and/ or other on-board systems. Furthermore, the ETS allows spinning up the tires before touchdown to reduce tire wear when touching the ground while landing [35].

Conclusion

Concerning the Delos Aerospace Electric Taxi System, no testing reports, certification progress documentation or equivalent system/ product information are available. Additionally, the company's homepage was last updated in 2011 which makes it difficult to evaluate the products significance or its closeness to market entry. Although the system's concept sounds very promising since it claims several great features and targets all aircraft weight classes, it does not seem like it will be ready to be available on the market anytime soon. The only resources that could be found were patents on the electric motor's functionality on a concept level basis [36], [37], [38].

The Magnet-Motor Green Taxi system might be an option as well, but not much information is available regarding the recent status of the progress on the market entry. L3 provides only a testing video of the system but does not comment on any other development as of now. A similar position has to be taken up when evaluating the electric taxiing system from Delos Aerospace. Delos provides even less product information which make it difficult to predict when or if the system enters the market at some point. The DLR fuel cell powered front gear eTaxi System targets very low speeds so far (25 km/h top speed) and does not provide sufficient system peak power to allow competitive taxi performance when compared to today's conventional main engine taxiing [18]. The German Aerospace Center system can be seen as a milestone regarding the feasibility of certain ETS topologies but it requires a lot more research progress and time to bring such system to the market. Therefore, it cannot be concluded that the latter systems are to be certified or usable in the near future. Furthermore, it can also not be determined when or if these systems will become commercially available within the next decade.

Thus it can be concluded that only the WheelTug and EGTS systems appear to be serious options for electric taxi on-board systems. Both systems provide recent status reports on their system progress and development.

1.3.2 Advanced On-Ground Propulsion System Selection

Based on the previous market research analysis section on advanced on-ground propulsion systems, an overall comparison between on-board and off-board solutions will be conducted in this section. In consequence of this comparison one system topology will be selected for this research work. The respective advantages and disadvantages of on-board and off-board on ground propulsion systems are described below and it will be explained why on board systems have been selected for the subsequent work of this thesis.

Besides the differences among on and off-board systems, both systems fulfil the major demands on increased efficient taxiing and enable further secondary benefits. The actual quantification on the respective benefits of each advanced on ground propulsion system depends on the actual system's design and is not addressed in this general overview. All general primary advantages and further secondary benefits based on [3], [23], [31], [33] are described in Table 1-2.

Table 1-2 - Advanced On-Ground Propulsion Systems: Advantages and Benefits

Primary Advantages	• Less fuel consumption for on-ground operations, • Reduction in emissions which includes greenhouse gases as well as noise
Secondary Benefits	• Reduced on-ground operation time • Possibility of cost savings (shorter on-ground operating time, less fuel consumption) • Reduction of Foreign Object Damage “FOD” • Improving aircraft On Time Performance “OTP” (rapid transition from pushback to taxiing) • Increased airport throughput (more flight missions in the same time frame) • Reduced Brake Wear of Aircraft Brakes • Increased service life of main engines (maintenance reduction) • Possibility of on-ground safety (e.g. no installation of tow bar required anymore, less or even no additional personnel for on-ground operation required, etc.) • Fail Safe Mode: in case of system failure conventional main engine based taxi can be used

The following sections will focus on the specific advantages and disadvantages of modern and future on ground propulsion systems for the aerospace sector.

Off-Board Systems

The idea of using modern and advanced tractors/ tugs for the full taxiing phase is a great and simply realizable concept. Such solutions allow addressing the required improvements of lowering emissions as well as improving the on-ground energy consumption for aircraft of all types. The key benefits of such systems are summarized below [23]:

- No modifications on aircraft required
- APU must not be replaced
- Off-board power supply for on-ground operation (no power demand from aircraft internal systems)
- No additional weight to aircraft (system is off-board)
- Intuitive system control (no need for advanced training of pilots)
- Usable for all commercial aircraft classes
- Taxi speeds similar to conventional taxiing (23 knots)
- Indicated Return of Investment (ROI): 1.5 – 2 years

Another great advantage is the fact that one tractor can be used for different aircraft types since its application is not limited to a specific aircraft. Furthermore, as stated in [18], the systems development is completely isolated from the aircraft architecture which simplifies the systems design significantly.

On the other hand, several shortcomings can be found when analyzing the operation of off-board systems for on-ground aircraft taxi and pushback operations:

- System use might require on-ground infrastructure expansion due to increased traffic of the tractors that need to travel from the gate to the runway and vice versa [18],

- Since air traffic increases in the future, additional tractors might cause ground traffic delays. In the worst case these delays could offset the cost saving advantage when using advanced on ground propulsion systems [18],
- More motion on ground due to additional vehicles on the taxiways might yield to safety issues and concerns [18],
- Most solutions still require additional personnel to sit inside the system to steer the vehicle for pushback and to connect the tractor with the jet (cost factor and safety risk),
- If the system should operate automatic a complex network and guidance control infrastructure needs to be developed which would increase the costs to implement such technology [18],
- Some proposed solutions propose hybrid powertrains that combine diesel engines and electric motors to taxi airplanes. Such a solution has a lower powertrain efficiency than modern electric systems and would not allow zero-emission taxiing,
- No improvement in maneuverability. Turning radii for the aircraft will most likely stay the same; no 360 degree rotation about aircrafts center of gravity,
- Tractor based off-board systems are difficult to use for taxi-in phases due to their connection/ disconnect time (no seamless taxi operation can be achieved) [12],
- Airport needs to maintain large infrastructure when implementing this technology,
- Usage of system locally limited to respective airport. Airports that do not have these advanced tractors cannot profit from this advanced technology and will still face the key issues of costly, inefficient and emission emitting taxiing [18].

On-Board Systems

As discussed previously, so called Electric Taxi Systems seem to be the only viable option for improved, modern on-board ground operation systems for aircraft. Several systems follow different design layouts and are currently in the concept or development phase. Depending on the location of the system within the selected aircraft, different on-ground performances can be expected. In the following a summary of the major advantages and disadvantages of ETS in general is presented:

<u>Advantages</u>:

- Elimination of tractor/ tug for on-ground operations [3]
    - Significant decrease in the on-ground traffic density
    - Strong safety improvement in the apron area[1]
- Autonomous aircraft repositioning and independent on-ground motion [19], [31]
    - Independent reverse and forward motion
    - Maneuverability improvement
        - Possibility for aircraft to rotate about its center of mass
        - Tighter cornering on-ground possible
    - Rapid "pushback and go" transition (time reduction)
    - Cost savings
    - Increase in gate autonomy
- System's area of use not limited to certain airport facilities, system is installed on-board

---

[1] The apron describes the area of an airport where aircraft are parked, fueled, where luggage is loaded or unloaded, and where passengers enter/ exit airplanes.

- On-board energy regeneration while taxiing (usable not only for taxi system but also for other internal aircraft systems)
- Fully electric system (zero emissions while operating)

<u>Disadvantages</u>:

- Additional weight might offset fuel savings on ground when aircraft is considered for medium (3-6 hours) or long haul (6-12 hours) flights [19], [39]
    - System limited to short-haul operations (max. 3 hours)
    - System only usable for small or medium size aircraft; sometimes referred to as "single-aisle aircraft"
- Certification more difficult than for off-board systems [12]
- Heat of brakes will affect system; especially after touchdown braking [12] (challenges for system cooling)
- Packaging space for system is highly limited
- System requires energy source such as an ESS, Fuel Cell, modified APU or equivalent
- System hard to retrofit; might require aircraft undercarriage redesign
- For competitive on-ground taxi performance, a challenging system design is required (characterized by high performance electric machines)

System Selection

With respect to the previously discussed advantages and disadvantages of modern on and off-board on-ground propulsion systems, the on-board systems have been selected for this research project.

Similarly to the final statement made in [18] which compared different novel concepts for improved airport on-ground operation systems, it must be concluded that a combination of on and off-board ground propulsion systems appears to be the only solution to allow faster, more efficient and cleaner ground maneuvers for all different types of modern and future aircraft.

The decision to analyze on-board systems was made based on the forecasts for the future passenger traffic growth which can be expected to rise between 4.1% up to 4.8 % per year through the year 2034 and 2036, respectively [6], [40]. A growth in passenger traffic is directly related to an increased demand on air traffic in general. The idea of improving the on-ground operation efficiency while offering the opportunity to decrease ground traffic, especially with considering the trend of significant growth in worldwide air traffic, has been picked as the critical system selection criteria. Adding more vehicles on the airports infrastructure might yield serious problems such as increased on-ground congestion and the likely demand for airports ground network extensions to handle the increased vehicle numbers. Other problems include the requirement for highly complex novel ground management strategies to manage the high volume of ground traffic. Furthermore, the fact that off-board systems are limited to local operations on a certain airport is another important factor within this consideration. In case a certain airport is not equipped with such modern off-board propulsion systems, it will be excluded from the advantages such systems offer.

The on-board system was chosen since it offers an integrated system that is not limited to local airports for its application, and it does not cause further logistical issues to future airport layouts and their ground operation processes. Moreover, the fact that Electric Taxiing Systems facilitate shorter ground operating times than off-board systems, which increases customer appeal, was a very important criterion to choose such a solution. Even though Electric Taxiing Systems are hardly retrofittable to current aircraft undercarriages and are limited in terms of their operating range they appear to be a more promising solution; especially for short flights with long ground operating phases.

2 ELECTRIC TAXIING SYSTEM SIZING

This chapter presents the ETS powertrain system sizing process for a chosen modern single aisle midsize commercial aircraft. Initially the system's design approach will be discussed to highlight the novelty of this study compared to previously introduced Electric Taxiing System layouts. The outcomes of this chapter are top level ETS powertrain component specifications that comply with a set of taxiing performance requirements.

The major topics that are addressed in this chapter are:

- ETS design approach for an Airbus A321 commercial aircraft,
- Modern taxiing drive cycle analysis which yields ETS performance requirements,
- Airbus A321 ETS sizing process,
- Prediction on the ETS energy consumption based on a custom ETS simulation model

This chapter is of significant importance to any subsequent analysis within this research project since it defines the ETS powertrain layout.

The proposed ETS is powered by an additional not further quantified on-board energy storage unit. The challenge of finding a suitable energy source and/ or energy storage system for the given application was not scope of this study and has not been addressed. This study therefore assumes that the required power to taxi the aircraft electrically is provided by a unique bidirectional energy source which can operate completely independent from any aircraft internal power source such as the Auxiliary Power Unit (APU) for instance. The exact nature of the energy source can be an APU, a flywheel, ultracapacitors, batteries, or any other energy storage system and any combination of these. Ultimately, the final nature of the energy source depends strongly on the required power and energy ratings, the available space within the aircraft, the required energy and power density, and the overall system's complexity

By considering a set of 36 self-recorded different taxi drive cycles- that include 19 takeoff and 17 touchdown taxi driving profiles- the ETS performance requirements are determined.

Subsequently to the requirements evaluation, the ETS was sized to comply with modern taxi performance demands.

The ETS powertrain sizing process for the selected commercial midsize aircraft was conducted together with Mr. Fabian Kelch at McMaster University in a shared research collaboration project [41].

2.1 ETS Design Approach

Most studies or publications on the subject of electric taxiing propose electrified traction systems that satisfy universal performance requirements for the peak taxi speed, maximum acceleration and power ratings for the major powertrain components such as electric motors, power electronics, and the energy source.

As of today, there is not a single ETS certified or in series/ mass production which could be used as a design benchmark. Furthermore, there are no taxi-operation standards existing which address the process of sizing such systems. Therefore, important design questions such as how fast can modern aircraft move and accelerate on-ground of airports around the globe are not addressed. These two factors led to many different ETS design concepts and prototypes that all follow individual design approaches. The following two examples verify this statement.

1. Example - Maximum available top speed for different ETSs:

   It was found that system top speeds vary largely from 10 knots (18.5 km/h) for the Front Gear system from WheelTug over the Main Landing Gear system "EGTS" from Honeywell/ Safran with approximately up to 20 knots (37 km/h) up to ETS concepts that target more than 25 knots (46 km/h) [18], [42].

2. Example – Energy Sources / Energy Storage Devices for ETSs:

   The majority of concepts or prototypes such as EGTS, the WheelTug system, and the Green Taxi system from Magnet Motor use the APU of the respective target aircraft to satisfy the power demand coming from the Electric Traction Drive Systems "ETDSs"[2] [3], [19], [43]. In doing so, some companies reuse the given APU in the rear of the selected aircraft to provide power to the ETS. However, such a powertrain layout might not provide enough available power to achieve a comparable performance when compared to conventional, main engine based, taxiing. Only the Honeywell/ Safran system EGTS announced that it will operate with a modified APU to provide the electric taxi system with more power. Nevertheless, it remains to be seen if the EGTS's APU will be able to deliver enough power to achieve a similar taxi performance as conventional taxiing. The German Aerospace Center (DLR) on the other hand designed and tested a front gear system that uses a hydrogen fuel cell to power their ETS [34]. Even though this system layout adds an additional energy storage device to the aircraft's infrastructure to feed the associated ETS, the system suffers from a low power-to weight ratio which needs

---

[2] An ETDS is composed of an electric machine and its respective motor controller (traction motor plus power electronics to drive the electric machine)

to be carefully considered when the system is evaluated in terms of taxi performance.

The above mentioned two examples indicate that novel ETSs still strive to find a set of requirements that can be used to design a system that does not only demonstrate the systems operational feasibility but also delivers competitive performance when comparing it to conventional taxiing.

Therefore, special attention had been given to the subject of deriving appropriate ETS design requirements in this case study. It was decided to analyze actual taxi operations of modern midsize aircraft while they were operating. This allows tailoring a system for a chosen aircraft that will not suffer from a lack in taxi performance when compared to today's aircraft taxiing. This ETS design philosophy for this project can be described as an "Equivalent Performance Design Approach".

2.2 Aircraft Selection and Weight Estimation

Aircraft Selection

The foundation for sizing an ETS is the selection of an aircraft in which the proposed taxiing system can be integrated. Several studies on the topic of electric taxiing have targeted recent small or midsize commercial airplanes for their designs. Therefore, one of the larger modern single-aisle midsize aircraft has been chosen for this study. This selection allows defining and exploring the highest possible performance envelope for feasible ETS applications as of today. Indeed, considering the enormous mass of large aircraft it is understandable that an ETS for such application is not viable with present performance numbers for traction motors and especially electrical energy storage devices. As shown later in this chapter, the decision to select one of today's largest midsize aircraft and sizing an ETS for it that pursues the selected design philosophy already results in a system which requires traction motors that show similar performances as the most powerful motors available on the market.

For the scope of this research project an Airbus A321 commercial aircraft from Airbus S.A.S. has been selected.

Airbus A321 Wheel Data

Due to the fact that the electric ground propulsion system will interface with the aircraft wheels, it is important to quantify the actual wheel geometry.

Table 2-1 - Common commercial aircraft wheel specifications

Aircraft Type/ Name	**Tire Sizes (Main, Nose)**	**Tire Label [in]**	**Nom. Tire Ø**	**Nom. Rim Ø**	**Tire Mass** [44]	**Rim Mass** [45]
Airbus A321 (Max. Ramp Weight: 89.4 t) [46]						
	Main (MLG)	49x18-22	1.245 m	0.556 m	198.8 lbs (90.2 kg)	*74.4 kg
	Nose (FG)	30-8.8 R15	0.762 m	0.381 m	52 lbs (23.6 kg)	*51 kg
Boeing 737-500 (MTOW: 61 t) [47]						
	Main (MLG)	40x14.5-19	1.016 m	0.483 m	150.4 lbs (68.2 kg)	39.6 kg
	Nose (FG)	27x7.75-15	0.686 m	0.381 m	38.9 lbs (17.65 kg)	n.a
Boeing 747-400 (MTOW: approx.. 400 t) [48]						
	Main (MLG)	49x19-22	1.245 m	0.556 m	248.5 lbs (112.7 kg)	74.4 kg
	Nose (FG)	49x19-22	1.245 m	0.556 m	112.7 kg	74.4 kg
** Estimated values (see explanation in this section)*						

Commonly aircraft tire and rim data is difficult to obtain. With the help of previous studies and the comparison of available aircraft wheel data, the Airbus A321 tire and rim specifications were determined.

Generally, aircraft tires are labeled according to the following labeling scheme:

$$\underbrace{TT}_{\substack{Nominal\ Tire\\ Diameter\ [in]}} \quad x \quad \underbrace{WW}_{\substack{Nominal\ Tire\\ Section\ Width\ [in]}} \quad - \quad R\ \underbrace{XX}_{\substack{Nominal\ Wheel,\\ Rim\ Diameter\ [in]}}$$

Thanks to the information provided in [49], the tire dimensions for wheels located in the aircraft's front gear (FG) and the main landing gear (MLG) could be determined. The tire and rim mass data that was presented in [44], [45] was used to estimate the respective masses for the Airbus A321 wheels. The collected data is summarized in Table 2-1.

Since the Airbus A321 MLG rim size (22 inches) is equivalent to the rim size of the wheels in a Boeing 747-400 aircraft (Table 2-1), the rim mass of an Airbus A321's MLG wheel was assumed to be equivalent to the rim mass of a Boeing 747-400 MLG wheel.

Concerning the FG rim mass for the Airbus A321 no information could be found. Thus, the Airbus A321 FG rim mass was estimated. To do so, the ratio of the A321 FG rim diameter to the Boeing 747-400 MLG rim diameter was used to approximate the unknown A321 FG rim mass. In other words, it was assumed that the rim's mass-to-diameter ratio of an Airbus A321 FG rim and a Boeing 747-400 FG rim is the same. This conservative approach resulted in an estimated Airbus A321 FG rim mass of circa 51 kg.

Wheel Inertias:

The wheel inertias of the Airbus A321 MLG and FG wheels are important inputs to any subsequent analysis that will be done on the plane's dynamic taxi behavior. This section will cover the derivation of estimated Airbus A321 FG and MLG wheel inertias.

1. Airbus A321 Main Landing Gear Wheel Inertia

For the purpose of determining the MLG wheel mass moment of inertia $J_{M_{MLG}}$, it will be assumed that the rim can be approximated by a thin plate and a circular ring. Furthermore, the total rim's mass m_r that was derived in Table 2-1 was assumed to be equally divided into a mass m_1 for the thin plate and mass m_2 for the circular ring [50].

$$m_1 = m_2 = \frac{m_r}{2} = 37.2\ kg$$

With the geometric information from Table 2-1 and the masses m_1 and m_2, the mass moment of inertia for the thin plate J_{rtp} and the circular ring J_{rr} can be calculated.

Thin-plate part of the rim:

$$J_{rtp} = \frac{m_1 \cdot r_{rim}^2}{2}\ .$$

Circular ring part of the rim:

$$J_{Mr} = m_2 \cdot r_{rim}^2\ .$$

The total rim's mass moment of inertia for a MLG wheel J_{rMLG} equals to the sum of the rim's thin plate mass moment of inertia J_{rtp} and the rim's circular ring mass moment of inertia J_{rr}.

$$J_{rMLG} = J_{rtp} + J_{rr}$$

$$J_{rMLG} = \frac{m_1 \cdot r_{rim}^2}{2} + m_2 \cdot r_{rim}^2$$

With $m_1 = m_2 = m_r/2$:

$$J_{rMLG} = \frac{3}{4} \cdot m_r \cdot r_{rim}^2$$

The tire's mass moment of inertia J_{tMLG} was calculated according to two different approaches. The first approach assumed the tire being a torus J_{tt} whereas the second modeled the tire as a circular ring J_{tr}. When the tire's torus based mass moment of inertia was compared to the ring based model, it was found that the ring yields a 70 % higher mass moment of inertia for the considered tire. It was then decided to select the higher inertia in order to implement a conservative estimation for the aircraft's total wheel inertia $J_{M_{MLG}}$.

Tire torus based mass moment of inertia J_{tt}:

$$J_{tt} = m_{tire} \left(\frac{3}{4} \cdot r_i^2 + r_c^2 \right) .$$

Here, $r_i$stands for the inner radius of the torus and r_c describes the radius to the center of the tube (torus center radius).

Tire circular ring based mass moment of inertia J_{tr}:

$$J_{tr} = m_{tire} \cdot r_{tire}^2$$

Since $J_{tr} > J_{tt}$ it was chosen:

$$J_{tMLG} = J_{tr} \ .$$

The sum of rim's and tires mass moment of inertia yields the mass moment of inertia for one wheel within the Airbus A321's MLG $J_{M_{MLG}}$:

$$J_{M_{MLG}} = J_{rMLG} + J_{tMLG}$$

$$J_{M_{MLG}} = \frac{3}{4} \cdot m_r \cdot r_{rim}^2 + m_{tire} \cdot r_{tire}^2 \ . \tag{1}$$

With the given parameters for wheel dimensions, the rim's and the tire mass from Table 2-1 the mass moment of a single wheel within the aircraft's MLG $J_{M_{MLG}}$ was computed.

$$J_{M_{MLG}} = 39.3\ kg \cdot m^2 \tag{2}$$

2. Airbus A321 Front Gear Wheel Inertia

The exact same process to determine the MLG wheel mass moment of inertia $J_{M_{MLG}}$ has been applied to determine the FG wheel mass moment of inertia $J_{M_{FG}}$. The equation to compute $J_{M_{FG}}$ is equivalent to eq. (1) with the only difference that the values for tire and rim masses as well as the dimensions for the rim and the tire radius must be substituted for the FG specific numbers that are given in Table 2-1. Finally, the FG wheel mass moment of inertia $J_{M_{FG}}$ was determined:

$$J_{M_{FG}} = 4.83\ kg \cdot m^2 \tag{3}$$

The results of the inertia calculation for MLG and FG wheels are summarized in Table 2-2.

Table 2-2 - Airbus A321 Wheel Mass Moment of Inertia

Aircraft Type/ Name	**Tire Location (Main, Aux.)**	**Tire Label [in]** [49]	**Mass Moment of Inertia J_M $[kg \cdot m^2]$**
Airbus A321	Main (MLG)	49x18-22	39.3
	Nose/ Front (FG)	30-8.8 R15	4.83

Aircraft Mass Estimation (Static and Dynamic Mass)

An important first step in the ETS sizing process is the determination of the actual aircraft mass. This in turn requires the system designer to estimate the planned ETS's weight which is to be added to the chosen aircraft's mass. With the estimate of approximately 500 kg for the additional mass of electrified propulsion systems that was published in [18] and based on a mass estimation of 800 kg that had been conducted for a less demanding ETS in [51], an initial ETS weight estimate of 1200 kg was made. With this additional weight the system was sized initially to determine the expected powertrain component specifications. Once the numbers were derived the additional ETS weight was reassessed based on the initial powertrain component specification results and fine-tuned to improve the weight estimate. The system sizing process was iterated to derive more accurate powertrain component specifications. It was found that the first ETS weight estimate was already very close to the final ETS's mass approximation.

Static Aircraft's Mass m_{stat}:

Once the final powertrain component specifications for the electric traction drive system's (ETDS) and the energy storage systems (ESS) were determined, the ETS's static mass had been approximated. Static mass in this context equals to the airplanes mass while standing; when the plane is not in motion. The ETDS's mass, composed of electric motor(s) and corresponding power electronics, was calculated from the peak motor system power of 520 kW, and the mean value of the technical targets for the specific power of Electric Traction Drive Systems between the years 2015 (1.2 kW/kg) and 2020 (1.4 kW/kg) [52]. Similarly, the estimated weight for the not further specified ESS was derived from the required ESS peak power within the ETS of almost 592 kW and the power density for future lithium ion batteries (0.8 kw/kg) [53]. A lithium ion ESS was chosen as a baseline or orientation technology to assess the expected

ESS's weight but the ESS technology will not be limited to such energy storage solution. With an estimated mass of 740 kg for the ESS and 400 kg for the ETDS, the overall mass of the ETS results in 1140 kg. Adding the ETS's mass to the maximum ramp weight of an Airbus A321 yields the expected total static mass m_{stat} of the target aircraft. A summary of all important midsize aircraft specifications is given in Table 2-3.

Dynamic/ Inertial Mass of the Aircraft m_i

The so called "equivalent inertial mass" m_i of a system is composed of the total system's static mass m_{stat} and an equivalent mass which originates from all rotating parts and their respective inertia within a moving system. Since the inertia of a certain component can be described in a simplified fashion as resistance against the change in rotational speed of a certain rotating component, it needs to be considered when a systems dynamic behavior is analyzed. The inertia effect coming from rotating parts within a system acts as an additional resistance which a system needs to compensate in order to deliver the desired output performance.

Applied to the targeted aircraft and more precisely applied to the ETS, all rotating components and their respective inertia effect on the planes change in speed need to be factored in. Inertias will include shaft, gears, and the rim and tire inertias.

When the aircraft's kinetic energy for on-ground motion is analyzed, an expression for the actual aircraft inertial/ dynamic mass m_i can be derived. Generally, the dynamic mass of a system can be expressed as the product of the systems static mass m_{stat} and the so called rotational inertia factor δ [54]:

$$m_i = \delta \cdot m_{stat} \tag{4}$$

The magnitude of δ depends on the final ETS design for the chosen aircraft. Factors that will affect δ are for instance the electric machine's rotor inertia, a gearbox with its respective gears, the number of traction motors used, and the wheel dimensions. Furthermore the wheel specifications of wheels within the aircraft's undercarriage will strongly contribute to the inertia factor's magnitude. Summarized, important parameters for the computation of the rotational inertia factor are [51]:

- Wheel dimensions (obtainable for example from [55]),
- Number of wheels,
- Mass of tires,
- Mass of rims,
- Wheel mass moments of inertia (one possibility to approximate these parameters is given in [50]),
- Powertrain component inertias (shafts, electric machine rotor, gears, etc.),
- And the gear ratio of a gearbox in case a transmission is used.

Since the final shape of the powertrain was not available in the initial ETS sizing process an overall estimate for the rotational inertia factor δ was made based on the findings that were obtained in [51]. A first system design assumed an inertia factor of $\delta = 1.01$ which means that the rotational inertia effect of all rotating components in the proposed ETS equals to a dynamic mass increase of 1% when compared to the aircraft's total static mass m_{stat}.

Due to this first dynamic mass estimate the respective powertrain design requirements were evaluated and a system was sized. It was found that four traction motors will be required to provide the desired performance. Furthermore it was assessed that the use of a gearbox will be required to supply the demanded torque to the wheels of the aircraft when taxiing. Once the powertrains shape was determined, another and more sophisticated analysis on the actual expected dynamic mass based on the aircraft's kinetic energy while taxiing was conducted.

The airplane's total kinetic energy while taxiing E_{kt} is a combination of translational (linear) kinetic energy E_{kl} and rotational kinetic energy E_{kr} that originates from rotating parts (i.e. wheels in the MLG and FG, shafts, electric machine rotor, gearbox, etc.).

$$E_{kt} = E_{kl} + E_{kr} \tag{5}$$

To determine the actual total kinetic energy of the aircraft while taxiing E_{kt} it can be assumed that the rotational and translational energy portions E_{kl}, E_{kr} will both merge into an equivalent translational kinetic energy E_{keq}; E_{kt} will then be equivalent to E_{keq}. This equivalent energy will then equal to an equivalent dynamic mass m_i which is called aircraft dynamic/ inertial mass and the instantaneous velocity v of a system; here the taxi velocity. The dynamic mass m_i incorporates the aircraft's static mass m_{stat} and the mass inertias of all rotating parts in the ETS.

$$\underbrace{\frac{1}{2} m_i v^2}_{E_{keq}} = \underbrace{\frac{1}{2} m_{stat} v^2}_{E_{kl}} + \underbrace{\sum_i \frac{1}{2} J_{M_i}\, \omega_i^2}_{E_{kr}} \tag{6}$$

$\sum_i \frac{1}{2} J_{M_i}\, \omega_i^2$	Rotational kinetic energy for all rotating components in the ETS
J_{M_i}	Mass moment of inertia for component i in the ETS $[kg \cdot m^2]$
ω_i	Angular velocity of rotating component i in the ETS $[rad/s]$.

In case that certain rotating parts spin with the wheel (tire) angular velocity ω_W ($\omega_i = \omega_W$), the angular velocity of such components ω_i can be simply expressed in terms of the current taxi velocity v and the respective tire radius r_t:

$$v := \omega_w \cdot r_t \tag{7}$$

$$\xrightarrow[\omega_i=\omega_w]{} \omega_i = \frac{v}{r_t} \tag{8}$$

If the rotating parts are separated from the wheels by a transmission unit- or several transmission units ($\omega_i \neq \omega_W$), then the applicable transmission gear ratios k need to be considered in order to express the component's angular velocity ω_i as a function of the current craft's velocity v at the wheels.

The transmission gear ratio k is defined by the ratio of input ω_{in} to output ω_{out} angular velocity. Applied to ETSs, the gear ratio will equal to the components angular velocity ω_i divided by the wheel angular velocity ω_w:

$$k = \frac{\omega_{in}}{\omega_{out}} = \frac{\omega_i}{\omega_W}$$

$$\xrightarrow[\omega_i\neq\omega_w]{} \omega_i = k \cdot \omega_W$$

With eq. (7):

$$\xrightarrow[\omega_i\neq\omega_w]{} \omega_i = k \cdot \frac{v}{r_t} \tag{9}$$

By implementing eq. (8), (9) in eq. (6) one obtains:

$$\frac{1}{2} m_i v^2 = \frac{1}{2} m_{stat} v^2 + \underbrace{\sum_i \frac{1}{2} J_{M_i} \left(\frac{v}{r_t}\right)^2}_{\substack{rot.Energy\ of\ parts\ that\\ rotate\ with\ the\ wheel\\ angular\ velocity\ \omega_W}} + \underbrace{\sum_j \frac{1}{2} J_{M_j} \left(k \frac{v}{r_t}\right)^2}_{\substack{rot.Energy\ of\ parts\ that\\ rotate\ not\ with\ wheel\\ angular\ velocity\ \omega_w}} \tag{10}$$

Dividing eq. (10) by $\frac{v^2}{2}$ yields the expression for the dynamic/ inertial mass m_i:

$$m_i = m_{stat} + \sum_i J_{M_i} \frac{1}{r_t^2} + \sum_j J_{M_j} \frac{k^2}{r_t^2} \ . \tag{11}$$

Equation (11) enables ETS designers to accurately compute the aircraft's total equivalent dynamic mass m_i as a result of the powertrain layout. In case there is no transmission used within the powertrain, also called direct drive powertrain, the third term in equation (11) must not be considered $\left(\sum_j J_{M_j} \frac{k^2}{r_t^2}\right)$.

The above derived dynamic mass equation depends on the static systems mass m_{stat}, the mass moments of inertia for all rotating powertrain components J_M, and the geometry of all rotating components within the ETS powertrain.

The detailed system parameter definition process is covered in the ETS Powertrain Sizing section. After running through several powertrain sizing iterations where the component specifications were continuously fine-tuned, a final ETS design was identified that will be implemented into the airplane's MLG. All four MLG wheels will need to house an electric machine to output the required traction power through a transmission to all four MLG wheels.

Applied to the chosen aircraft with the final ETS powertrain design the equivalent dynamic mass m_i was computed by the use of the following equation which is based on eq. (11):

$$m_i = m_{stat} + \underbrace{n_{w_{FG}} \frac{\mathrm{J}_{\mathrm{M}_{\mathrm{FG}}}}{\left(\frac{d_{tFG}^2}{4}\right)}}_{FG\ wheels} + \underbrace{n_{w_{MLG}} \frac{\mathrm{J}_{\mathrm{M}_{\mathrm{MLG}}}}{\left(\frac{d_{tMLG}^2}{4}\right)}}_{MLG\ wheels} + \underbrace{n_{EM} \cdot J_{M_R} \frac{k^2}{\left(\frac{d_{tMLG}^2}{4}\right)}}_{Electric\ Machines}$$

Table 2-2 and Table 2-3 contain the majority of variables that were used to determine the dynamic/ inertia mass m_i. The missing parameters such as number of electric machines used in the ETS n_{EM}, electric machine rotor inertia J_{M_R}, gear ratio for the transmission k depend on the final ETS powertrain layout. The following numbers were derived while sizing the powertrain:

- $n_{EM} = 4$,
- $J_{M_R} = 0.2\ kg \cdot m^2$ (estimated number for rotor inertia, depends on the actual motor design which is not part of this study),
- And $k = 12$ (selected gear ratio to transmit demanded torque to the MLG wheels).

With these ETS parameters the dynamic mass of the commercial Airbus A321 aircraft m_i resulted in:

$$m_i = 91309.5\ kg$$

$$\rightarrow \delta = \frac{m_i}{m_{stat}} = 1.0085$$

The derived rotational inertia factor δ indicates that the rotating components in the aircraft add an equivalent mass of 0.85% to the total static aircraft mass of 90.54 tonnes.

Table 2-3 - Aircraft Type and Specifications

Aircraft Type [32]	Airbus A321
Max. Ramp Weight [32] [t]	89.4
ETS Mass Estimation [t]	1.14
Aircraft total static mass for Simulation m_{stat} [t]	90.54
Rotational Inertia Factor for dynamic mass (initial estimate) δ	1.0085
Aircraft total dynamic mass (initial estimate) m_i [t]	91.31
(A321 Coefficient of Drag) x (A321 Active Frontal Area) $c_D \cdot A_{ref}$ [56] [m^2]	2.6
Number of FG wheels n_{wFG} [-]	2
Front Gear: Tire Diameter d_{tFG} [m]	0.762
Front Gear: Tire / Rim Mass [kg]	23.6/ 51
Number of MLG wheels n_{wMLG} [-]	4
Main Landing Gear: Tire Diameter d_{tMLG} [m]	1.245
Main Landing Gear: Tire/ Rim Mass [kg]	90.2/ 74.4

All in this section selected and derived parameters are summarized in Table 2-3. This table states the most important input parameters for the ETS sizing process.

2.3 Drive Cycle Analysis and Requirements Definition

One of the most important phases in designing a fully functional system that works as desired is the definition process of appropriate design requirements. This general statement is universally applicable and applies to any product or system design process. In order to derive requirements that yield a satisfying ETS design, 36 real life conventional aircraft taxi driving profiles, also called: drive cycles[3] or driving cycles, were recorded with a GPS device. In a first step 19 takeoff and 17 landing driving profiles are evaluated to analyze the performance of conventional aircraft taxiing. Secondly, performance parameters for the chosen midsize aircraft are selected in compliance with the ambition to satisfy the kinematic performance demands for a majority of the available drive cycles; equivalent performance design approach.

2.3.1 Taxiing Drive Cycles

Between December 2013 and June 2015, multiple aircraft's velocity versus time profiles while moving on-ground before takeoff and after touchdown had been recorded for a variety of different conventional taxi operations. The driving profiles were logged by a GPS device across various airports in North America and Central Europe. In total, 36 taxiing driving cycles had been recorded. The locations where the drive cycles were recorded are listed in Table 2-4.

---

[3] The drive cycles in this case had been velocity versus time profiles.

Table 2-4 - Available Drive Cycles

Airports for Takeoff Drive Cycles (number of drive cycles available) 19	Airports for Landing Drive Cycles (number of drive cycles available) 17
Berlin-Tegel (TXL), Germany (4)	Berlin-Tegel (TXL), Germany (2)
Calgary (YYC), Canada (1)	Brussels (BRU), Belgium (2)
Dallas/Fort Worth (DFW), USA (2)	Calgary (YYC), Canada (1)
Frankfurt Main (FRA), Germany (1)	Dallas/Fort Worth (DFW), USA (2)
Hamilton (YHM), Canada (1)	Frankfurt Main (FRA), Germany (2)
London Heathrow (LHR), UK (2)	London Heathrow (LHR), UK (1)
Munich Airport (MUC), Germany (1)	Munich Airport (MUC), Germany (2)
Toronto Pearson (YYZ), Canada (6)	Seattle Tacoma (SEA), USA (1)
Washington Dulles (IAD), USA (1)	Toronto Pearson (YYZ), Canada (2)
	Vancouver (YVR), Canada (2)

Figure 2-1 to Figure 2-8 display four representative drive cycle profiles. Two different examples of takeoff drive cycles and their respective GPS tracking can be seen from Figure 2-1 to Figure 2-4. Figure 2-5 to Figure 2-8 represent two different touchdown cycles.

In the Berlin drive cycle (Figure 2-1, Figure 2-2) the aircraft stands at the gate initially; holding phase before pushback. From 25 to 80 seconds the aircraft experiences the push back phase which is indicated by a low speed phase. Once the tractor is uncoupled from the aircraft’s nose gear, the aircraft remains still standing since the main engines need to warm up before the conventional taxi process can be initiated. At the point where the main engines reach their desired temperature the plane leaves the gate which marks the starting point for the takeoff taxi process (after 220s). In this phase the aircraft is powered purely by the main engines. The plane taxis to the runway without any stop but with frequent changes in its taxi speed which lead to changing acceleration and deceleration events. At the point where the aircraft reaches the runway it stops shortly to wait for the takeoff approval coming from the tower. Once takeoff is granted the plane enters the takeoff phase and leaves the airport. This drive cycle is a good example of a takeoff taxiing process with no stops while moving forward. The initial pushback phase was actually done in reverse moving direction but the GPS device could .not capture this while it was recording.

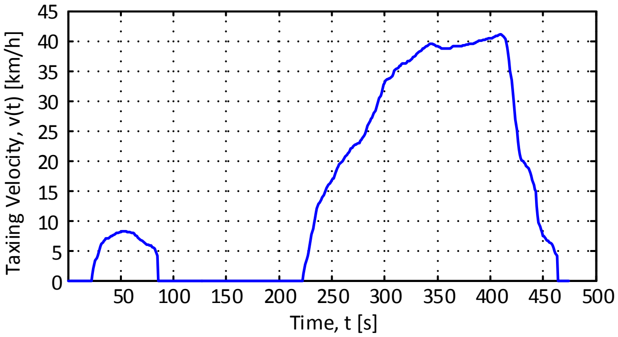

Figure 2-1 – Berlin Tegel Airport, Germany – Takeoff Drive Cycle No. 2

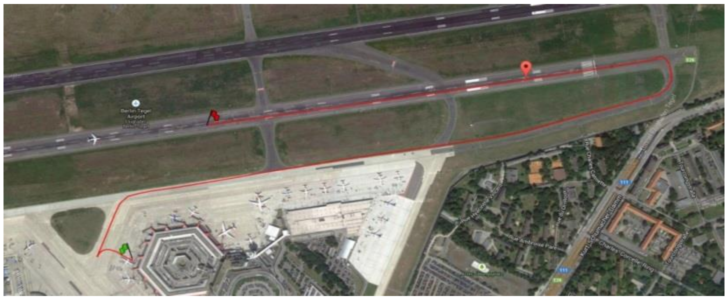

Figure 2-2 – Berlin Tegel Airport, Germany – Takeoff Drive Cycle No.2 (GPS Tracking)

The Hamilton takeoff drive cycle (Figure 2-3, Figure 2-4) is an example of a drive cycle with multiple stops before taking off. After an initial push-back phase (40s to 120s), the aircraft stops at several intersections on ground in order to let other, simultaneously operating aircraft pass its taxiway.

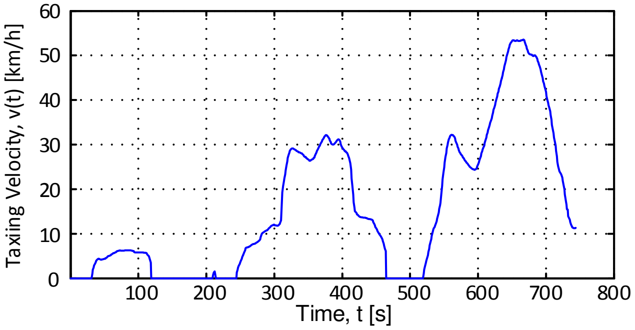

Figure 2-3 - Hamilton International Airport, Canada – Takeoff Drive Cycle

Figure 2-4 - Hamilton International Airport, Canada – Takeoff Drive Cycle (GPS Tracking)

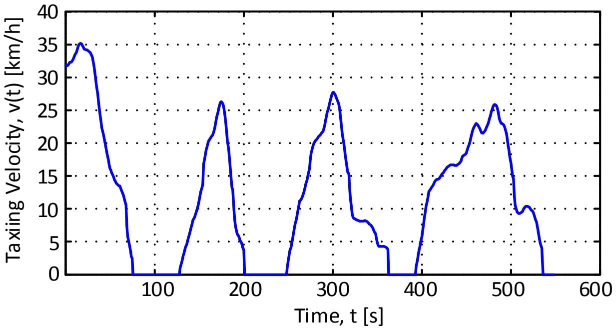

Figure 2-5 - Dallas/Fort Worth Airport, USA – Landing Drive Cycle No. 1

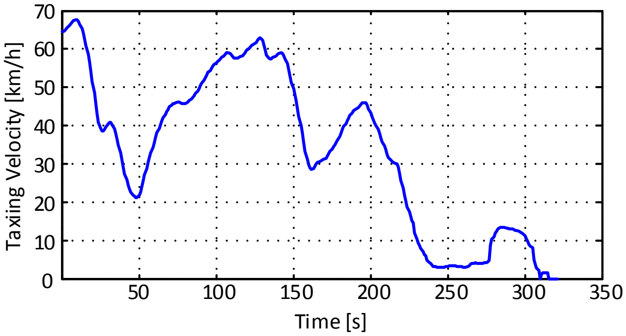

Figure 2-6 - Munich Airport, Germany – Landing Drive Cycle

Figure 2-5 and Figure 2-6 represent two different landing drive cycles. The Dallas driving cycle is an example of a cycle with frequent stops which reaches taxiing top speeds of around 30km/h. The Munich landing taxi cycle, contrary to the Dallas cycle, is a smooth taxi profile with no stops during the actual taxi-in phase which reaches high taxi speeds beyond 60 km/h. The only existing stopping event in the Munich landing profile is the point where the aircraft reaches its final holding position in front of the terminal (after 310s).

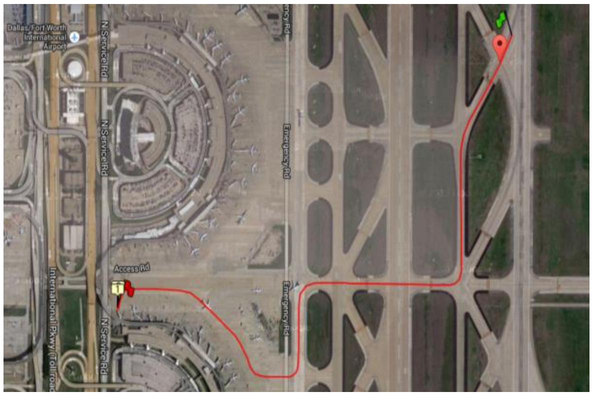

Figure 2-7 - Dallas/Fort Worth Airport, USA – Landing Drive Cycle No. 1 (GPS Tracking)

Figure 2-8 - Munich Airport, Germany – Landing Drive Cycle (GPS Tracking)

Based on these four example drive cycles, it can be seen that taxiing can follow different patterns depending on the airport's infrastructure and the on-ground traffic conditions. The possession of taxi driving profiles allows system designers to perform a detailed performance analysis. These analysis results can then be used to derive performance requirements for an ETS.

2.3.2 Kinematic Analysis and Requirements Definition

In order to derive an ETS that provides sufficient performance for electric taxiing, a four-step sizing procedure was applied. Initially all recorded landing and takeoff driving profiles are analyzed to quantify the taxi behavior of modern conventional taxiing. With the knowledge of these taxi characteristics the performance requirements are then defined. In the following step an ETS for an Airbus A321 commercial aircraft is then sized. The outcomes of the sizing phase are top-level ETS powertrain component specifications which are commonly used to enter the actual component design phase. Finally, the proposed ETS is tested against all available drive cycles to confirm that the proposed system can deliver a competitive performance when compared with conventional taxiing. To test the electric powertrain for taxi operations, a custom simulation model was designed that allows implementing the performance characteristics of the developed ETS. With the simulation tool the effectiveness of the powertrain sizing process can be evaluated. Moreover, the simulation tool is able to provide estimated values for the energy consumption of the complete ETS powertrain and its major components such as electric motors, inverters, energy storage system, etc. The simulation model was designed by MATLAB/ Simulink [57].

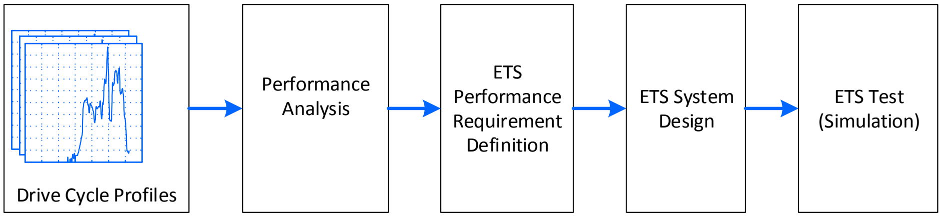

Figure 2-9 - ETS System Sizing Phases

As mentioned earlier a drive cycle analysis is necessary to derive proper ETS design requirements. By studying the given driving profiles for different takeoff and landing taxi operations, the following key parameters were determined for each available driving profile:

- Maximum taxi speed/ velocity v_{max},
- Peak taxiing acceleration a_{max},
- Peak traction force (product of assumed aircraft's dynamic mass m_i and the peak taxiing acceleration a_{max}) F_{TM},
- Maximum traction power P_{TM}.

To facilitate the study of important conventional taxi parameters, an easy-to use simulation model has been created (Figure 2-10).

The drive cycle analysis model which was designed within MATLAB/ Simulink uses the different velocity over time profiles for each drive cycle as a simulation input. The outputs from this simulation are several kinematic parameters, such as acceleration, velocity, tractive force, and tractive power, that are important for the subsequent performance requirements definition phase.

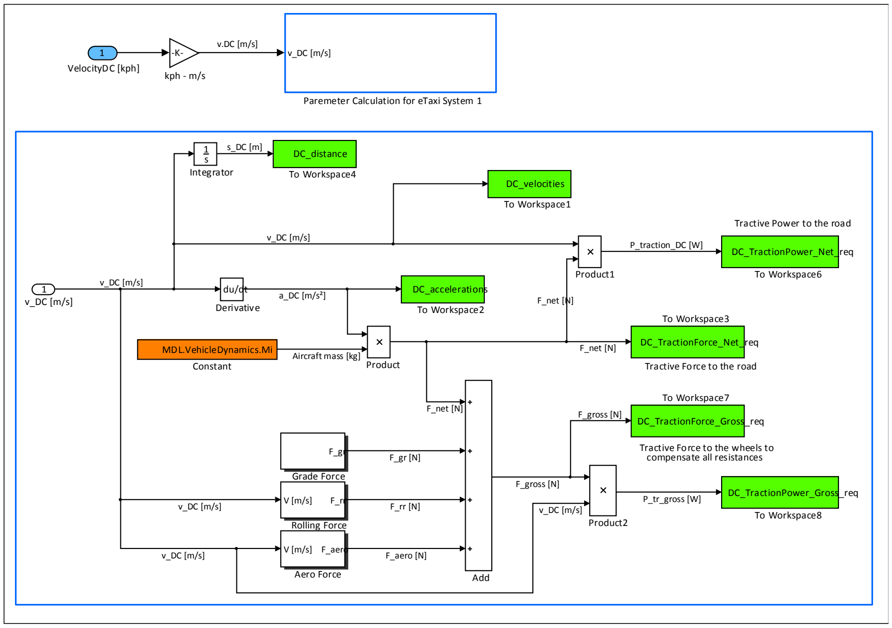

Figure 2-10 - Drive Cycle Analysis Simulink Model

On the basis of the currents aircraft taxi velocity $v(t)$ the acceleration $a(t)$ and the current driving cycle taxi distance $d(t)$ can be calculated by derivation and integration of the instantaneous taxiing velocity.

$$d(t) = \int_{t_0}^{t} v(t)\, dt$$

$$a(t) = \frac{d}{dt} v(t)$$

The current traction force $F_T(t)$ was computed by using the estimated dynamic aircraft mass m_i and the current taxi acceleration $a(t)$, according to Newton's Second Law of Motion.

$$F_T(t) = m_i \cdot a(t)$$

The instantaneous tractive power $P_T(t)$ was then determined as the product of the current traction force $F_T(t)$ and the instantaneous taxi velocity $v(t)$.

The tractive force and power have further been divided in net and gross parameters to distinguish between the performance that is to be expected to the road (net) and the performance that was delivered to the wheels (gross). A more in-depth explanation on these differences will be addressed in the upcoming ETS sizing section. For the initial drive cycle analysis it was focused on net performance numbers. Therefore only the performance to the road (net parameters) has been assessed in the beginning.

The extreme values from all kinematic drive cycle analysis simulations[4] are displayed in Table 2-5. These results indicate the peak conventional taxi performances which the intended ETS should target ideally. Unfortunately, an ETS with such a superior performance would be strongly oversized and extremely difficult to fit into the actual available space in the chosen aircraft's undercarriage. Therefore these analysis results cannot directly be transferred into ETS design requirements. Nonetheless, the extreme values from all analyzed conventional taxiing cycles have been listed in Table 2-5 to provide information on modern taxiing peak performances.

Table 2-5 – Drive Cycle Analysis Results: Extreme Values

Parameter [unit]	**Takeoff Cycles**	**Landing Cycles**
Peak acceleration a_{max}	**1.14 m/s²** (Hamilton 1)	1.083 m/s² (Munich 1)
Max. taxiing velocity v_{max}	61.8 km/h (Dallas 2)	**67.6 km/h** (Munich 1)
Max. traction force $F_{trMaxPeak}$	**104 kN** (Hamilton 1)	98.9 kN (Munich 1)
Peak traction power $P_{trMaxPeak}$	**584.8 kW** (Frankfurt 1)	539.92 kW (Toronto 2)

Even though the above mentioned peak performance figures from the conventional drive cycle data analysis were not used directly as ETS performance

---

[4] Detailed kinematic analysis results for every available drive cycle are shown in the Appendix, section Drive Cycle Analysis Results

requirements, these numbers were still utilized to derive adequate system performance requirements.

So as to avoid proposing a heavily oversized ETS and for the purpose of compensating possible GPS tracking errors, that might arise due to emitter/ receiver disturbances and the actual device's receiving tolerance, the 85 %-quantile values of the extreme values in Table 2-5 were selected. By using a x %-quantile value will ensure that x % of all given drive cycle performance demands will be satisfied by the ETS. Consequently, using the 85 %-quantile is a popular way to cut out possible measurement errors and outliers that had been accidentally recorded by using a measurement device. The 85%-quantile numbers for the key performance parameters are listed in Table 2-6.

Table 2-6 – Drive Cycle Analysis Results: 85%-Quantiles

85%-quantile value	**Takeoff Cycles**	**Landing Cycles**
Peak acceleration $a_{0.85}$	**0.93 m/s²**	0.89 m/s²
Max. taxiing velocity $v_{0.85}$	48.43 km/h	**57.6 km/h**
Max. traction force $F_{TM0.85}$	**84.5 kN**	81.6 kN
Peak traction power $P_{TM0.85}$	367.54 kW	**431.96 kW**

Because of the fact that the ETS needs to operate during the takeoff and landing taxi phase, the maximum values for each 85%-quantile performance number, shown in Table 2-6, must be respected. This in turn yields the ETS performance requirements that are the foundation for the subsequent electrified ground propulsion system sizing. The obtained system design requirements are summarized in Table 2-7.

Table 2-7 - ETS Performance Requirements

ETS Performance Requirement	**Value [unit]**
Max. Acceleration at the wheel a_{Wm}	0.93 m/s²
Max. Velocity at the wheel v_{Wm}	58 km/h
Max. tractive force to the road F_{Tm}	85 kN
Max. wheel tractive power to the road P_{Tm}	432 kW

2.4 ETS Powertrain Sizing

With the knowledge of appropriate system design requirements such as the ones that were derived in the previous section, a powertrain can be sized that provides the desired performance to the road. In the case that the ETS will not be able to achieve the demanded performance, it will not have the capabilities to compete with conventional taxi operations when on-ground dynamics are considered.

The following section discusses the powertrain component sizing phase to provide the desired ETS taxi performance with the selected Airbus A321 commercial aircraft. The top-level ETS powertrain layout is illustrated in Figure 2-11. The system will operate as described in the following paragraph.

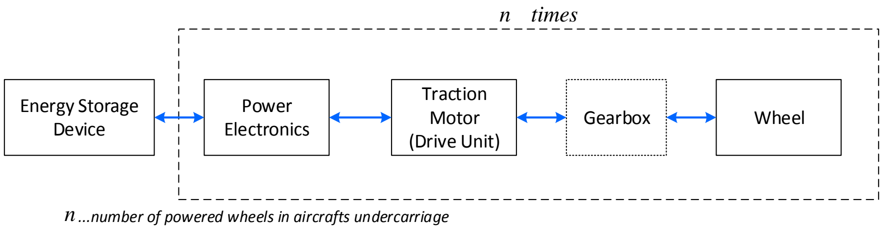

Figure 2-11 - ETS top-level powertrain layout

The electrical energy storage device supplies the amount of electrical power that is requested by the power electronics. The power electronics, which at a minimum contain a motor controller, will ensure that the right amount of electrical power is being sent to each drive unit in order to satisfy each traction motors power request. Per aircraft wheel that is supposed to be powered by a traction motor, a gear reduction might be used to step up the motor output torque while decreasing its speed. The usage of a gearbox heavily depends on the ETS's shape and will be analyzed in this chapter. Finally, the mechanical power which is put out by the motors and gearbox, if one is used, will be transmitted to the corresponding wheel to propel the target aircraft purely electric. In case that multiple powered wheels are required to provide the desired taxi performance, the above described powertrain will be duplicated as many times as it is necessary. The only unit which will not be duplicated is the energy storage device, since this design intends to use one energy storage unit for the complete system.

In the following the ETS sizing process is conducted with the main goal of quantifying the traction motor, motor controller and energy storage system specifications. Furthermore, the number of needed powered wheels in the Airbus A321's undercarriage for electric taxiing is assessed.

2.4.1 Friction and Maximum Traction Analysis

This first analysis part will determine how much force can be delivered to the different wheels in the aircraft's undercarriage. The results of this study determine where the ETS must be placed, FG or MLG, in order to deliver the desired on-ground taxi performance.

Maximum traction in this context describes the tractive force F_T at which a tire starts to skid. That is, when the tire will not be able to push itself off the tarmac anymore. Translated into a kinematic criterion, the maximum traction is reached once the instantaneous tractive force F_T overcomes the static friction force for rubber on tarmac/ asphalt. The static friction force will be called adhesion force F_{adh}. For any tractive force lower than the adhesion force a proper dynamic operation can be expected; the tire will not begin to skid.

Tire skid:

$$F_T > F_{adh} \tag{12}$$

Tire adhesion (no skidding):

$$F_T \leq F_{adh} \tag{13}$$

The adhesion force is defined as the product of the aircraft's weight W and the static friction coefficient COF. Especially the latter depends strongly on the material combination that is used to transmit the tractive force. Furthermore, this coefficient also depends on the weather conditions, the ambient temperature, and many other factors. When a vehicle for instance should be accelerated on dry asphalt or an icy road a noticeable difference in maximum transmittable tractive force before tire skidding can be experienced.

Applied to the selected midsize aircraft a study was conducted to evaluate the maximum transmittable tractive force to the FG or MLG within the undercarriage for three different weather conditions.

From previous studies it was found that 90 % of the total Airbus A321's mass is centered above the MLG and the remaining 10 % are supported by the Nose Gear [39]. With this weight distribution factor WD for the FG ($WD = 0.1$) and MLG ($WD = 0.9$), the maximum transmittable traction force F_{Tt} for each respective gear within the aircraft can be determined.

$$F_{Tt} = f(WD, COF)$$

$$F_{Tt} = W \cdot WD \cdot COF \tag{14}$$

The weight force W is defined by multiplying the total aircraft mass m_{tot} (Table 2-3) with the gravitational acceleration g.

Table 2-8 depicts the analysis results for the maximum transmittable traction force F_{Tt} in dependency of the weather conditions and the location in the aircraft's undercarriage (FG or MLG).

The results from the maximum wheel traction study lead to the decision to select the MLG for the ETS integration. The integration of the electric taxi system into the FG would impose an undesirable traction force limitation on the maximum tractive force to the road. Not one of the three weather scenarios, not even ideal conditions of running tires on dry tarmac, allow the output of 85 kN peak tractive force to the wheels as it is demanded from the performance requirements that were presented in Table 2-7.

Table 2-8 - Maximum Wheel Traction: Analysis Results

Parameter	**Dry Conditions (optimum)**	**Wet Conditions (intermediate)**	**Snow and Ice (worst-case)**
COF (static friction coefficient)	0.8 [39]	0.25-0.75 (0.4 used) [58]	0.12 (at 0°C) [59]
FG - Max. Tractive Force (complete FG, two tires)	71.06 kN	35.53 kN	10.66 kN
MLG - Max. Tractive Force (complete MLG, four tires)	639.5 kN	319.75 kN	95.93 kN

The MLG instead allows transmitting the required tractive force of 85 kN to the ground even under the most challenging weather conditions such as snow and ice. This is beneficial to increase the aircraft's controllability in critical situations, such as avoiding tire-slip in case of bad conditions, e.g. rain or snow on the taxiways' [51]. Due to the high amount of mass that is supported by the MLG, the ETS will be integrated into the aircraft's MLG.

For ideal taxi conditions, i.e. tires moving on dry tarmac, the following maximum tractive forces for the Airbus A321 have been determined. According to Table 2-8 the maximum allowable tractive force F_{Ttc} for the complete MLG results in:

$$F_{Ttc} = 639.5\ kN\ . \tag{15}$$

Since the MLG is comprised of four wheels in total, each wheel will allow a peak tractive force F_{Ttw} which is equivalent to the peak tractive force for the complete MLG F_{Ttc}; assuming the weight is equally distributed among all four wheels within the MLG.

$$F_{Ttw} = 159.9\ kN \tag{16}$$

2.4.2 *Ground Dynamics and Performance to the Wheels*

To examine the dynamic behavior of the aircraft while, it is mandatory to analyze the forces that act on the aircraft while taxiing. From the previous section the location of the desired ETS as well as the performance to the road numbers had been obtained. In this thesis the performance to the road will be called "net performance" since it does not take motion resistances into account such as rolling resistance, grade resistance and the aerodynamic resistance (also called "drag"). The performance that needs to be supplied in order to compensate all applied resistances while still ensuring that the requested net performance is being send to the road, is called "gross performance". Calculating this gross performance is of significant importance to decently size the ETS powertrain.

Summarizing, gross parameters are the sum of net parameters plus all applicable resistances that need to be compensated.

When the aircraft's taxiing motion dynamics are analyzed the relationship between gross and net performance becomes apparent. A free body diagram visualizing the aircraft's on-ground dynamics is depicted in Figure 2-12.

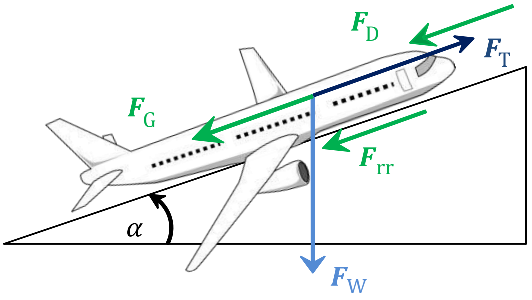

Figure 2-12 - Aircraft On-Ground Dynamics: Free Body Diagram

F_T describes the instantaneous tractive force to the road (net tractive force), F_{rr} stands for the rolling resistance of the aircraft while taxiing, F_D

symbolizes the aerodynamic drag, and F_G illustrates the grade resistance. F_W is the aircraft's weight which is defined as the product of the aircraft's static mass m_{stat} and the gravitational acceleration g ($9.81 \frac{m}{s^2}$).

Based on Newton's 2nd Law of Motion the gross tractive force $\hat{\mathrm{F}}_{\mathrm{T}}$ had been determined. Again, $\hat{F}_T$ must be capable to compensate all applied resistances in order to employ the desired net tractive force to the road F_T. Thus, $\hat{F}_T$ must equal the net tractive force F_T plus all ground motion resistances:

$$\hat{F}_T = F_T + \underbrace{(F_{rr} + F_G + F_D)}_{Resistances} \tag{17}$$

Rolling Resistance:

The aircraft's rolling resistance F_{rr} can be approximated by multiplying the weight F_W with the so called rolling friction coefficient c_{rr}.

$$F_{rr} = F_W \cdot c_{rr}$$

Since $F_W = m_{stat} \cdot g$, the rolling resistance results in:

$$F_{rr} = m_{stat} \cdot g \cdot c_{rr} \ . \tag{18}$$

The rolling friction coefficient c_{rr} follows a similar dependency on the material contact between two components as the static friction coefficient's COF. This behavior was explained in the Friction and Maximum Traction Analysis section.

For the material combination of a rubber tire on dry asphalt the rolling friction coefficient c_{rr} can be assumed to equal 0.009 according to [60]. For the chosen aircraft with its static mass according to Table 2-3 this yields a constant rolling resistance F_{rr} of:

$$F_{rr} = 7.994\ kN\ . \tag{19}$$

Even though the rolling friction coefficient depends on a variety of influencing factors such as the wheel speed, the tire pressure, the road conditions and the temperature, etc. [61] it is commonly assumed as a constant.

Aerodynamic Drag:

Another resistance acting on the aircraft while moving, is the aerodynamic resistance. Its magnitude depends on the current taxiing velocity v, the density of air ρ_{air} (1.2 kg/m^3 at 20°C), and the aircraft's drag coefficient c_D times the active frontal area A_{ref}.

$$F_D = f(v)$$

$$F_D = \frac{\rho_{air} \cdot c_D \cdot A_{ref} \cdot v^2}{2} \tag{20}$$

The density of air will be assumed to stay constant and the Airbus A321's specification for the product of $c_D \cdot A_{ref}$ is listed in Table 2-3. The maximum drag F_{Dm} that the airplane will face can be determined if the maximum taxi velocity of 58 km/h (Table 2-7) is substituted for v in eq. (20).

$$F_{Dm} = 404.93\ N \tag{21}$$

Grade Resistance:

The last resistance that will affect the available net traction force to the road F_T is the grade resistance F_G. This resistance comes from moving the aircraft uphill, i.e. a ramp that separates an airport's apron from the taxiway or equivalent.

If the grade of a ramp in percent gr is known, then the angle of climb α (Figure 2-12) can be derived by:

$$\alpha = \arctan\left(\frac{gr}{100}\right) .$$

The maximum allowable ramp grade gr_m on an airport is standardized and depends on the airplane type that is supposed to move along a certain paths on the airport's on-ground infrastructure. According to the so called ICAO Aerodrome Reference Code which classifies aircraft into different groups, a maximum allowable ramp grade is imposed. For the chosen Airbus A321 the maximum allowable ramp grade is 1.5 % according to [62].

Overall, the grade resistance F_G depends on the aircraft's weight F_W and the angle of climb α [3] and can be computed with eq. (22).

$$F_G = \sin(\alpha) \cdot F_W \tag{22}$$

Although the grade was set to zero which equals to no grade resistance in the ETS powertrain sizing process, its calculation was still described to allow the implementation of this factor in future studies.

<u>Maximum Gross Tractive Force (Force to the Wheels):</u>

The maximum gross tractive force $\hat{F}_{Tm}$ for an aircraft taxiing on perfectly ground (no grade resistance: $F_G = 0$) was determined on the basis of the maximum traction force to the road F_{Tm} (Table 2-7), the rolling resistance according to eq. (19), and the maximum drag F_{Dm} (eq. (21)).

$$\hat{F}_{Tm} = F_{Tm} + F_{rr} + F_{Dm}$$

$$\hat{F}_{Tm} = 85\ kN + 7.994\ kN + 0.405\ kN$$

$$\rightarrow \hat{F}_{Tm} = 93.4\ kN \tag{23}$$

Maximum Required Torque to the Wheels

With the above calculated gross tractive force $\hat{F}_{Tm}$ the maximum required ETS torque to the wheels T_{ETSwm} had been calculated. Utilizing the diameter of a single tire within the Airbus A321's MLG d_{tMLG} that is stated in Table 2-3 and $\hat{F}_{Tm}$ yields:

$$T_{ETSwm} = \hat{F}_{Tm} \cdot \frac{d_{tMLG}}{2}$$

$$T_{ETSwm} = 58.142\ kNm \quad . \tag{24}$$

Equation (24) indicates that the complete ETS must be capable to produce up to 58 kNm of torque to the wheels to supply the desired performance to the road.

2.4.3 Maximum Power Investigation

The required peak power to the road P_{Tm}, according to Table 2-7, is input to the maximum ETS power analysis. One method to determine the peak tractive force to the wheels (gross) can be based on the demanded peak gross tractive force $\hat{F}_T$ and the instantaneous taxi velocity of the aircraft v:

$$\hat{P}_T = \hat{F}_T \cdot v$$

To estimate the peak gross tractive power of the ETS one could assume that the peak gross tractive force $\hat{F}_{Tm}$ coincides with the peak taxiing velocity v_{Wm} of 58 km/h (Table 2-7). However, such an approximation yields a largely oversized ETS because of the fact that the peak gross tractive force $\hat{F}_{Tm}$, which is the result of the maximum acceleration of the aircraft while taxiing, must not necessarily concur with the aircraft's top taxi speed v_{Wm}.

For this reason, it was chosen to follow a more accurate gross traction power estimation process. This approach is similar to the way how the ETS powertrain requirements have been developed. By using the kinematic aircraft analysis model that was presented in Figure 2-10, the Airbus A321 was simulated across all available driving profiles (Table 2-4).

By implementing all motion resistances, eq. (18), (20), (22), that counteract the actual required tractive force to the wheels, the gross tractive force was computed for every simulation time step across all available drive cycles according to eq. (17). The simulation outcome is a demanded gross power $\hat{F}_T$ versus drive cycle time t_{DC} profile. In a final step the gross tractive force profiles were multiplied with the velocity profile of each corresponding drive cycle to obtain the true gross tractive power profiles. One example gross power demand over drive cycle duration plot is depicted in Figure 2-13

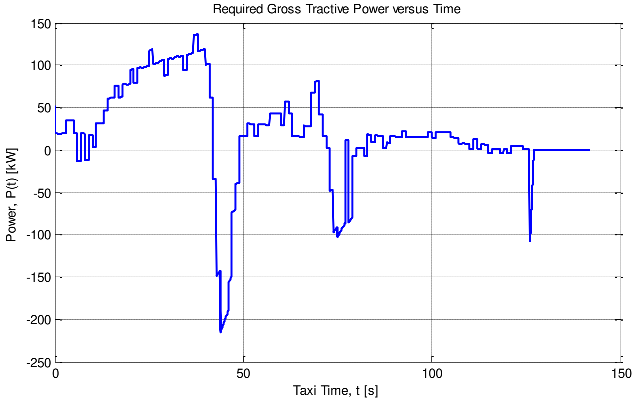

Figure 2-13 –Brussels Landing 2: Gross Traction Power Profile

As it was done before to derive the required ETS performance numbers to the road, the 85 %-quantile values of the peak gross power $\hat{P}_{Tm}$ had been derived for both all takeoff and landing driving profiles. The maximum value from all landing and takeoff gross tractive power distributions has been selected as the peak power to the wheel result that the ETS needs to provide.

With the drive cycle analysis tool results, it was determined that the complete ETS must be capable of applying up to 491 kW of peak tractive power to the wheels.

$$\hat{P}_{Tm} = 491\ kW \tag{25}$$

Table 2-9 – Peak Gross Power Results from Drive Cycle Analysis

Takeoff Cycles **peak power to the wheel $\hat{P}_{Tm0.85}$**	**Landing Cycles** **peak power to the wheel $\hat{P}_{Tm0.85}$**
446.76 kW	490.72 kW

2.4.4 Gearbox Investigation

A transmission system within the proposed powertrain appears to be required due to the high torque at the MLG wheels demand of 58 kNm; see eq. (24). When direct drive applications for such traction requirements are analyzed, it becomes apparent that electric machines with almost 60 kNm peak torque and up to 491 kW peak power do not exist for the available space in a MLG wheel within an Airbus A321; rim diameter: circa 0.5 meter, tire diameter: approximately 1.25 meter according to Table 2-1. Even if a direct drive application with four motors is considered, i.e. each MLG wheel housing one motor for propulsion, then the required motor specifications would still exceed the state of the art available motor technology. A direct drive system without a gearbox and four electric machines, one machine per MLG wheel, would still require a mechanical peak output torque of around 15 kNm per motor. Unfortunately, there is no such motor available as of today that provides this superior performance while still fitting in the rim of an Airbus A321 MLG wheel.

Since direct drive motor applications without a gear reduction can therefore be excluded from the pool of feasible solutions, a torque converter unit must be considered to primarily decrease the torque demand of the respective drive units.

As to choose a suitable torque converter unit, gearboxes were considered. Among all different gearbox variants, special attention was devoted to planetary gearbox systems due to their low weight to high gear reduction ratio (torque conversion ratio), their small size coupled with low losses per stage, and the characteristic that the gearbox input is coaxial to the gearbox output. According to [63] single stage planetary transmissions with gear ratios k of up to 13 can be built without sacrificing the high efficiency of these transmission systems.

For the proposed ETS a single stage planetary gearbox with a gear ratio $k = 12$ was selected. Since the German Aerospace Center (DLR) already designed and build a nose gear ETS which was capable of housing a two-stage planetary gearbox with a gear ratio of 12 [34], it was assumed that a gearbox with the same gear ratio can be integrated in the MLG of an even larger aircraft.

The drawback of using a gearbox is the property of transmission systems that the rotational speed of the gearbox output will decrease by the same ratio k with whom the motor's output torque will increase. Furthermore, the implementation of a gearbox will slow down the powertrain dynamics as well as it will contribute to additional loss generation within the ETS when operating.

The gear ratio k is generally defined as follows:

$$k = \frac{T_{out}}{T_{in}} = \frac{\omega_{in}}{\omega_{out}} \tag{26}$$

Here, T_{in} and T_{out} describe the input and the output torque of a transmission unit respectively. The variable ω_{in} as well as ω_{out} correspond to the transmission's input and output angular velocities. With the chosen gear ratio k of 12 the transmission's output torque can be stepped up by a factor of 12 whereas the peak angular velocity of the electric machine's rotor will exit the gearbox with 1/12th of its magnitude.

2.4.5 Traction Motor Specifications

This paragraph covers the traction motor number selection as well as the single electric machine specifications that are required to deliver the desired ETS taxi performance.

The peak system torque for the complete ETS in front of the transmission T_{ETStm} can be calculated by the use of the definition of the transmission gear ratio k, eq. (26), and the maximum required ETS torque to the wheels T_{ETSwm} (eq. (24)):

$$k = \frac{T_{out}}{T_{in}} = \frac{T_{ETSwm}}{T_{ETStm}}$$

$$\rightarrow T_{ETStm} = \frac{T_{ETSwm}}{12}$$

$$T_{ETStm} = 4845.17\ Nm\ . \tag{27}$$

This peak torque must be supplied by the ETS, no matter how many electric motors will be used to move the aircraft.

The ETS's peak power that is input to the transmission unit P_{ETStm} can be derived based on the gearbox efficiency η_T and the peak power to the wheel $\hat{P}_{Tm}$ that was presented in eq. (25).

$$\eta_T = \frac{P_{Tout}}{P_{Tin}} = \frac{\hat{P}_{Tm}}{P_{ETStm}}$$

P_{Tout} and P_{Tin} symbolize the transmission output and input torque.

With an assumed efficiency for a single stage planetary gearbox system of 96 % ($\eta_T = 0.96$), P_{ETStm} was computed.

$$P_{ETStm} = \frac{\hat{P}_{Tm}}{\eta_T}$$

$$P_{ETStm} = 511.46\,kW \tag{28}$$

The needed peak rotational speed at the transmission input n_{TIm} can be calculated with the required peak taxi velocity at the wheels v_{Wm}that is listed in Table 2-7.

Initially the maximum rotational speed at the wheels n_{Wm} in revolutions per minute (rpm) must be determined by utilizing the Airbus A321's MLG tire diameter d_{tMLG} that is stated in Table 2-3:

$$n_{Wm} = \frac{\omega_{Wm}}{2\pi} = \frac{v_{Wm}}{2\pi \cdot \left(\frac{d_{tMLG}}{2}\right)} \tag{29}$$

$$n_{Wm} = 4.12\frac{1}{s} = 247.15\,rpm \tag{30}$$

With the maximum wheel rotational speed n_{Wm} and the definition of the transmissions gear ratio k (eq. (26)), n_{TIm} can be calculated. Since the angular velocity ω is defined as the product of 2π and the rotational speed n, the following relationship was obtained:

$$k = \frac{\omega_{in}}{\omega_{out}} = \frac{2\pi \cdot n_{in}}{2\pi \cdot n_{out}}$$

$$\rightarrow n_{in} = k \cdot n_{out}\,. \tag{31}$$

Applying eq. (31) yields:

$$n_{TIm} = k \cdot n_{Wm}$$

$$n_{TIm} = 2965.78\,rpm\,. \tag{32}$$

The overall findings for the total ETS system's performance have been summarized in Table 2-10. The system needs to have the capability to apply the indicated torque, power and speed demands to the transmission input. Therefore, the electric traction motors must be selected or even designed accordingly.

Table 2-10 – ETS Performance Numbers (System Level)

ETS Specification	**Value [Unit]**
Peak Torque to Transmission T_{ETSm}	4850 Nm
Peak Power to Transmission P_{ETSm}	512 kW
Maximum Rotational Speed (Transmission Input) n_{ETSm}	2970 rpm
Transmission Gear Ratio (Single Stage) k	12

Since the Airbus A321 MLG consists out of four wheels that are integrated into two MLG wheel assemblies, up to four motors can be integrated in the aircraft’s MLG. As a result, a study was executed to determine the effect of multiple motors and their respective performance specification requirements.

Only the both options with two or four electric machines in the MLG had been analyzed in order to ensure the system’s symmetry and to maintain the aircraft’s balance. Since the ETS is an on-board system it will affect the flight performance. Thus, unbalanced ETS layouts were disregarded. Furthermore, ETSs that possess only one traction unit would not be capable to improve the aircraft’s maneuverability because such architecture would not allow the aircraft to rotate around its center of mass. Since this system feature is desired to strongly increase the craft’s flexibility for on-ground operations, single motor architectures were not considered as well. Using at least one motor per MLG wheel assembly allows additionally to control each MLG wheel assembly independently which can improve the cornering performance.

Assuming that m numbers of motors are used within the powertrain, then the peak motor output torque T_{Mm} and the peak power demand for each electric motor P_{Mm} result in:

$$T_{Mm} = \frac{T_{ETSm}}{m} \tag{33}$$

$$P_{Mm} = \frac{P_{ETSm}}{m} \ . \tag{34}$$

The maximum rotational speed for a single motor n_{Mm}, no matter how many motors will be used within the proposed ETS, must always be capable of providing the maximum required taxi velocity. Therefore, every motor must be able to spin up to the maximum rotational speed of the total ETS n_{ETSm}:

$$n_{Mm} \equiv n_{ETSm} \ . \tag{35}$$

The comparison between using two or four traction motors within the ETS is shown in Table 2-11.

Table 2-11 - Single Motor Specifications for different ETS Layouts

Motor Parameter	**ETS with 2 Motors** $\boldsymbol{m = 2}$	**ETS with 4 Motors** $\boldsymbol{m = 4}$
Single Motor Peak Torque T_{Mm}	2425 Nm	1213 Nm
Single Motor Peak Power P_{Mm}	256 kW	128 kW
Single Motor max. rot. speed n_{Mm}	2970 rpm	2970 rpm

When the motor parameters for a two or four motor ETS are compared, it becomes apparent that only the powertrain with four electric machines, one motor per MLG wheel, will be a viable option. A single motor with more than 2400 Nm output torque and a peak power of above 250 kW with a top rotational speed of close to 3000 rpm does not exist for the given geometric constraints. A comparison with two high performance permanent magnet motors (PMSM) from YASA [64] and GKN [65] shows that the only possible solution would be an ETS with four electric machines.

Table 2-12 - ETS Motor Comparison 1: YASA-750

YASA-750 Specifications [64]	
Maximum turning speed	3250 rpm
Peak Torque	790 Nm
Peak Power Output (at 700 VDC)	200 kW
Total Mass	33 kg
Diameter	350 mm

Table 2-13 - ETS Motor Comparison 2: GKN AF-240

GKN (EVO Electric) AF-240 Specifications [65]	
Maximum turning speed	5000 rpm
Peak Torque (max. 60sec)	800 Nm
Launch Torque (max. 18sec)	1200 Nm
Peak Power Output (max. 60sec)	335 kW
Total Mass	80 kg
Diameter	400 mm

According to the specifications of the YASA 750 and GKN AF-240 permanent magnet machines it can be seen that the demanded peak power as well as the peak rotational speed are no critical factors and can be provided by commercial motors. The required peak torque for the proposed ETS remains the most critical factor in order to find an electric machine that delivers the desirable taxi performance. It can be seen that the GKN motor is able to provide 1200 Nm for up to 18 seconds. Ultimately, when the AF-240's motor size is taken into account, one can assume that a motor could be designed that provides the desired torque while fitting inside the Airbus A321's MLG wheel rim. Additionally, since the peak torque capabilities depend heavily on the actual cooling strategy of an electric machine it will be assumed that a suitable electric machine can be designed that delivers the desired 1215 newton meter peak torque for at least ten seconds.

This finally yields the traction motor specifications as well as the powertrain layout for the proposed Airbus A321 ETS. A system with four traction motors, all of similar performance, is required to satisfy the design requirements. With a system containing four traction motors that supply the performance specifications which are indicated in Table 2-14, the ETS will perform similarly to today's commercial main engine based taxiing.

Table 2-14 - Airbus A321 ETS: Proposed Traction Motor Specifications

Motor Specifications	
Maximum rotational speed n_M	2970 rpm
Nominal (continuous) Torque T_c	600 Nm
Peak Torque (max. 10 s) T_M	1215 Nm
Nominal (continuous) Power P_c	65 kW
Peak Power Output (max. 60 s) P_{Mm}	130 kW

The continuous power and torque numbers in Table 2-14 were selected to be half the magnitude of their respective peak values. It is desirable that these continuous numbers are as high as possible in order to improve the dynamic behavior of the ETS. However, the definition of nominal motor performance numbers is part of the actual component design phase which will not be addressed in this thesis.

A final schematic on the ETS powertrain layout is outlined in Figure 2-14.

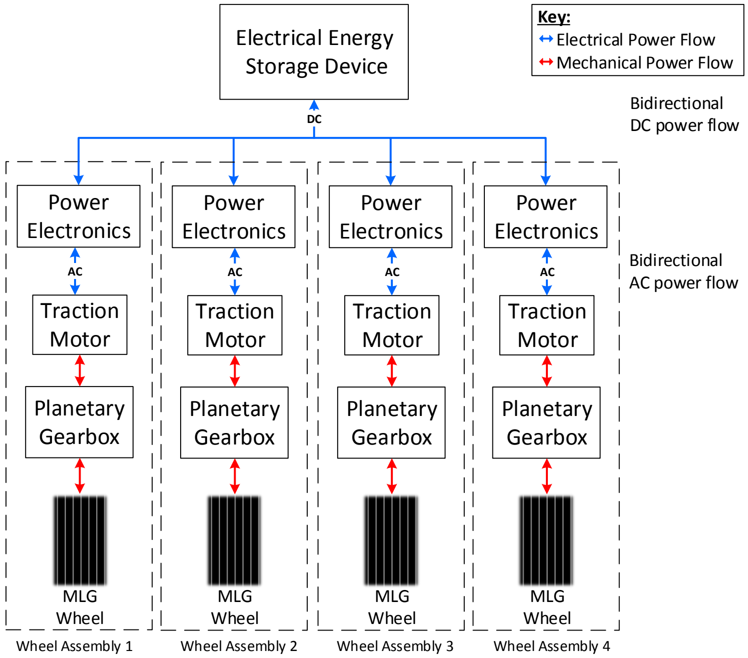

Figure 2-14 - ETS Powertrain Layout

2.4.6 *Motor Controllers*

Motor controllers are part of power electronic systems. For the discussed ETS in this thesis, motor controllers are required to ensure that the traction motors can operate as required. A common motor controller is the so called “inverter” which is used to control three-phase traction motors. A detailed description on the functionality and a design analysis of an inverter for this proposed ETS will be part of the following chapter. At this point, only the required inverter’s peak power output to the electric machine will be investigated P_{Im}.

Assuming that the electric machines will have an average efficiency η_M of 92%, allows estimating the needed peak output power of one inverter.

$$P_{Im} = \frac{P_{Mm}}{\eta_M}$$

$$P_{Im} = 141.3\ kW \tag{36}$$

2.4.7 Energy Source Power Rating

As mentioned previously an electrical energy storage system will be used that is not further specified. Possible electrical energy sources for the ETS are supercapacitors, batteries, fuel cells (electro-chemical), flywheels (electro-mechanical), the airplane's APU or any analogous bidirectional energy source as well as any combination of those.

The energy rating was not determined in this study. It was simply assumed that a large enough energy source will be available to provide the ETS with sufficient power at any time. The energy consumption and size of the energy storage device depends strongly on the chosen storage technology.

In order to provide the drive units (electric machines plus power electronics) with adequate power, the energy storage system's peak power output P_{ESm} must be determined.

To conservatively estimate P_{ESm} the average efficiencies for the traction motor and its respective motor controller were utilized. For this purpose the combined motor – inverter efficiency η_{MI} was assumed to be constant at 86.5 %; average efficiency for motor: 92 % and 94 % average efficiency for the motor controller. This orientation value was assumed based on a given combined efficiency map for a high performance PMSM and its motor controller [66].

The energy storage system's peak power output P_{ESm} was calculated by dividing the ETS's peak power P_{ETSm} with the combined motor-motor controller efficiency η_{MI}:

$$P_{ESm} = \frac{P_{ETSm}}{\eta_{MI}} \ . \tag{37}$$

$$P_{ETSm} = 591.9 \ kW \ . \tag{38}$$

2.4.8 Clutch Mechanism Requirement

Since aircraft commonly touch the runway with above 200 km/h when landing on a destination airport, a clutch must be implemented between the ETS traction units and their respective MLG wheels. The motors were sized to deliver top taxi speeds of 58 km/h which does not enable the ETS to operate at actual touchdown velocities. In order to protect the ETS powertrain from any physical damage, a clutch mechanism or a switchable gear box will be required. The latter variant would be the most desirable option since it could enable the ETS to make use of power regeneration capabilities during touchdown braking. A more detailed discussion on regenerative braking capabilities versus required taxiing performance has been published in [51].

2.4.9 Airbus A321 ETS - Summary

The following table summarizes the findings from this ETS Powertrain Sizing section. All important top level system parameters and specifications are presented in Table 2-15.

Table 2-15 - Airbus A321 ETS Powertrain Specifications (Summary)

ETS Parameter/ Specification	**Value/ Description**
General Specifications	
Number of powered wheels	4
Location of ETS	MLG
ETS maximum velocity	58 km/h
Gearbox	
Number of Gearboxes in ETS	4 (one per MLG Wheel)
Suggested Gearbox Type	Planetary Gearbox
Gear Ratio k	12
Assumed Average Efficiency η_T	96 %
Traction Motors	
Number of Motors in ETS	4
Peak Torque (max. 10 s) T_M	1215 Nm
Peak Power Output P_{Mm}	130 kW (max. 60 s)
Maximum rotational speed n_M	2970 rpm
Assumed Average Efficiency η_M	92 %
Motor Controller (Inverter)	
Number of Motor Controllers	4
Desired Controller Topology	3 phase Inverter
Peak Power Output P_{Im}	141.3 kW
Assumed Average Efficiency η_I	94 %
Electrical Energy Storage System (Electrical ESS)	
Peak power output P_{ESm}	591.9 kW
Capacity in kWh	Not quantified
ESS topology	Not quantified
Assumed Average Efficiency η_{ESS}	90 %

2.5 ETS Simulation

In this section, the previously introduced ETS powertrain is simulated across all available taxiing driving cycles to evaluate the system's performance and to confirm the powertrain sizing process with all the assumptions that had been made to derive component specifications.

Because of the fact that this study puts a special emphasis on the actual taxiing energy consumption of ETSs, the energy consumption will be assessed as well. This information can then be used to support the selection process of a proper electrical energy storage system within the chosen Airbus A321 commercial aircraft and to assess the cost savings when using electric instead of conventional taxiing.

A simulation based analysis, however, requires the existence of a virtual simulation environment that allows the calculation of the system's energy consumption for a set of different taxi driving profiles. Since there is no such MLG ETS powertrain simulation tool commercially available, a custom powertrain simulation tool has been developed in MATLAB/ Simulink.

2.5.1 ETS Simulation Model

A "circuit based Matlab/ Simulink model" in contrast to a "physics based model" was designed to allow the performance study of the proposed ETS. Circuit based in this context describes a model that uses a mathematic signal representation for any physical signal such as mechanical torque, power, speed or electrical voltage, and current. The Simulink model supports a bidirectional power flow between all major powertrain components that were visualized in Figure 2-14 to allow the study of energy recuperation due to regenerative braking.

A conventional taxi driving profile is input to the simulation. The virtual ETS powertrain with its proposed component specifications according to Table

2-15 will then attempt to match the drive cycle while providing top level component outputs as well as system level information, i.e. single motor power versus taxi time, energy consumption versus taxi time to name only a few possible outputs.

The simulation model for the given ETS powertrain is similar to the models that were presented in [3] and [51]. The only powertrain simulation tool modifications that were required had been the adjustment to move from two powered MLG wheels to four and the component specification adaption.

The electric taxing system simulation layout is presented in Figure 2-15.

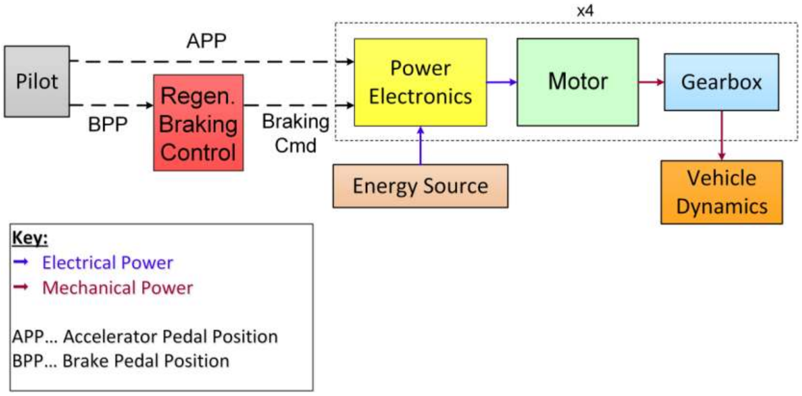

Figure 2-15 – Electric Taxiing System: Simulink Model

The first system from the left, called pilot subsystem, is the simulation's input system and reads the selected taxiing drive cycle in. With respect to the difference between the demanded instantaneous drive cycle velocity and the current aircraft taxiing velocity inside the simulation, an acceleration- or braking command will be generated. The demanded and the current aircraft taxi velocity enter the system and the difference between both velocities will be computed; called velocity error. A PID controller will then use this error in order to produce a respective signal similar to an accelerator (APP) or brake pedal position (BPP). The APP's value can vary between 0 % and 100 % where 0 % means that the aircraft must not be accelerated and 100 % signals that the maximum possible acceleration is requested to match the demanded drive cycle reference velocity. Similarly to the APP, the BPP had been designed to yield values between 0 % (no braking) and -100 % (maximum braking performance required). The Simulink model for the pilot system is shown in Figure 2-16.

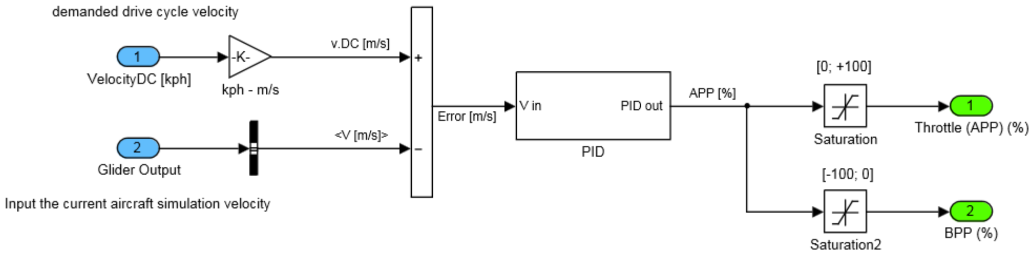

Figure 2-16 - ETS Simulation Model: Pilot System

The following “Regen. Braking Control|” system embodies the braking strategy of the ETS. The overall idea is that the ETS powertrain will attempt to make use of as much regenerative braking as possible rather than using conventional friction based braking instead. Hence, regenerative braking will be applied whenever the requested braking power is below or equivalent to the currently available peak output power of all motors within the ETS. The maximum available peak power of all motors depends on the momentary condition of the electric machines while they are operating. In the event that the pilot’s braking power request cannot be satisfied by all motors within the ETS, the electric machines will provide their maximum available regenerative braking power. The missing braking power will then be supplied by friction based braking to ensure that the proper braking performance can be achieved. This blended braking strategy of friction and regenerative braking allows providing any imaginable braking performance for on-ground taxi operations, while achieving the maximum possible amount of energy regeneration in braking events.

The Power Electronics and Motor systems were actually modeled as one system which was called “Motor Drive System”. A system schematic is presented in Figure 2-17.

System inputs are the accelerator pedal position (APP) in case of acceleration events or the required regenerative braking command coming from the “Regen Brake System” if braking is required. With the APP and the electric motor specifications such as the instantaneous maximum available motor output torque the motor’s output torque is calculated:

$$Motor\ Torque_{Out}(t) = APP \cdot Available\ Peak\ Motor\ Torque_{out}(t).$$

The APP value equals to a scalar within the interval [0; 1]. With the current rotor speed, which in turn is a linearly depended on the taxi velocity, the current electric machines rotor speed is determined; using equations (29), (31). The momentary rotor speed and the instantaneous output torque of the machine were then multiplied to yield the current motor output power. The electrical input power demand from the energy storage system for the motor drive system is finally determined by utilizing the combined motor-inverter efficiency similarly to equation (37).

Analogous to propulsion, the regenerative braking command was utilized for braking scenarios. The required regenerative braking torque together and the instantaneous rotor speed were used to calculate the current regenerative power. Finally, the regenerative power from regenerative braking is then sent to the energy storage system.

Depending on propulsion or regenerative braking, the motor model’s output power will be a positive or negative signal respectively. This model characteristic implements a bidirectional power flow between the combined motor-inverter system, the energy storage system and the gearbox system.

The motor drive system outputs are the mechanical output power to the gearbox, the electrical input power demand from the energy storage system, and the power losses according to the motor drive's combined efficiency.

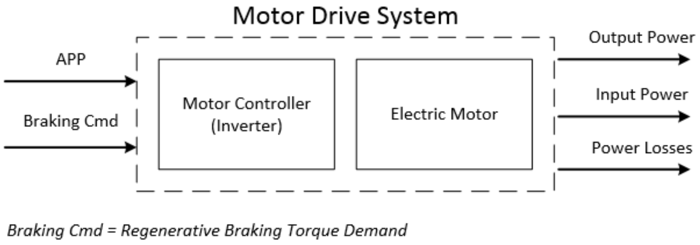

Figure 2-17 - ETS Simulation Model: Motor Drive System Inputs and Outputs

The "Energy Storage" system (ESS) is fed by the "Input Power" request of the motor drive system that was shown in Figure 2-17. Based on the power request of the motor drive and the energy storage systems efficiency, the required power need from the energy storage unit is calculated. By subtracting the required ESS power by the motor drive power request, which is also equivalent to the ESS's output power to the motor drive, the power losses are determined. The energy storage system model will then output information on the power need to supply sufficient electrical power to the motor drive system, and the ESS power loss. Also, in case of regenerative braking the model provides information on stored electrical power to allow the estimation of used electrical energy over a drive cycle when regenerative braking is applied. The Simulink model is shown in Figure 2-18.

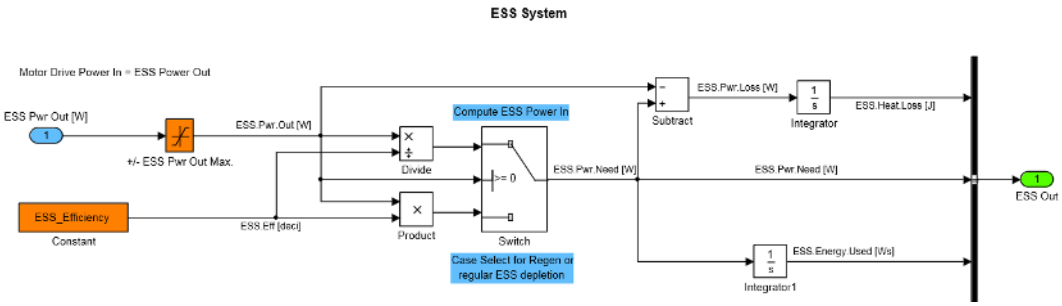

Figure 2-18 - ETS Simulation Model: Energy Storage System

The “Gearbox” system inputs the motor drive’s output power. With the current rotor angular velocity ω the model determines the current motor output torque; power is the product of torque and angular velocity. Once the momentary gearbox input torque is calculated the system applies equation (26) to determine the torque to the wheels (gearbox output torque). The gearbox system’s output torque will then interface with the next system which simulates the on-ground taxiing dynamics and the interaction of the MLG wheels with the tarmac. In a final step the defined gearbox efficiency was used to determine the instantaneous gearbox power loss.

In a last step, the gearbox system’s output torque to the wheels is put into the “Vehicle Dynamics” system, which is sometimes also called “Glider” model. With the wheel geometry of the MLG wheels as stated in Table 2-3 the actual ETS’s tractive force to the wheels is calculated. In a next step this gross tractive force is reduced by all applied motion resistances to yield the net tractive force to the road; this step implements the aircraft dynamics which were derived in equation (17). By dividing the net tractive force through the inertial mass m_i of the aircraft, see section “Aircraft Selection and Weight Estimation”, the instantaneous acceleration is obtained. Integration of the acceleration gives the current plane’s velocity which is then used as a feedback signal in the “Pilot” input system of the ETS powertrain simulation model. Some additional parameters such as gross tractive energy and the taxiing distance were calculated for post-processing purposes. The glider/ vehicle dynamics model is depicted in Figure 2-19.

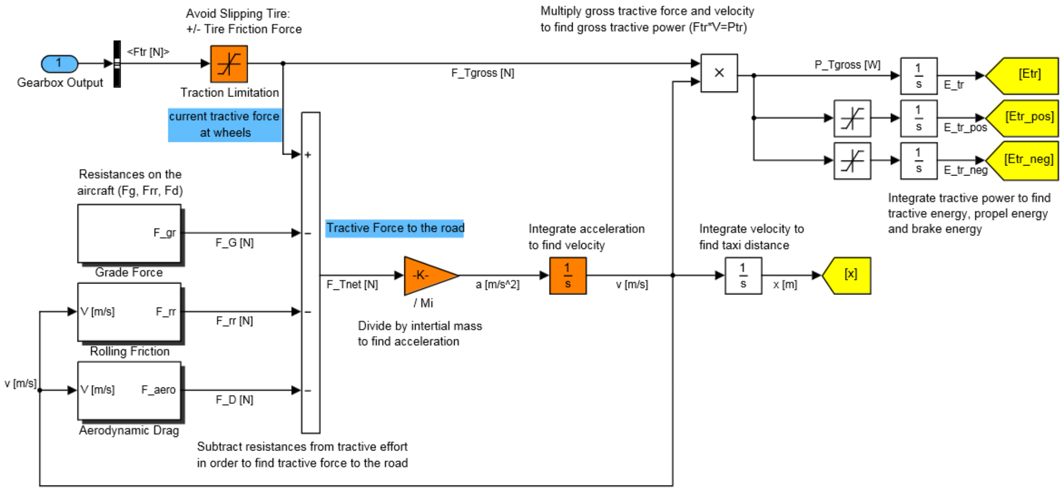

Figure 2-19 - ETS Simulation Model: Vehicle Dynamics/ Gilder System

Overall, four identical motor drive units were implemented in the ETS powertrain simulation tool, one for each MLG wheel in the aircraft's undercarriage. For every major powertrain component efficiencies were taken into account. Initially, constant efficiencies had been assumed since component specific efficiency maps were not available at the time where the powertrain tool was developed. The component efficiencies were selected to represent average state-of-the-art component specific efficiencies. However, the powertrain model can be upgraded with actual component efficiency distribution maps, such as electric motor, energy storage system and inverter efficiency maps. These efficiency maps would be capable to generate more accurate and realistic simulation outcomes for the proposed ETS.

The constant component efficiencies that were used for the initial ETS powertrain sizing and the ETS powertrain simulations across all available drive cycles were listed in Table 2-15.

Since this thesis puts an emphasis on the energy consumption of the proposed ETS powertrain, all simulations were conducted on perfectly flat ground without any grade. Hence, the effect of grade resistances while taxiing has not been investigated. Because of the fact that the drive cycle data sets did not include data on the actual elevation while taxiing, accurate outcomes on the energy consumption of such an ETS could not be determined.

2.5.2 Simulation Analysis and Results

To confirm the proposed ETS powertrain, the simulation results for the most demanding drive cycles will be shown in this section. Even though, the ETS was simulated across all driving profiles only the results for the most demanding simulation are presented. Once it is demonstrated that the proposed ETS is able to follow the trajectories of the most demanding drive cycles, it can be concluded that the system is capable of achieving the performance of less challenging driving profiles.

Using the findings from the previous drive cycle analysis (Table 2-5) for the most demanding driving profiles, required to test the ETS across the Hamilton 1 Takeoff, Frankfurt 1 Takeoff and Munich 1 Landing drive cycles. It was found that these three driving cycles impose the most challenging taxi performances in terms of maximum on-ground acceleration, peak tractive force to the road, peak power output to the road, and finally taxi top speed. If the ETS can demonstrate a satisfying performance across these driving profiles the system level feasibility of the sized ETS is shown.

The selected three drive cycles are characterized by high top taxi velocities, above the ETS performance requirements, high accelerations at high taxi speeds which demand the highest tractive forces and tractive power levels to the road among all available drive cycles. Since the sized powertrain was not designed to supply the required performance of every single driving cycle but the performance of 85 % of all available driving profiles, an ideal match when testing the ETS versus the most challenging cycles cannot be expected. Figure 2-20 to Figure 2-22 picture the drive cycle matches of the proposed system compared to the two takeoff and the landing taxi driving profiles.

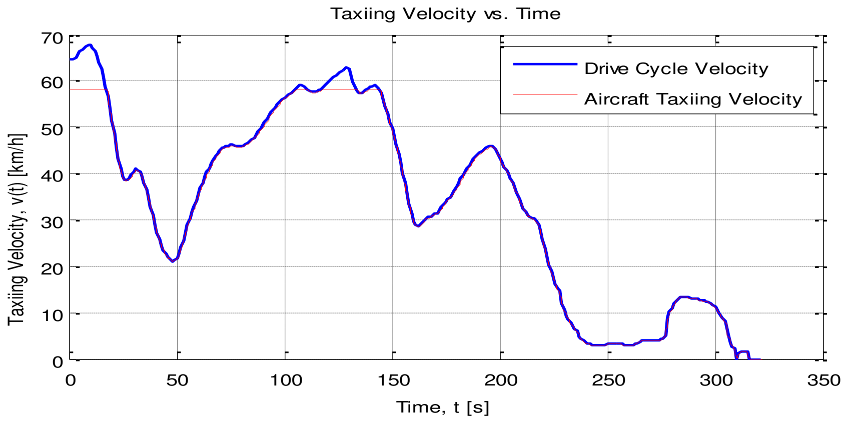

Figure 2-20 – ETS Simulation Results: Munich Landing 1 Drive Cycle Match

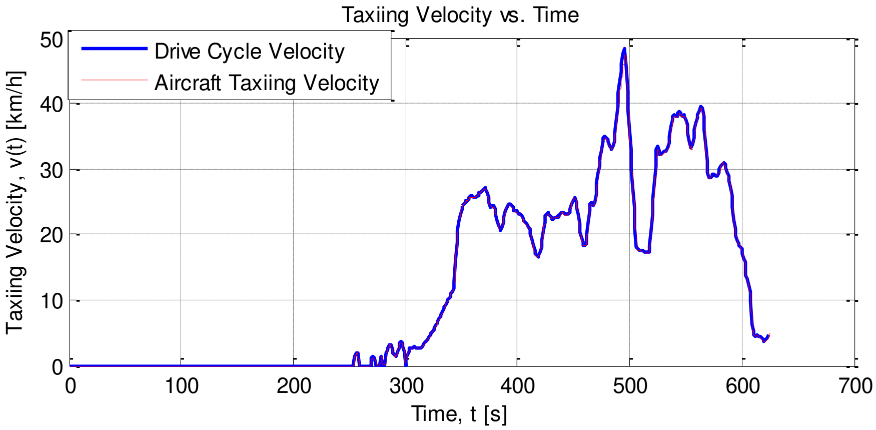

Figure 2-21 - ETS Simulation Results: Frankfurt Takeoff 1 Drive Cycle Match

On the Munich landing cycle (Figure 2-20) the ETS's top speed limitation of 58 km/h becomes apparent. The ETS is unable to reach the top speed of the conventional taxi procedure since the taxiing system was not designed for taxi speeds above 58 km/h. Hence, the ETS taxis with lower top speeds than conventional taxiing in the time intervals from 0 s-20 s and from 100 s- 150 s.

Apart from the top speed limitation on the Munich driving profile, it was found that the newly designed powertrain is still capable to perform unexpectedly well on all three driving profiles that are beyond the ETS performance ratings (seen in Table 2-15).

Due to the accurate drive cycle tracking of the ETS system across all three driving profiles, it can be concluded that the proposed electric taxi powertrain is capable to accomplish a similar driving performance as conventional taxiing for the majority of all available drive cycles.

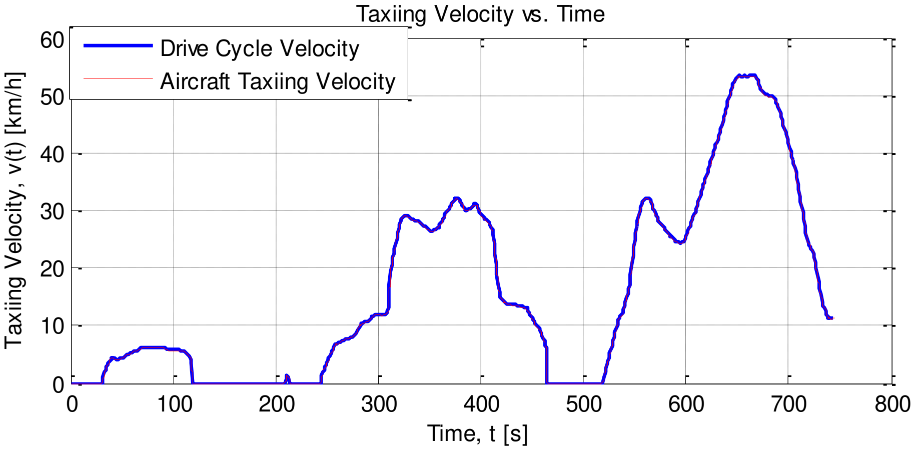

Figure 2-22 - ETS Simulation Results: Hamilton Takeoff 1 Drive Cycle Match

Even more, the proposed ETS can replace conventional taxiing for all taxi operations on airports with similar performance requirements as the ones that were derived in this study while offering the benefit of more efficient electrified ground propulsion when compared to traditional taxiing. Additionally, an ETS can make use of power regeneration functionalities due to regenerative braking which will further improve the on-ground energy consumption.

Because of the fact that this studies scope was the examination of the complete power system's performance, and more detailed, the analysis of the taxiing energy consumption with respect to energy recuperation capabilities, the consumed energy of the complete ETS across the three above mentioned drive cycles is depicted in Figure 2-23, Figure 2-24 and Figure 2-25.

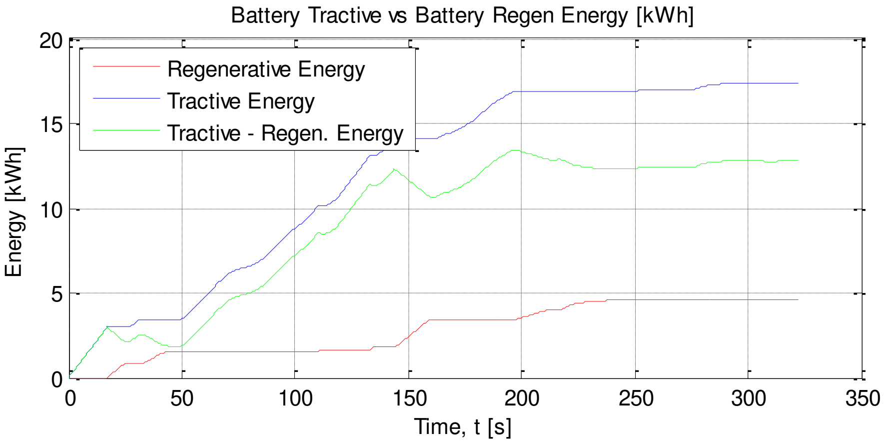

Figure 2-23 - ETS Simulation Results: Munich Landing 1 Energy Consumption

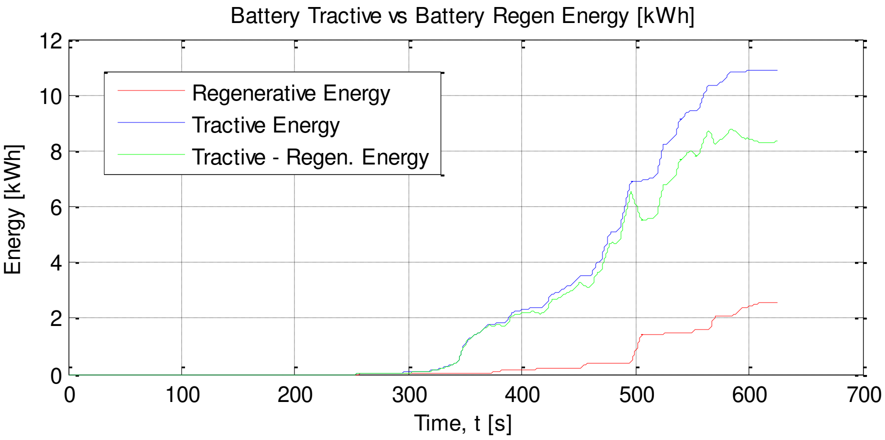

Figure 2-24 - ETS Simulation Results: Frankfurt Takeoff 1 Energy Consumption

Even though the powertrain simulation tool was primarily designed to provide ETS top level information such as average power and energy consumption across a chosen taxiing driving profile, it can also output very detailed component specific simulation results which can help in the actual component design phase. Some important simulation outcomes that the tool is capable to provide are:

- Component instantaneous power output/ input over taxi time,
- For traction motors: mechanical output torque versus rotor speed,
- Powertrain braking force or torque over taxi time,
- And instantaneous aircraft acceleration/ deceleration versus time to name only a few possible simulation results.

From the pool of possible ETS simulation results the following five parameters were selected for examining the ETS's energy consumption and performance capabilities:

<u>Total energy use</u> of the ETS which is the result of the total tractive energy minus the energy that was saved in the energy storage system due to regenerative braking in [kWh],

<u>Recovered energy</u> of the ETS due to regenerative braking in [kWh],

<u>Energy recovery</u> as the ratio of the recuperated energy and the tractive energy[5] for the selected taxi drive cycle in [%],

<u>RBF or: "Regenerative Braking Fraction"</u> This parameter is used as a measure to indicate how much braking within a selected drive cycle can be accomplished by regenerative braking to follow the target drive cycle profile. A RBF of 100 % indicates that all braking events in a particular taxi drive cycle can be performed by electric machine regenerative braking. Correspondingly, a RBF of 0 % indicates that all braking in a certain drive cycle must be done by friction brakes. The RBF is given in [%]

---

[5] Tractive Energy is equivalent to the electrical energy use when taxiing purely electric and not using energy regeneration capabilities

Average System Power describes the mean value of the instantaneous ETS system power for the purpose of following the drive cycle trajectory of the chosen taxi driving profile. This parameter is given in [kW].

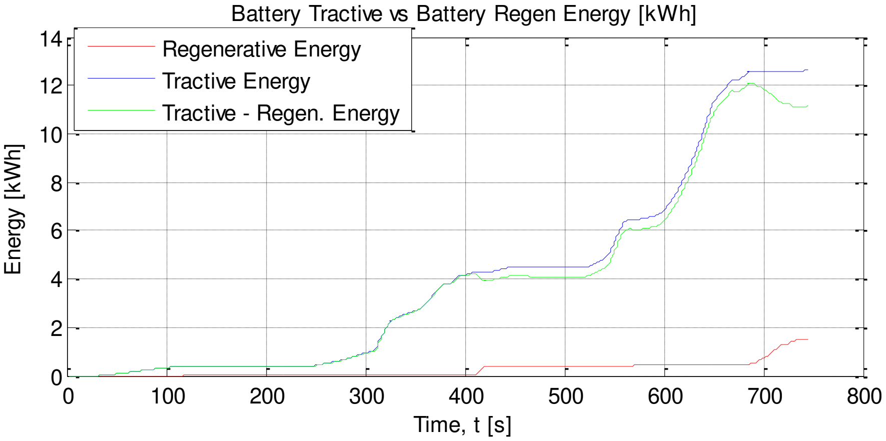

Figure 2-25 - ETS Simulation Results: Hamilton Takeoff 1 Energy Consumption

The simulation results of the Airbus A321 with the proposed ETS for the three most demanding drive cycles as well as the average results for all takeoff, all landing, and of all drive cycles in total are presented in Table 2-16.

The simulation outcomes display that in almost all braking events, across all available drive cycles, regenerative braking satisfies the conventional taxiing braking performance demands; almost 94 % of all braking throughout all drive cycles can be accomplished by regenerative braking. This offers great potential for energy savings and allows downsizing the electrical energy storage system to further reduce the additional mass of the ETS. Furthermore, by using regenerative braking for a significant amount of on ground braking allows reducing the wear and the use of friction brakes on the aircraft. This will ultimately have a positive effect on friction brake maintenance intervals and can yield cost reductions.

With the assumed grade of 0 %, it was also found that the use of regenerative braking can recover more than 14 % of the total tractive energy that is required to taxi the Airbus A321 across all given drive cycles. On some particular driving cycles such as the Munich Landing 1 cycle more than 25 % of the used energy to propel the aircraft on ground can be recovered. This further exemplifies the benefit of using modern electrified taxiing systems.

Table 2-16 – Simulation Results for Airbus A321 ETS at 0 % grade

Drive Cycle	**Energy Used [kWh]**	**Recovered Energy [kWh]**	**Energy Recovery [%]**	**RBF [%]**	**Average System Power [kW]**
Munich L 1	12.77	4.63	26.6	51.3	142.8
Frankfurt TO 1	8.33	2.58	23.6	87.8	48
Hamilton TO 1	11.15	1.49	11.8	99.3	53.9
Average of Takeoff Cycles	10.09	1.55	13	95.8	42
Average of Landing Cycles	6.93	2.5	26.7	73.6	89.6
Average of all Drive Cycles	9.79	1.64	14.3	93.6	46.5

In terms of required electric energy it was found that on average almost 10 kWh of energy storage capacity would be required. However, one particular driving profile was found (Toronto Takeoff 2) that required twice as much energy storage capacity; 20.3 kWh. This cycle was recorded during a snow storm in Canada which required the aircraft to taxi for roughly one hour on ground before takeoff. Although these taxi operations are unusual, such unforeseeable environmental impacts on the complete taxi operation must be considered when an actual ETS is designed and build. One option could be the implementation of an emergency mode of the taxiing system's controller which would switch to conventional taxiing once the energy storage system gets close to being depleted.

When the average ETS power is analyzed it can be seen that only 46.5 kW of average power were required to match conventional taxiing. Comparing this average system power with the system's motor peak power of four times 130 kW, it becomes apparent that the electric machines will operate most of the taxi time far below their peak power levels.

Overall, the trend was found that takeoff driving cycles require more energy (10.09 kWh) than landing driving cycles (6.93 kWh) to taxi electric. The reason for this is that most landing cycles are significantly shorter than takeoff driving profiles when the taxi durations are compared. Furthermore, many landing drive cycles demonstrated a smoother drive cycle profile with fewer stop and go maneuvers. Since landing cycles often make use of the fact that the aircraft is already in motion when it exits the touchdown runway, it is further explainable that a higher amount of energy regeneration can be achieved. This statement can be justified by the fact that the aircraft does not need to accelerate initially to reach a certain taxi speed and by the above mentioned arguments of demonstrating shorter and smoother taxi profiles with fewer stop and go scenarios as it is illustrated by the Berlin Landing 2 cycle in Figure 2-26.

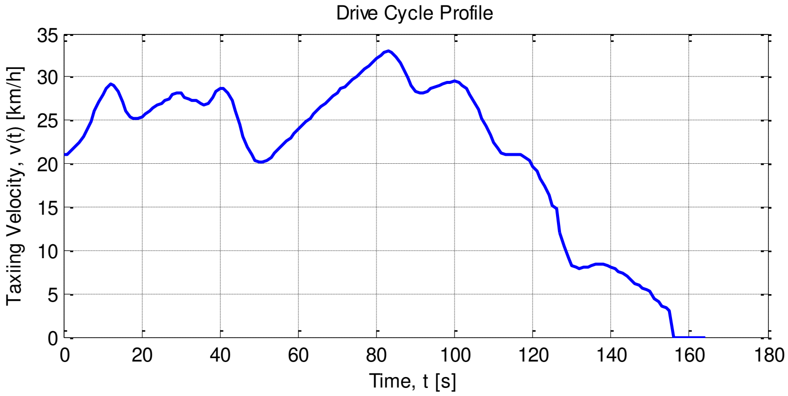

Figure 2-26 - Berlin Landing 2 Drive Cycle

3 ELECTRIC TAXI POWER SYSTEM MODEL DEVELOPMENT

This chapter covers the power system development for the ETS that was introduced, sized, simulated and analyzed in the previous chapter. Since the objective of this thesis is to investigate the proposed Electric Taxiing System in terms of its power management, efforts were undertaken to further predict the behavior of the electric traction drive system (ETDS). More precisely, the motor drive system, which is composed of an electric machine and its respective motor controller, were modeled with the ultimate goal of obtaining more reliable numbers on the energy consumption of the complete ETS.

This thesis focuses on the motor controller since it is the central component that manages the power flow in the ETS to achieve the needed taxi performance. According to what was already explained in the former chapter, in the ETS Simulation Model section, the motor controllers ensure that the electric machines supply the currently requested traction or regenerative braking torque. More accurately, the controllers input an accelerator or braking pedal position which is proportional to a traction or regenerative breaking torque request. On the basis of this torque command the controllers determine how much power must be taken from the energy storage system to feed the electric machines. With this electrical power, the motor controllers drive the electric machines to produce the desired mechanical output torque. A more detailed explanation of how the motor controller operates and what kind of controller topology was chosen for this project will be discussed in this chapter.

The objective of this initial motor controller design phase is the generation of an operating point specific efficiency distribution in order to input a more realistic component behavior into the ETS simulation model. In the last chapter the ETS powertrain simulations were carried out based on constant component efficiencies that tried to predict the average power conversion losses for each powertrain component. However, this is inaccurate and does not reflect a realistic powertrain behavior.

Therefore, the meaningfulness of the former ETS energy consumption results will be increased if component specific efficiency distributions are substituted for constant component efficiencies.

After a brief overview on electric power converters which belong to the field of “Power Electronics”, the required controller topology together with the selected electric machine type will be introduced. Subsequently to the topology selection the simulation based inverter model will be presented. The major contribution of this chapter is the easy to use motor controller loss model that was developed. In a final step the loss model was used to estimate the motor controller losses with the ultimate goal of computing the controller’s efficiency distribution for a variety of different electric machine operating points. An electric motor operating point commonly describes a specific combination of machine output torque and rotor speed.

With the efficiency profile of the inverter, the simulations from the former chapter will be repeated in the following chapter and the difference in the energy consumption will be assessed. The implementation of a more realistic and more accurate component’s behavior allows producing more reliable top level ETS performance predications such as the energy consumption. Furthermore, it yields more accurate component specific information that can be used to support the design and building process of the actual component, i.e. heat loss distribution, operation points, average and peak performance numbers to name only a few.

3.1 Introduction to Power Electronics

The term “Power Electronics” is used as a general description for the technology that is capable to transport and convert electrical power from one form to another [8]. Power Electronic systems which are commonly called “Power (Electronic) Converters” usually make use of electric circuits that modify the characteristics of electric power which are defined as the product of current and voltage [67], [68], [69]. A general power flow schematic of a power converter is illustrated in Figure 3-1.

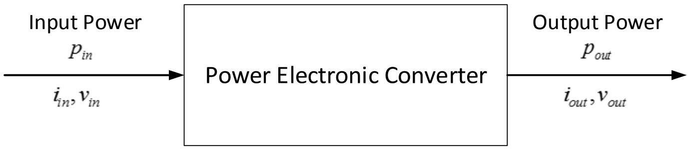

Figure 3-1 – Electric Power Conversion Schematic

Today, the most popular used devices to convert the input power to a desired output power form are semiconductors. In order to change the input current’s and voltage’s frequency and/ or their magnitude to a desired output current and voltage form, switching devices are used [68], [69].

The design process of power converters is interdisciplinary and requires electrical, magnetic, electrochemical, controls and software-based, as well as mechanical related knowledge [67], [68].

Many different power converter topologies exist depending on the power level that needs to be converted and the shape of the desired output current and voltage profiles. Most users today are not even aware of the fact that they use power electronic systems to satisfy their needs. One example is a cell phone charger which converts the grid power available from a receptacle (AC power) to a voltage and current shape that can be stored in the phones battery (DC power).

The four main power electronic converter topologies are described in Figure 3-2.

A detailed explanation on all different topologies can be found in [67] and [68]. In the following the so called "Inverter" will be described in more detail since this topology was selected to drive the electric machines in the proposed ETS.

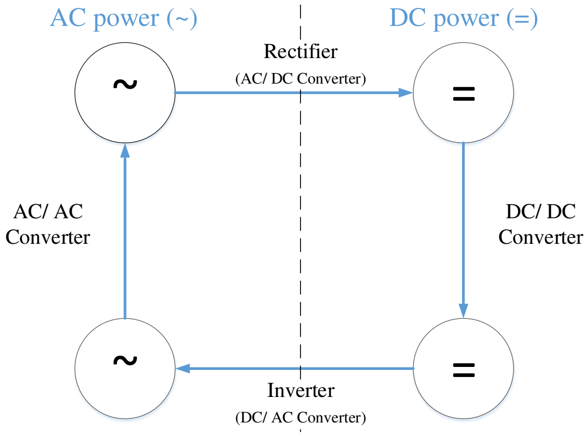

Figure 3-2 - Power Electronic Converter Types and Power Conversion Diagram

The Inverter:

An inverter is an electronic power converter that converters the available power of a DC source to a requested AC power level on its output side.

It must be mentioned that unlike often assumed no power converter is capable to actually increase the input power level. The magnitude of the voltage and the current on every converter's output might be different than it was on the input side but the product of current and voltage at the output cannot be greater than the input power. In many cases either the input voltage or current will be increased due to the converter but that means that the corresponding other factor (current or voltage) will be decreased accordingly.

Inverters are popular converters for electrical energy transportation where for instance DC power from an energy storage medium should be feed into a power grid, for uninterruptable power supplies, or they are used in certain motor drive applications in the transportation sector [67], [68].

Switching Devices:

As mentioned previously, semiconductor switching devices are used today in order to convert electrical power. The main function of such switches is to open and close an electrical circuit. A closed switch will be able to conduct current while an open switch interrupts or blocks the current's conduction. When an ideal switch is in "conduction mode" which is commonly called the "on state" the voltage across the two switches terminals is zero while the absolute value of the conducting current in greater than zero. In "blocking mode" or "off state" the former described condition turns around and the current through the switch becomes zero while the absolute value of the voltage across the two terminals of the switch becomes greater than zero. In this example, the absolute values for currents and voltages were used to avoid differentiating between the two different possible orientations (positive and negative).

The operational limits of a switch are called ratings. Depending on the switch topology and its technology, different limitations for the maximum allowable voltage across the two switch terminals (voltage rating) and the maximum allowable operating conduction current (current rating) apply. Therefore, the switch selection for a desired power converter is crucial to its proper and effective operation. The wrong selection of a switching device can yield from inefficient power conversion, high losses while converting power, in the best case to irreversible damage of the complete power converter in the worst case [67].

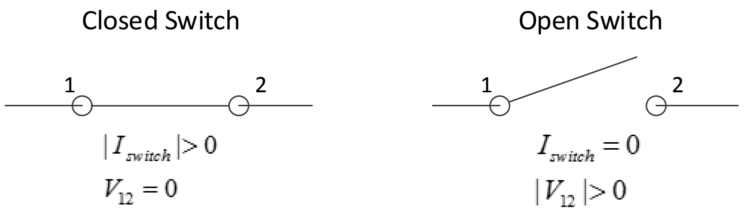

Figure 3-3 - Switching States of an Ideal Switch

Power converters that use proper semiconductor switching devices are generally characterized by low power losses that emerge from the switching device's operation itself. Nonetheless, switching device technologies are a continuous field of improvement where the following characteristics are object of improvements: size, mass, voltage and current ratings within certain switch topologies, and efficiency to name only the most important characteristics.

Switches can be classified based on different features. Mostly switches are grouped based on their used switch, and therefore semiconductor, topology. Other grouping criteria could be the operating power level, the characteristic of being an active (controllable) or passive (uncontrollable) switching device, or the measure of how fast a switch can switch between its on and off state; also called "switching frequency".

Controllable switches are semiconductor switching devices where the turn on and the turn off events can be controlled by an external signal which is commonly a small voltage that is sent to the respective switch. Analogous, passive switches are devices where the turn on/ off event cannot be controlled. Instead, the turn on/ off event is dependent on a fixed condition. The diode as an example par excellence for popular passive switching devices will switch to conduction mode if the voltage across the device (V_{12} in Figure 3-3) is greater than zero. In the event that V_{12} is smaller than zero it will block any further current flow and transitions to the off state.

A classification of the most widely used controllable switches according to their component top level performance parameters, power rating and switching frequency, similarly to what was presented in [67] is shown with slight modifications in Figure 3-4.

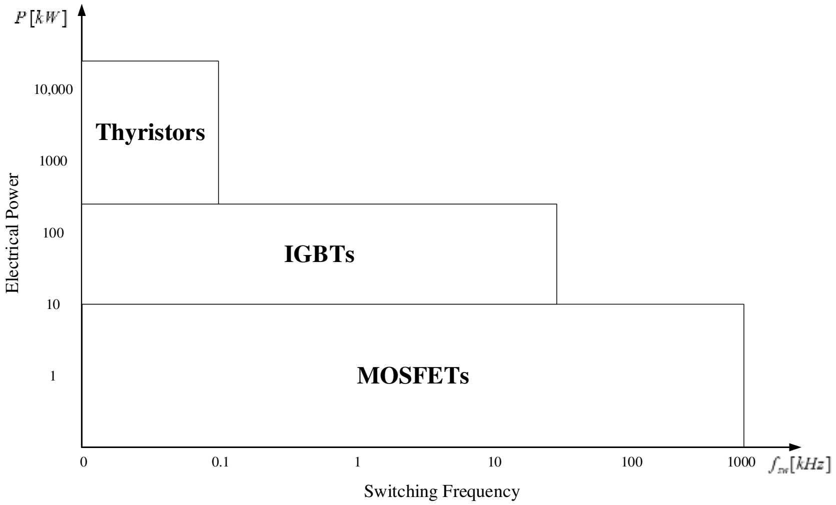

Figure 3-4 - Classification of Controllable Semiconductor Switching Devices

Diodes, which are also widely used in power electronic converters, are not explicitly shown in the classification chart above since they are uncontrollable switching devices. The operating range of modern diodes according to the information provided in [70] has been summarized in Table 3-1. Further literature and more detailed descriptions on switch topologies, their respective operational principles and characteristics can be found in [67], [68], and [70] for example.

Table 3-1 - Diodes Top Level Specifications: Operating Range

Diode Specification	Operating Range
Electrical Power P	> 0.1 kW – 10,000 kW
Switching Frequency f_{sw}	10 Hz - > 10 kHz

3.1.1 Motor Controller Topology Selection

Before the motor controller topology will be selected, two important technical terms must be introduced. These two terms are called “source” and “load” of an electric power converter. Their locations within a power converter system are displayed in Figure 3-5.

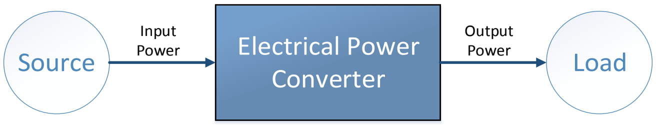

Figure 3-5 - Power Converter Integration between Source and Load

As per [68] an electrical power converter “serves as an interface between the source and load”. The source will provide the input electrical power to the converter which is defined as the product of the input’s instantaneous current i_{in} and voltage v_{in}. The converter will then convert this input power to the form that is requested by the load (v_{out}, i_{out}).

Thus, in order to select a suitable power converter topology it is important to quantify the ETS’s source and load.

Based on the proposed ETS powertrain layout, see former chapter for further explanation, the power converter’s source and load can be determined. Considering the powertrain architecture that was presented in Figure 2-14 and Figure 2-15 it becomes apparent that the electric taxi system is powered by a not further quantified electrical energy storage system. Due to the fact that this system provides the input power to the complete powertrain but more precisely to the power converter, the electrical energy storage system acts as the power converter’s source. The converter’s load is represented by the electric machine because it interfaces with the power converter on its output side.

Source:

The electrical energy storage system embodies the source. Since modern energy storage systems such as batteries, ultracapacitors, fuel cells or equivalent all provide DC power outputs, the power converter's input signal will be DC as well.

Load:

Most electric machines that are used for modern traction applications in the transportation sector are three phase AC powered [67]. When the derived single motor performance specifications from Table 2-14 are compared to traction motors that have similar performance levels (Table 2-12 and Table 2-13) it became obvious that only three phase AC machines can deliver the desired performance. Therefore the converter must be capable to supply a three phase AC power output to its corresponding traction motor.

With the quantified motor controller's source and load power characteristics, it was found that four three-phase inverters will be required to correctly manage the power flow between the energy storage system and the electric machines.

3.2 Model-based Inverter Design

Four similar three-phase inverters must operate in the Airbus A321 ETS. Since it will be assumed that these four inverters are similar to each other, the simulation-based three-phase inverter design for one representative inverter will be discussed in the following section. Initially a short overview on three phase voltage source inverters is given. Thereafter, the chosen inverter topology, a three-phase "Space Vector Pulse-Width Modulated" (SVPWM) voltage source inverter (VSI), is introduced. Finally the easy-to-use, self-derived inverter switch loss model is presented. The loss model is based on the switching device's instantaneous current and its specifications that are available in the respective device’s data sheet.

3.2.1 Introduction to Inverters for Traction Applications

In the following a voltage source inverter (VSI) was selected to explain the general operation of a three-phase inverter. The topology of a general three phase VSI is presented in Figure 3-6.

The inverter that is shown below inputs a DC source such as a battery, ultracapacitor, fuel cell or similar. This source provides the DC input power to so called “Legs”. Each leg contains two bidirectional semiconductor switching devices, or short: switches, which are labeled S1 to S6. Each individual leg’s center point interfaces then with one phase of the three-phase load to provide the desired AC phase output power. Here, the three output phases are labeled A, B, and C [67].

By opening and closing each individual switch in a certain individual sequence, the desired phase output voltage shape and frequency can be created.

It is important that the two switches within each leg will not conduct at the same time (turn on state) since such an event would cause a short circuit of the DC source [68]. Thus, the control signal which is often named “gate signal” of a certain switch in one leg must be opposed to its corresponding leg switch. As an example the control signal for switch S1 will be the opposite of the signal for switch S2. When S1 is supposed to turn on (conduction mode), switch S2 will transition to its blocking mode and vice versa. Therefore, it is sufficient to control only the states of top three switches S1, S3, S5 and apply the opposed state to the adjacent switches S2, S4, S6 in each respective leg.

Common switching devices for inverters are “Metal-Oxide-Semiconductor-Field-Effect-Transistors” (MOSFETs) or “Insulated-Gate Bipolar Transistors” (IGBTs) [67].

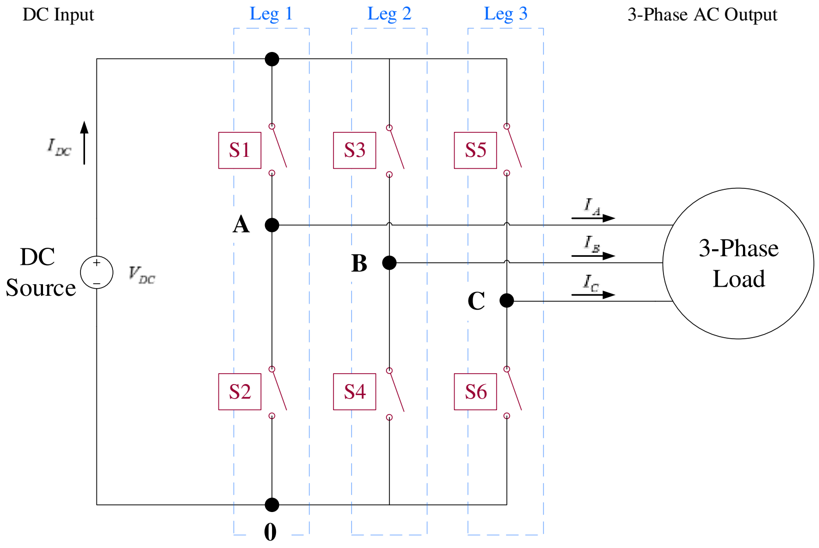

Figure 3-6 - Three Phase Voltage Source Inverter (VSI) Topology

With the opposed switch control for both adjacent switches in each inverter leg, the voltages V_{A0}, V_{B0}, V_{C0} between the inverter’s leg center points A, B, C and the connection point 0 can only equal to V_{DC} or zero.

When the electrical circuit is analyzed for each possible switching state, it can be found that the line-to-line output voltage states V_{AB}, V_{BC}, V_{CA} can only equal to either $\pm V_{DC}$ or zero [68].

The inverter’s output phase voltages V_{AN}, V_{BN}, V_{CN} to the three phase load are not simple to determine. Assuming that the switch gate signals of the top switches $S1, S3, S5$ can be either on (1) or off (0), then the possible phase (line-to-neutral) voltage output levels of a three-phase VSI, according to [71], result in:

$$\begin{Bmatrix} V_{AN} \\ V_{BN} \\ V_{CN} \end{Bmatrix} = \frac{V_{DC}}{3} \begin{bmatrix} 2 & -1 & -1 \\ -1 & 2 & -1 \\ -1 & -1 & 2 \end{bmatrix} \begin{Bmatrix} S1 \\ S3 \\ S5 \end{Bmatrix}$$

With:

$$S1, S3, S5 = \begin{cases} 1, & if\ switch\ is\ in\ its\ "on"\ state \\ 0, & if\ switch\ is\ in\ its\ "off"\ state\ . \end{cases}$$

Further information on the inverters input and output variables is available in [67], [71].

3.2.2 Motor Drive Control Strategy

A motor drive describes the overall system that is composed of an electric machine and its respective motor controller. The task of a motor controller, here the VSI as shown in Figure 3-6, is to make sure that the required three phase stator voltage is supplied to the electric machine. The control algorithm must therefore possess the property to produce different three-phase stator voltage amplitudes and frequencies[6].

The respective control strategy for a certain motor drive system, and more precisely for the motor controller, will depend on the used electric machine type. Thus, in order to control the switches of the above presented inverter correctly the electric machine's topology needs to be known.

Electric Machine Topology for Airbus A321 ETS

Parallel to the motor controller development for the proposed ETS, an electro-magnetic traction motor design for ETS applications had been conducted that targeted the demanded performance outputs listed in Table 2-14 and Table 2-15. After the desired ETS motor performance specifications were compared to two high performance benchmark electric motors, YASA 750 [64] and GKN AF-240 [65], it became apparent that only a high performance electric machine with a

---

[6] The frequency of the 3 phase voltage signal to the electric machines stator will determine the machine's rotor speed.

high power- and torque-to-mass-ratio would be capable to reach the desired powertrain performance requirements.

Because of the superior output torque demand and due to the similar motor topology that was used in both benchmarked electric machines, an Axial Flux Permanent Magnet Synchronous Machine topology, short: AFPM, was selected.

AFPMs are preferred for traction applications such as electric taxiing or high performance electric vehicle propulsion due to its pancake-like shape which allows keeping the machine compact and simple to integrate. Additionally, such machines are characterized by high obtainable power [72] which was desirable for the target application.

Presently, permanent magnet synchronous machines, short: PMSMs, are generally the preferred choice for high performance, high efficiency applications [73]. Furthermore, these machines provide high power densities as well as high torque-to-inertia ratios, and perform well under dynamic operating conditions due to their fast response [70], [73], [74].

Control Strategies for PMSMs

Any control strategy for electric machines generally describes a method to control the motor controller's switching devices in a way that a currently requested motor performance, commonly motor output torque or rotor speed, can be achieved.

In order to control modern PMSMs two control methods, the so called Vector Control (VC) and the Direct Torque Control (DTC) methods, have become widely accepted in the industry [73], [75]. In many applications vector controls are also referred to as field-oriented controls (FOCs).

Both control types can be used to control the electric machine's torque or speed. Overall both schemes ensure that the electric machine runs smoothly through its full speed range, they allow controlling the machines output torque even when it stands still, and both of them support fast machine dynamics for rapid acceleration/ deceleration operations [74]. However, VC and DTC methods have several advantages and disadvantages which are important to consider when choosing one of them for a certain application.

VCs yield smoother machine torque responses, and allow using a fixed switching frequency for controlling the inverter's switches. Furthermore, its capability to accurately control the machines stator current magnitude and angle makes it a popular choice for high performance, high accuracy motor drive applications [70]. On the other hand these controls techniques require a permanent feedback of the machine's rotor position, the control algorithm is more complex than most DTC control schemes, and VCs can only be applied for PMSMs with a sinusoidal back-electromagnetic force (EMF) [70], [75]. DTC methods on the other hand require less complex control algorithms that are independent of the machine's rotor position which in turn allows a quicker response of the machine. Drawbacks of DTC techniques are the increased inverter phase output current ripples that directly translate to greater machine output torque ripples than VCs. Additionally, DTCs cannot maintain a fixed switching frequency since their switching frequency is dependent on the machine's rotor speed, and the load torque applied to the machine [73], [75].

ETS Inverter: Motor Control Strategy Selection

The control method selection criterion for this study was the motor controller's ability to use a fixed frequency control method that ensures a smooth and high quality electric machine output torque generation. Because of this controller requirement, a vector / field-oriented control method has been chosen.

Furthermore, the so called “Space-Vector Pulse Width Modulation” (SVPWM) control method was selected to control the proposed AFPM machine for the Airbus A321 ETS.

The reasons for this control algorithm selection were the higher possible phase output voltages, higher degree of utilization of DC source voltage, and the generation of smoother inverter phase currents when compared to other techniques such as the sinusoidal pulse-width modulation (SPWM) algorithm. The implementation of SVPWM allows producing inverter output phase effective voltages and effective line-to-line voltages of up to $V_{DC}/\sqrt{6}$ and $V_{DC}/\sqrt{2}$ respectively which is $2/\sqrt{3}$ times higher than what the conventional SPWM technique can produce [71]. AC signal effective voltages or currents are commonly referred to as “rms” values.

A comprehensive description on the functionality and the implementation of SVPWM for a three-phase VSI is given in [71].

3.2.3 Inverter Design and Testing

Top Level Requirements Selection

Before the inverter model was designed, system level design requirements were compiled to ensure the desired ETS’s powertrain operation.

The first important parameter that needs to be selected is the DC input voltage of the inverter’s source. Since an ETS is targeted that is independent of the residual aircraft’s architecture in terms of power supply, the ETS’s DC source voltage level must not necessarily orient itself on electrical energy sources that already exist in the aircraft.

Recently the increase in electrification of modern airplanes to replace conventional devices, improve the aircraft power management, increase the operational efficiency, and reduce mass has led to the discussion of integrating more powerful electrical energy sources into modern aircraft. One concept to further reduce the aircraft's electrical network mass, size, and its respective losses is the implementation of a high voltage DC network with system voltage levels of 270, 350, or 540 V_{DC} [9], [76], [77]. Such DC based network could be used instead of 230 V_{AC} generators that are used in modern more electric aircraft (MEA), such as the Airbus A350 or the Boeing B737 Dreamliner, to supply electrical power on board the airplane [9]. Even though high DC bus voltages in an aircraft might be critical at high altitude and reduced pressure, due to corona discharge [78], recent studies at the University of Manchester in partnership with Rolls-Royce UTC investigate DC bus voltage levels for MEA applications at 540 V_{DC} [76], [79], [80], and [81].

The high voltage DC network approach was used as an opportunity to select the DC input voltage for all four three-phase ETS inverters. A DC source voltage of 540 $V_{DC,}$ was chosen for the Airbus A321 electric taxi powertrain due to the above mentioned reasons.

Many inverters within electrified powertrains for traction applications in the transportation sector employ switching frequencies for their switching devices from above 1 kHz [82] up to 30 kHz [83]. The most commonly used switching frequencies for modern inverters for traction motor drive applications are frequencies in the range of 5-15 kHz [82], [84], [85]. Some automotive companies such as BMW integrate power electronic converters with switching frequencies of up to 20 kHz into their electrified vehicles [86]. The majority of all inverters used in the transportation sector select either IGBTs or MOSFETs as their switching devices for electric or hybrid-electric propulsion. With respect to the switching frequency range of modern inverters for traction applications in the transportation sector, a switching frequency of 10 kHz for the proposed ETS inverters was selected.

To properly select the ETS powertrain switching devices, not only the expected inverter's switching frequency must be considered but also the desired peak power. From the findings of the ETS powertrain sizing process that was described in Chapter 2, it was determined that four three-phase inverters with a total electrical power output of above 140 kW will be needed.

Considering these two inverter system level specifications, switching frequency of 10 kHz and a power output of above 140 kW, IGBTs were selected as suitable switches for the ETS according to the switch operating classification diagram that was displayed in Figure 3-4.

Another favored, but not mandatory, inverter feature was the emission of low power losses, which equals to low heat dissipation, to keep the efficiency of the inverters as high as possible.

The top level ETS inverter specifications, which were chosen together with the AFPM motor designer, are listed in Table 3-2.

Table 3-2 - ETS Three-Phase VSI Top Level Specifications

Inverter Specification	**Value**
DC source voltage V_{DC}	540 V_{DC} (2 x 270 V_{DC})
Switching Frequency (fixed) f_{sw}	10,000 Hz (10 kHz)
Switching Devices	IGBT (Insulated Gate Bipolar Transistor)
Desired Peak Output Power P_{Iom}	approx. 140 kW
Control Algorithm	SVPWM (Vector Control)
Peak rms output phase-neutral voltage	220 V_{rms} ($V_{DC}/\sqrt{6}$)
Peak rms output line-to-line voltage	381.8 V_{rms} ($V_{DC}/\sqrt{2}$)
Expected peak rms phase output current[7]	450 A_{rms}
Inverter Heat Losses	As low as possible (high efficiency targeted)

---

[7] Specification comes from motor designer. The peak rms single phase output current is dependent on the actual load. In this study the inverter's load on the AC side is the electric machine with its stator phase resistances and inductances.

ETS Inverter Model

A virtual vector controlled voltage source inverter simulation model according to the SVPWM control method described in [71] was modeled in MATLAB/ Simulink by the use of the physical modeling library “Simscape”. More precisely the inverter was created with modeling blocks from the “SimPower Systems” library [57]. A simulation model schematic of the designed three-phase inverter is depicted in Figure 3-7.

Instead of initially connecting the three inverter’s output phases to an electric machine, as it is desired for the proposed ETS VSI, a constant load was chosen. Each phase was connected to a series resistor-inductor (RL) load which served to represent the phase resistance and inductance of each single motor phase. The constant RL loads were selected for initial validation purposes to ensure that the inverter functions as desired.

Across the RL loads, the three phase-to-neutral output voltages, short: phase voltages, V_{AN}, V_{BN}, V_{CN} were measured. The main task of every VSI is the generation of a three-phase output voltage shape that is identical to the instantaneous three-phase voltage reference signal that is put into the inverters controller; here: “SVPWM Controller” subsystem.

The inverter’s three-phase AC output voltage signal is therefore dependent on the momentary three-phase voltage reference signal. According to the magnitude and the frequency of the AC reference signal, gate signals "G" will be produced that open and close the inverter switches to generate the desired phase voltages. The two characteristics that will be controlled by the SVPWM controller subsystem are the magnitude and the frequency of the inverter’s AC phase output voltages. Commonly these switching events happen many times within a single second per switch. This generally yields to phase output voltages that do not look like the desired three-phase AC reference signal at a first glance. However, once the output phase voltages are filtered the requested three-phase output voltages can be observed.

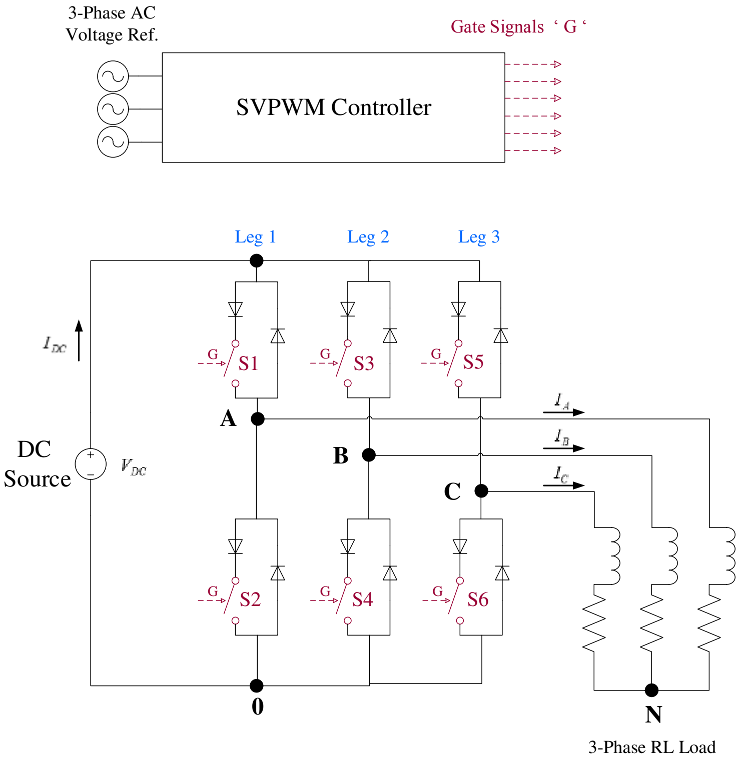

Figure 3-7 - Three Phase SVPWM Inverter: Initial Simulation Model

The gate signals in this simulation model can be either a logic one or a zero which correspond to a closed (conducting) or open (blocking) switch respectively. Depending on the momentarily demanded AC voltage reference, the number of switching events as well as the duration in which certain switches conduct or block will be determined.

Ideal IGBT Model:

Instead of using a real IGBT model that accounts for the transient switching behavior, an ideal controllable semiconductor switching device with an antiparallel diode was used to mimic the IGBTs behavior. A real IGBT is a unidirectional switching device that only allows current flow in one direction;

forward conduction mode [70]. Since a real IGBT will not conduct negative currents, an equivalent IGBT model had been used which consists of an ideal controllable switch and a diode that blocks reverse current flow through the ideal switch. Both devices are then connected in series; see left branch in the equivalent IGBT and antiparallel Diode model in Figure 3-8.

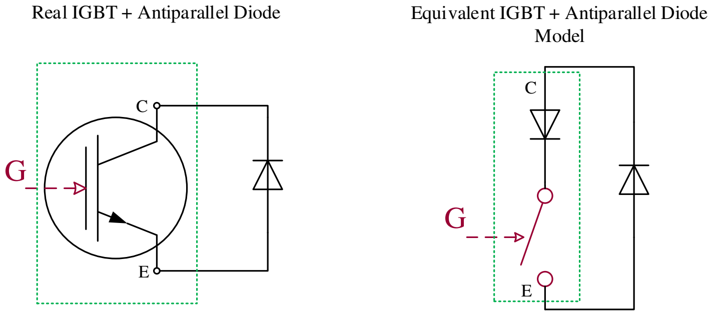

Figure 3-8 - Equivalent IGBT and Anti-Parallel Diode Model

In the schematic above G stands for the gate of the respective switching device which allows opening or closing the switch as it was discussed previously. The current flowing from the collector node C to the emitter node E is the so called forward flowing current and reverse flowing current will run from terminal E to terminal C. The current's forward conduction path for a turned on switch will be the left branch of the equivalent switch model; through the series connection path of the diode and the controllable ideal switch. Accordingly, reverse conduction will only go through the anti-parallel diode in the right branch of the model.

Idealized DC Source Side:

The DC source side of actual inverters might include more elements than what was displayed in Figure 3-7. In this simulation model an ideal voltage source was used to feed the inverter with the desired DC input voltage of 540 V. Depending on the DC source type that interfaces with the inverter's DC lines, a capacitor that is connected in parallel with the DC voltage source might be used to protect the DC source from voltage ripples. These voltage ripples can occur during the inverters operation and not every voltage source is capable to sustain quick dynamic voltage level changes. Therefore many applications that are powered by electrical energy storage devices, such as batteries or equivalent, utilize so called "DC link capacitors" in front of the true DC source. Moreover, additional filter elements are also frequently used on the DC source side to protect the DC source from current ripples. These ripples are dynamically changing currents which originate from the rapid switching events that the inverter's switches undergo during operation of the power converter. An example on the DC side current ripples with a reference to the inverters phase output currents, for an inverter with a not further characterized load, are exhibited in Figure 3-9.

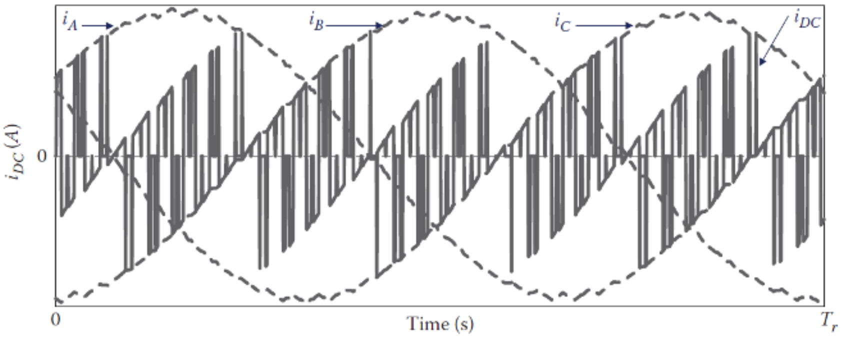

Figure 3-9 - Three-Phase VSI: DC Side and Phase Output Currents [67]

The current filter on the DC source side could be a series RL branch that is capable to keep high frequency currents away from the DC source side or any other element that acts as a proper low-pass filter.

Inverter Testing

Before the three-phase inverter with its six equivalent IGBT and anti-parallel diode models was used to derive a power loss model for each switch, the proper power conversion operation was tested. As it was mentioned previously, the goal of every inverter is the generation of AC phase output voltages to a load that are equivalent to the reference signal that is sent to the inverter's control system. More accurately, the output voltages of the inverter should show the exact same RMS voltage magnitudes as the reference signals as well as they should exhibit an identical frequency. Moreover, the designed model should also be capable to divide the current flow according to its direction of flow as it was discussed in the section "Ideal IGBT model"; positive/ forward currents should flow through the left switch model branch that was built of a diode and an ideal controllable switch whereas negative or reverse currents should run through the anti-parallel diode in the right switch model branch that was shown in Figure 3-8. Especially the last point of dividing the current flow properly will be of major importance for the switch loss model that will be discussed in the next section.

The results for a three-phase inverter with a 220 V_{RMS} (311 V amplitude), 50 Hz three-phase sinusoidal reference signal are displayed in Figure 3-10, Figure 3-11, and Figure 3-12. The load for this simulation was a constant RL load with a phase resistance R and phase inductance L similar to the final ETS motor specifications; $R = 6.82\ m\Omega$ and $L = 0.934\ mH$.

Results:

The test results confirm that the three-phase VSI with SVPWM control and ideal switches is capable to achieve the desired performance.

As displayed in Figure 3-10 the effective/ rms phase AC reference voltage of 220 V_{rms} can be reached by the inverter after a short transient time period (0-0.25 s). The transient behavior is caused due to the nature of using a simulation tool which solves a dynamic system equation with a variety of different initial conditions for every single device in the inverter model. In this transient phase the system works towards reaching its desired steady state in case that not all initial conditions, for every used block in the inverter model, were set properly; which is commonly the case. In this example, the system took approximately 0.25 seconds to get very close to its desired steady state operating point.

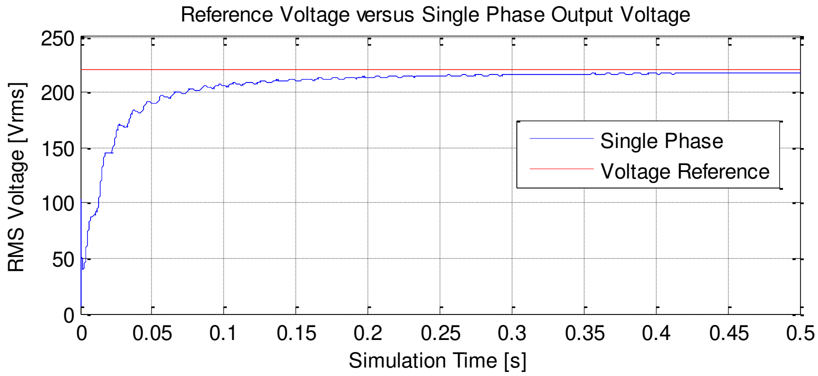

Figure 3-10 - Three-Phase VSI Testing: Phase A Output vs. Reference Voltage

Figure 3-11 demonstrates that the reference signal’s three-phase voltage frequency of 50 Hz can be generated from the inverter. This, together with the above discussed result for matching the commanded effective output rms-voltage of the reference signals, confirms that the inverter operates as desired. The observation that the amplitudes of the inverter’s phase output voltages in Figure 3-11 do not reach the amplitude of the reference signals, can be explained by considering that a filter was used to visualize the sine shaped output voltages. To confirm that the desired effective phase output voltage can be generated Figure 3-10 was provided.

Lastly, to ensure that the idealized switching devices work as intended the current split between the left and the right branch of switch model 1 (S1 in Figure 3-7) is displayed in Figure 3-12. As it can be seen in a real inverter, the positive half wave of the respective phase current passes only through the left switch model’s branch. The negative half wave, which represents reverse current flow, runs through the anti-parallel diode that is located in the right branch of the ideal switch model, respectively.

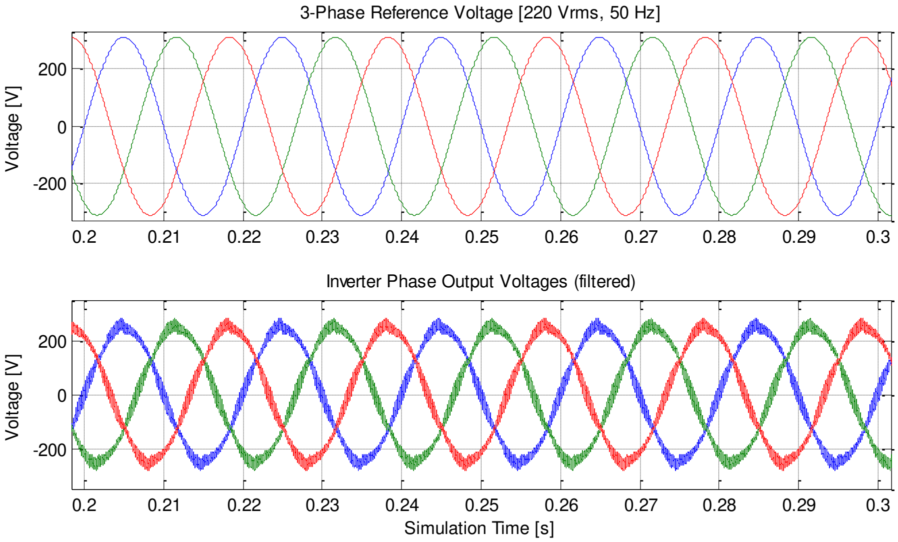

Figure 3-11 - Three-Phase VSI Testing: Filtered Phase A Output vs. Reference Voltage

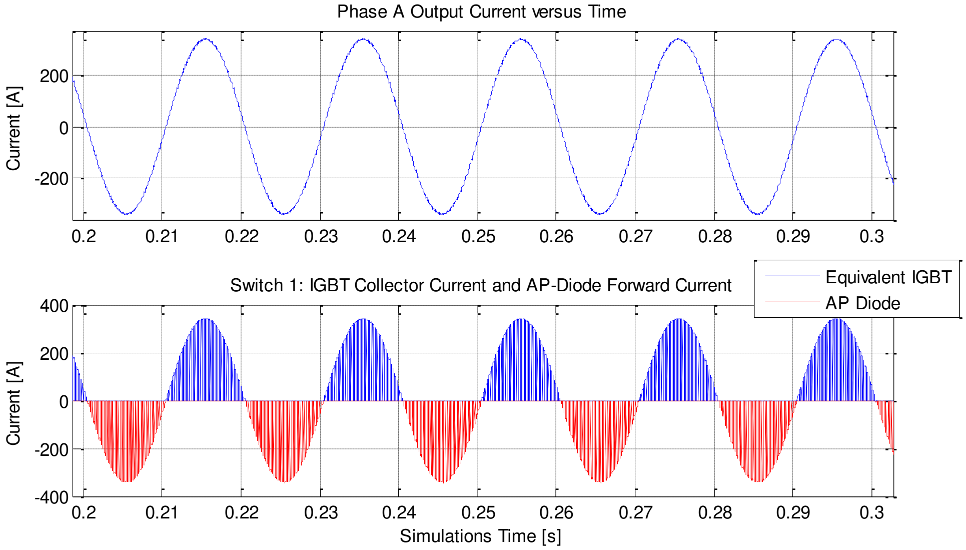

Figure 3-12 - Three-Phase VSI Testing: Switch Model Current Split

With these results the next and most important step in this ETS power system investigation study can be entered. The next section will utilize the VSI circuit model to implement a loss model that is capable to predict switching device losses.

3.2.4 Switching Device Loss Model

This section assumes that the reader is familiar with the system level operational principles of IGBTs and Diodes. Helpful information on basic operations and functionalities of these switching devices can be found in [67], [68], and [70] or any other literature resource that covers the fundamentals of semiconductor switching devices. In some particular cases switching device suppliers and their corresponding online resources can be a valuable resource as well.

Initially, before a loss model for a certain switch can be derived, a suitable switching device for the given application must be selected.

Switch (IGBT) Selection

As discussed previously and summarized in Table 3-2, an IGBT will be the most suitable switching device for the application in the ETS's inverter. The switch must be capable to sustain at least a voltage of 540 V and needs to withstand peak currents of up to 450 A_{rms} which, when a sinusoidal output current is assumed, will equal to current peaks of up to $I_p = 450\ A_{rms} \cdot \sqrt{2}$ [68]. Thus, it was determined that the chosen IGBT must be capable to tolerate 540 V and 636.4 A.

However, since voltage ripples might occur due to fast switching events of the switch, it was decided to impose a safety factor on the peak expectable voltage across the switching device's terminals. It was assumed that up to ten percent higher voltages than the DC source voltage of 540 V could occur during the switches operation, which required an IGBT with a rated voltage of almost 600 V. According to the inverter requirements from Table 3-2 and the just derived voltage and current demands, an IGBT with the following characteristics was required:

- Switching frequency: 10 kHz,
- Peak terminal voltage (also called collector-emitter voltage): up to 600 V,
- Peak current (also referred to as collector current): 636.4 A,
- And if possible low losses which in turn would yield high inverter efficiencies.

After reviewing several leading semiconductor switching device manufacturers and their products, a dual switch module from Infineon Technologies [87] has been chosen. Companies that were considered for the switch selection had been:

- Mitsubishi Electric Corporation [88],
- Semikron International GmbH [89],
- International Rectifier [90] which belongs to Infineon Technologies since January 2015,
- IXYS Corporation [91],
- And Infineon Technologies AG [87].

Infineon Technologies switches were considered due to the fact that Infineon is one of the market leaders for high power and high efficient semiconductor switching devices, because of their well-structured and easy to use product documentation, the availability of easy to implement IGBT loss calculation documentation which were helpful to get familiar with the topic of IGBT loss calculations, their product compactness even for high power switching devices, and finally since it offered a dual switch module that satisfied all requirements that were listed above.

The chosen switching device derives from the so called Infineon “Econo” product series which is characterized by superior thermal performance, convenient and simple assembly, less electromagnetic interference (EMI) emissions, and reduced turn on losses. The selected IGBT is a dual module which contains two IGBTs with their respective anti-parallel diodes in series connection, thus representing one complete leg of the inverter. The most important IGBT specifications are summarized in Table 3-3.

Table 3-3 – Infineon EconoDUAL 3 IGBT Module FF600R12ME4C Specifications

IGBT Module Parameter	EconoDUAL 3 Module: **FF600R12ME4C** [92]	Requirement for IGBT Selection
Switching Frequency f_{sw}	Up to 100 kHz [93]	10 kHz (fixed)
Peak Collector-Emitter Voltage	1200 V	600 V
Peak Current	1200 A (up to 1 ms)	636.4 A
Peak Temperature (inside switch)	Up to 150 °C (operating)	Not indicated

Further switch specifications can be obtained from the data sheet of the FF600R12ME4C switch from Infineon Technologies [92].

IGBT Module Loss Modeling

The losses of each switching device can be expressed generally as the sum of three different power losses [94]:

1. Losses based on conduction (Conduction Losses) P_c
2. Losses due to switching from the on to the off state and vice versa (Switching Losses) P_{sw}
3. Losses based on blocking (Blocking or Leakage Losses) P_b

Since the contribution of the switches blocking losses P_b on the overall power loss for a given switch is significantly smaller than the contribution of the switching P_{sw} and conduction losses P_c, the blocking losses P_b are commonly ignored when a loss evaluation is conducted [94]. Thus, the total switching device losses P_L will be approximated by:

$$P_L \approx P_{sw} + P_c \ . \tag{39}$$

Because every switch in the proposed three-phase VSI is modeled as an equivalent IGBT (series connection of diode and controllable switch) and an anti-parallel diode according to Figure 3-7 and Figure 3-8, the power losses for both, the equivalent IGBT and the anti-parallel diode, must be evaluated. Therefore the following loss models will be addressed in the subsequent paragraphs:

- IGBT conduction losses,
- IGBT switching losses (turn on and turn off losses),
- Diode conduction losses,
- And diode reverse recovery losses (turn-off losses).

All subsequent loss models will use IGBT data sheet information, the instantaneous current flowing through the respective switching device and, in some particular cases, the turn-on/ turn-off control signal (gate signal).

IGBT Conduction Losses:

If a switch is closed, which means that the device is conduction mode, the current flowing through the switch, called: collector current I_c, rises and the terminal voltage across the switch, called: collector-emitter voltage V_{ce}, decreases. While the IGBT is in its on-state the instantaneous conduction loss $P_{Ic}(t)$ can be calculated by multiplying the momentary collector current $I_c(t)$ with the current IGBT's collector-emitter voltage drop $V_{ce}(t)$. The voltage drop occurs only when the switch is in the conduction state.

$$P_{Ic}(t) = I_c(t) \cdot V_{ce}(t) \tag{40}$$

Equation (40) can also be rewritten when it will be assumed that lowercase variables stand for the instantaneous values of P_c, I_C, V_{ce}:

$$p_{ic} = i_c \cdot v_{ce} \tag{41}$$

In reality, the collector-emitter voltage drop v_{ce} depends on the collector current i_c, the gate emitter voltage v_{ge}, the instantaneous "virtual junction temperature" $T_{vj}(t)$, and the IGBT technology [70].

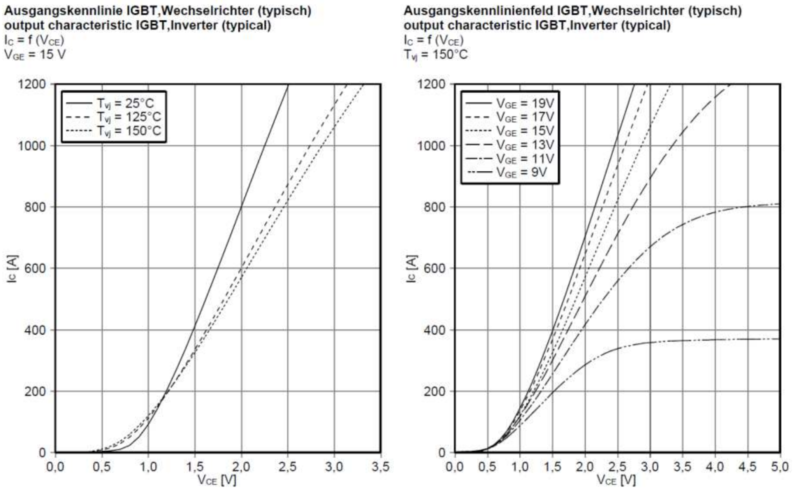

Figure 3-13 - IGBT voltage drop according to collector current [95]

The IGBT's data sheet provides details on the instantaneous voltage drop of a conducting switch for different operating temperatures T_{vj} and various gate-emitter voltages v_{ge}, displayed in Figure 3-13. By assuming these two influencing factors are constant values, it is possible to relate the switches voltage drop v_{ce} purely to different collector currents i_c. For the chosen switch a fixed temperature T_{vj}, that is equal to an IGBT's operating temperature, of 125 °C, and a fixed gate-emitter voltage V_{GE} of 15 V for turn-on and -8 V for turn-off were selected [70]. If the highest possible operating temperature for the loss calculation is selected, then the loss estimation will automatically yield conservative loss numbers. In this application, loss overestimation was preferred when compared to underestimating switching device losses.

Since the current i_c of the IGBT model can be measured at any time with use of the selected simulation software, the losses at any operating point, once the switch is in conduction mode, can be computed.

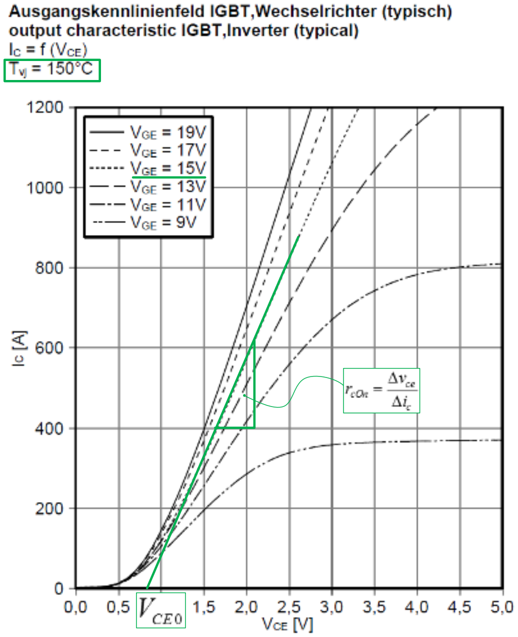

Figure 3-14 - IGBT Conduction Losses: On-State Resistance and Voltage Drop

In order to estimate the conduction losses it was assumed that the IGBT's collector-emitter voltage drop v_{ce} can be modeled as a series connection of a DC voltage source v_{ge0} and a conduction resistance r_c [94]. Such assumption is similar to a linearization of the IGBT's voltage drop behavior.

$$v_{ce} = v_{ce0} + r_c \cdot i_c \tag{42}$$

Here, v_{ge0} stands for the switches on-state voltage drop when the collector current is zero (start of conduction phase) and r_c represents the collector-emitter on-state resistance (conduction resistance).

The actual values for v_{ce0} and r_c depend on the momentary virtual junction temperature $T_{vj}(t)$ and the instantaneous gate-emitter voltage v_{ge}.

With the selected gate-emitter voltage $V_{GE} = 15\,V$ for conduction mode, r_{cOn} and v_{ce0} can be determined by using the green line in Figure 3-14.

$$v_{ce0} \approx 0.8\,V \tag{43}$$

$$r_{cOn} = \frac{\Delta\, v_{ce}}{\Delta\, i_c} \tag{44}$$

$$r_{cOn} = \frac{2.08\,V - 1.68\,V}{600\,A - 400\,A} = \frac{0.4\,V}{200\,A} = 0.002\,\Omega = 2\,m\Omega \tag{45}$$

With eq. (45), (43) and (42) in (41) the instantaneous IGBT's conduction loss p_{ic} can be computed as a function of the collector current i_c:

$$p_{ic} = i_c\,(v_{ce0} + r_{cOn} \cdot i_c)$$

$$p_{ic} = v_{ce0} \cdot i_c + r_{cOn} \cdot i_c^2$$

$$\rightarrow p_{ic} = 0.8\,V \cdot i_c + 0.002\,\Omega \cdot i_c^2 \tag{46}$$

With the use of some assumptions, such as constant maximum operating temperature, a constant gate emitter voltage during conduction mode, and linearization of the collector emitter voltage drop, the IGBT's conduction losses p_{ic} could be expressed as a function solely dependent on the switches collector current i_c.

Note: Accurate modeling of the IGBT's conduction losses is very challenging. This study focused on a simple loss estimation model, which did not intended to model the switches real operation in every detail.

IGBT Conduction Loss MATLAB Simulink Model:

The conduction loss model is designed as a circuit based simulation model and is displayed in Figure 3-15. The loss estimation according to equation (46) has been implemented in Simulink as it is shown in model below.

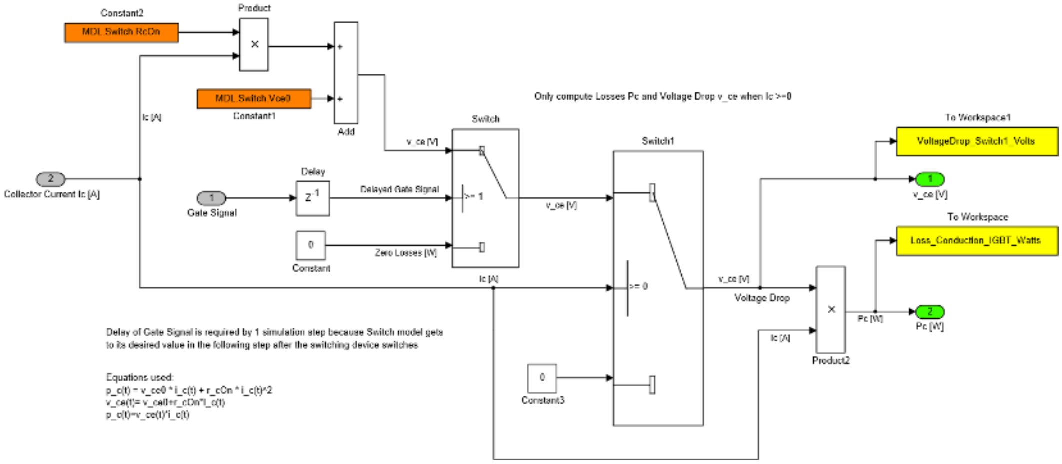

Figure 3-15 - MATLAB Simulink Model: IGBT Conduction Losses

The instantaneous collector current i_c and the switches gate signal are inputs to the conduction loss model. According to the conduction power loss equation (41), the instantaneous voltage drop and the momentary collector current are utilized to determine the conduction loss. Since the IGBT only conducts when the gate signal equals a logic one, the loss model will only evaluate conduction losses when the gate signal is greater than zero. In cases where the gate signal is zero, which indicates that the switch is in blocking mode, no conduction losses will be evaluated. The conduction loss model outputs are the switches voltage drop and the conduction loss.

The proper function of the loss model was tested by evaluating the calculated voltage drop for different collector currents. Figure 3-16 shows an example simulation of the three phase ETS inverter with the custom loss model. The simulation results demonstrate that the loss model works as desired since it produces similar voltage drop figures as the ones given in the IGBT's data sheet; for collector currents of 300 A, at virtual junction temperatures T_{vj} of 125 ˚C, the voltage drop for the chosen switch should be 1.5 V.

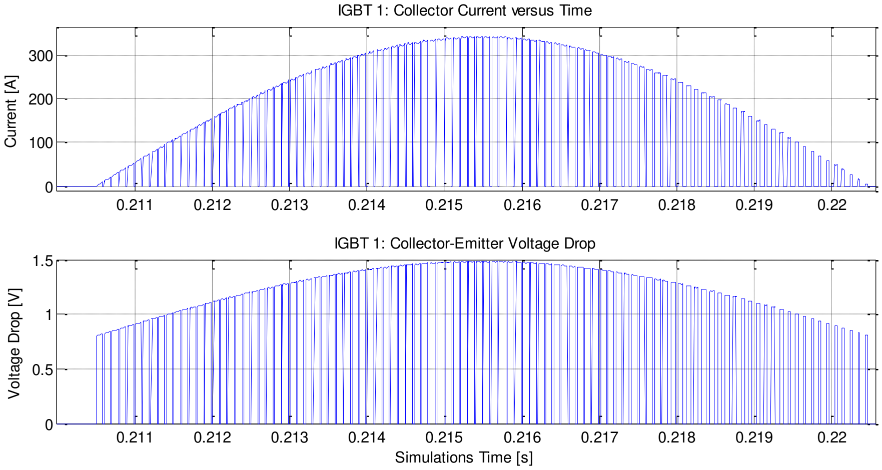

Figure 3-16 - IGBT Conduction Loss Model: Voltage Drop Characteristic

IGBT Switching Losses

Calculating the switching losses analytically is a very challenging topic. A practical method to estimate the switching losses, within an acceptable range to the actual losses, was developed based on the chosen switches data sheet [96].

The total switching losses P_{sw}, within one switching period, equal to the sum of the switches turn-on and the turn-off switching losses(P_{IswOn}, P_{IswOff}).

$$P_{Isw} = P_{IswOn} + P_{IswOff} \tag{47}$$

Since each switch commonly switches several times in one switching period, the values for P_{IswOn} and P_{IswOff} embody the sum of all occurring turn-on and turn-off switching losses per switching period. Expressing the turn-on and turn-off switching power losses in terms of the turn-on E_{IswOn} and turn-off energy losses E_{IswOff}, yields:

$$P_{Isw} = \frac{E_{IswOn} + E_{IswOff}}{t_{sw}} \quad . \tag{48}$$

Here, t_{sw} is the inverter's switching time per one switching period according to the fixed switching frequency f_{sw}. This study selected a switching frequency f_{sw} of 10 kHz.

$$t_{sw} = \frac{1}{f_{sw}} \tag{49}$$

It is important to be aware of the fact that both, the turn-on and turn-off, switching energy losses E_{IswOn}, E_{IswOff} strongly depend on the instantaneous switches collector current i_c [96]. The losses are further influenced by the present virtual junction temperature $T_{vj}(t)$ and the switches gate resistance R_G [70]. Each switch data sheet provides typical switching energy loss numbers, for turn-on and turn-off events, based on component tests that were executed by the manufacturer. This test data was used to estimate the IGBT's total switching energy loss E_{Isw}. E_{Isw} is defined as the sum of the total turn-on switching energy loss E_{IswOn} and the total turn-off switching energy loss E_{IswOff}.

$$E_{Isw} \coloneqq E_{IswOn} + E_{IswOff} \tag{50}$$

Figure 3-17 shows the used switching loss test data that was provided by Infineon Technologies [92].

Figure 3-17 reveals that the turn-on and turn-off losses are not equivalent for most operating collector currents I_C. Additionally to this observation, it must be added that some assumptions were made by the manufacturer to provide the above presented loss data:

The gate resistance R_G of the IGBT was assumed to be constant at $R_G = R_{Goff} = R_{Gon} = 0.51\,\Omega$. The collector-emitter voltage V_{ce} was kept constant at 600 volts, which equals to half the switches collector-emitter voltage rating V_{ces} of 1200 V [92]. Usually these operating conditions cannot be maintained when the switch transitions between on and off states. Furthermore, the available loss data of the IGBT is only given for virtual junction temperatures T_{vj}, that are situated at the top of the allowable temperature operating range.

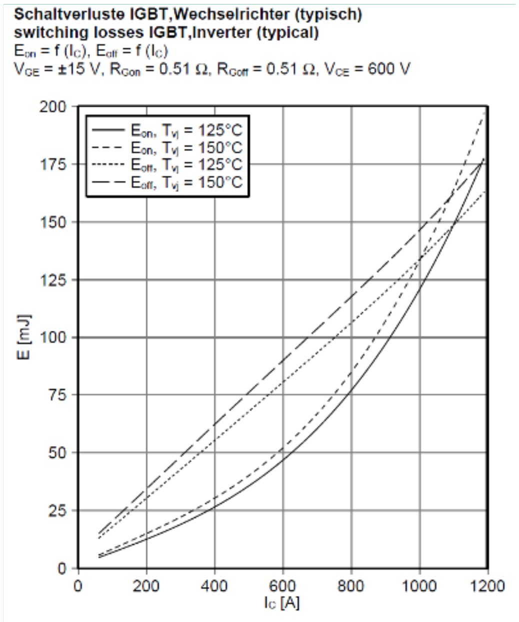

Figure 3-17 - Infineon IGBT FF600R12ME4C: Switching Energy Losses

As a result, the provided loss data presents conservative loss information under the above mentioned assumptions. For the ETS inverter's loss model, a constant IGBT junction temperature T_{vj} will be assumed, that is close to the switches peak operating temperature T_{vjm}.

$$T_{vj} = 125\,^{\circ}C$$

The switching energy losses can be approximated by assuming the energy loss is a function that only depends on the instantaneous collector current i_c. This approach is similar to the IGBT's conduction loss approximation method.

Turn-On Switching Losses E_{IswOn}*:*

Based on the strong non-linear turn-on energy loss behavior that was shown in Figure 3-17, a proper non-linear function for the dependency of E_{IswOn} on the instantaneous collector current i_c must be found. A loss linearization, as it was applied to estimate the IGBT's conduction losses in the former section, will not be sufficient to correctly estimate the turn-on energy losses.

As a consequence, the IGBT's turn-on energy loss data from the data sheet (Figure 3-17) had been digitized by the use of a plot digitizer [97]. Secondly, the points were exported to a spreadsheet application to further process and store the extracted loss data; here, Microsoft Excel was chosen. Two column vectors, one vector for the collector current and the second for the respective IGBT's turn-on energy loss, were stored in Microsoft Excel. Subsequently, these vectors were imported into MATLAB by use of the "xlsread" command [98]. Finally, both vectors were used to derive a mathematical equation that relates the instantaneous turn-on energy switching loss to its related collector current. This "curve fitting" process was done with the MATLAB "Curve Fitting Tool" application. Different polynomial order fits were investigated, until a satisfying mathematical representation for the energy loss versus collector current data set was found. The overall process, from digitizing the IGBT's energy loss data sheet information to the point where a proper polynomial turn-on energy loss function was determined, is schematically visualized in Figure 3-18.

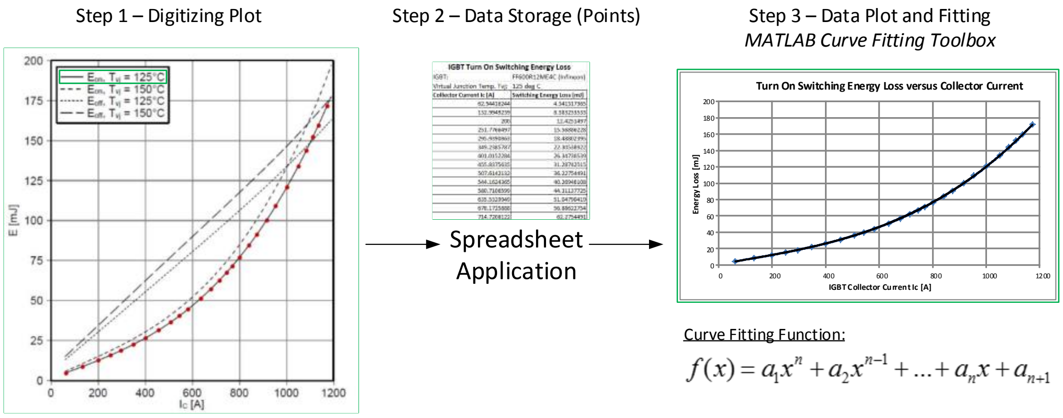

$$f(x) = a_1 x^n + a_2 x^{n-1} + \ldots + a_n x + a_{n+1}$$

Figure 3-18 - IGBT Turn-On Switching Losses: Curve Fitting Process

For the selected switch, a third order polynomial fit achieved an acceptable turn-on losses curve fit. The function, which relates the turn-on energy losses to the instantaneous collector current, is expressed in equation (51).

$$E_{IswOn}(i_c) = 7.641 \cdot 10^{-8}\, i_c^3 - 1.383 \cdot 10^{-5}\, i_c^2 + 0.057\, i_c + 0.86 \tag{51}$$

Note: The indicated turn-on switching loss in equation (51) is given in Millijoules [mJ]. Furthermore, the equation only applies for the selected switch. In case a different switch will be selected, equation (51) needs to be adjusted accordingly.

Turn-Off Switching Losses E_{IswOff}:

The turn off switching energy losses E_{IswOff} can be estimated similarly to the turn-on switching losses, which were discussed in the previous section. From Figure 3-17 it can be seen that the turn-off losses E_{IswOff} show almost an ideal linear dependency on the IGBT's collector current i_c. Therefore, the turn-off IGBT losses were modeled as a linear function based on the collector current (Figure 3-19). The turn-off energy loss graph, for a virtual junction temperature of 125 degree Celsius, from Figure 3-17 was used to derive the turn-on loss equation as a function of the collector current.

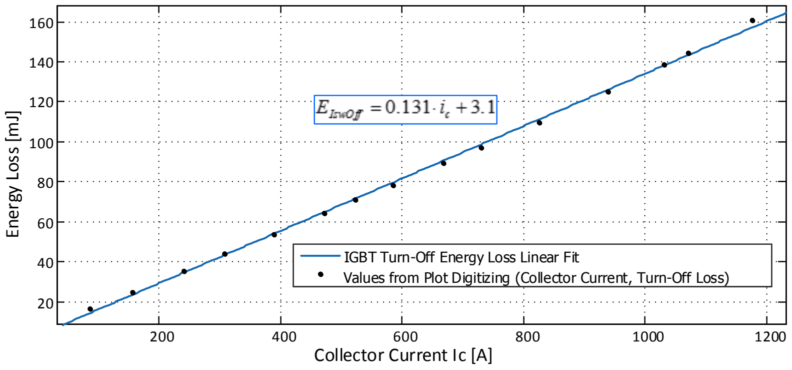

Figure 3-19 - IGBT Turn-Off Energy Loss: Linear Curve Fitting

The implemented function, relating the turn-off losses of the IGBT in Millijoules to the collector current, is presented in equation (52).

$$E_{Iswoff}(i_c) = 0.131\, i_c + 3.1 \tag{52}$$

IGBT Switching Loss (Turn-On/ Turn-Off) MATLAB Simulink Model:

In order to accurately estimate the switching and conduction losses while the inverter model is simulated across different drive cycles, it is crucial to precisely sense the events when the IGBT model gets turned-on and turned-off. Sensing these two events had been done by developing a turn-on and turn-off indicator logic in Simulink. Whenever the gate signal of a certain switch changes its state, a trigger will be sent to a respective subsystem to perform one of the following three tasks:

- Turn-on switching loss (transient) calculation,
- Turn-off switching loss (transient) calculation,
- Conduction loss computation (while IGBT is in the on-state).

The turn-on/ -off indicator logic is displayed in Figure 3-20.

The turn on detector only outputs a logic one, which signalizes a turn on event, when two conditions are met. Condition one checks if the current value of the gate signal is equivalent to one, signalizing that the switch is in conduction mode (on-state). The second condition investigates if the gate signal in the previous simulation step was equivalent to zero, which means that the switch was in the off-state before it became active. The delay block delays the gate signal by an indicated number of simulation steps to allow accessing earlier signals, i.e. for evaluation purposes. Only if both criteria are met, a turn-on event will be sensed by the turn-on detector. Similarly, the turn-off event was sensed. In this latter case, the gate signal's transition from a logic one to a logic zero was evaluated. Once such an event was detected, the turn-off detector detected a turn-off event.

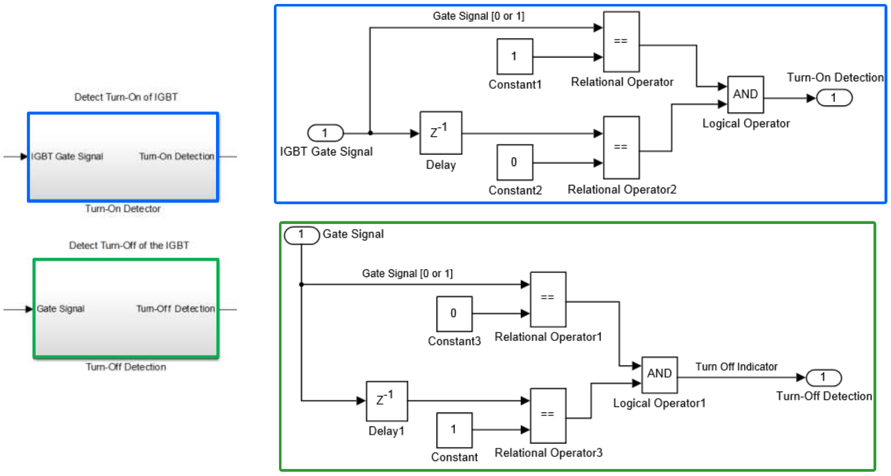

Figure 3-20 - IGBT Turn On and Turn Off Detectors

A test for one gate signal turn-on / turn-off cycle is displayed in Figure 0-1 in the Appendix of this thesis.

The switching losses were modeled by utilizing the behavior of an ideal switch in Simulink. An ideal switch will immediately reach its target conduction state once the gate signal requests a switching event; meaning that the switch does not consider any transient switching behavior. The way this was implemented in MATLAB Simulink, is explained in the following:

If a gate signal at simulation step "k" commands a switching state change from the ideal switch, the switch model will reach its target state in the following simulation step "k+1". The ideal switch will respond immediately without passing through its characteristic transient switching behavior. This model characteristic was carefully considered when the switching loss models were designed to pick the correct collector current numbers for certain switching events. The turn-on and turn-off loss models are detailed below.

Turn-On Switching Loss Model

The IGBT Simulink model was designed as an ideal switch with a diode in series (Figure 3-8). The ideal switch measures the collector current I_C of the IGBT and the switches collector-emitter voltage V_{CE} at any time. The turn-on loss model only uses the turn-on event detector signal, model shown in Figure 3-20, and the collector current i_c to evaluate the turn-on switching losses E_{IswOn}. The calculation model is embedded in a subsystem, which is shown in Figure 3-21, with the label "Turn-On Losses". The detailed structure of the IGBT's turn-on switching loss subsystem is displayed at the bottom in Figure 3-21. An example output of the loss calculation, while simulating the loss model, which is labeled "MatLab Output" is displayed in the top right corner.

It was found that the ideal switch model enters the conduction mode one simulation step after the gate signal requests a turn-on event. At simulation step "k", which in this example equals to simulation step 115, the gate signal jumps from zero to one; indicating a turn-on event. The previously introduced turn-on detector immediately detects this event at the same simulation step "k". Because of the fact that the IGBT collector current requires one simulation step to reach its demanded magnitude, the turn-on switching loss calculation is designed to delay the turn-on detector's signal by one simulation step. This allows considering the desired collector current value at simulation step "k+1", which is required to correctly calculate the turn-on loss.

In the event that the turn-on detector does not sense a turn-on request, no turn-on loss evaluation will be conducted. The realization of this evaluation logic is expressed by the first "Switch"-Block. The second switch "Switch 1" is used as a protection block and is optional. It ensures that no switching losses are evaluated in case that a negative collector current flows through the switch. Usually, an IGBT will not permit reverse current flow device, but it was found that in some particular cases very little negative currents might flow through the switch model. Thus, the second switch makes sure that a faulty switching loss determination can be avoided.

Finally, the calculated energy loss is converted to Joules by dividing the turn-on switching energy loss, which is computed in Millijoules, by 1000.

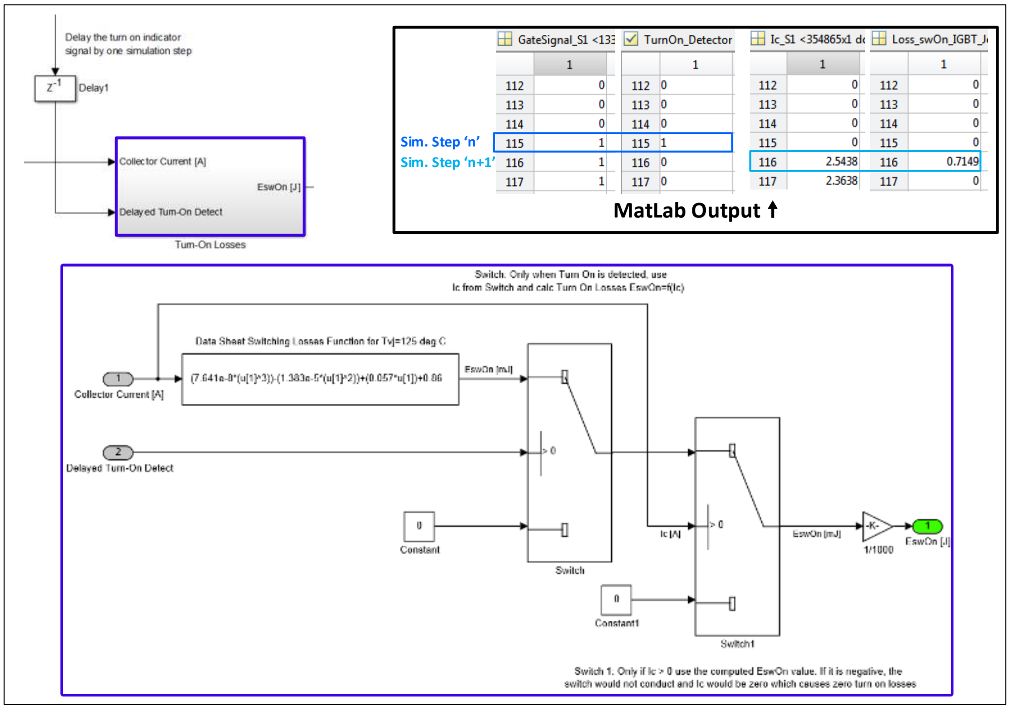

		GateSignal_S1 <133		TurnOn_Detector		Ic_S1 <354865x1 d		Loss_swOn_IGBT_J
		1		1		1		1
	112	0	112	0	112	0	112	0
	113	0	113	0	113	0	113	0
	114	0	114	0	114	0	114	0
Sim. Step ‘n’	115	1	115	1	115	0	115	0
Sim. Step ‘n+1’	116	1	116	0	116	2.5438	116	0.7149
	117	1	117	0	117	2.3638	117	0

MatLab Output ↑

Figure 3-21 - MATLAB Simulink Model: IGBT Turn-On Energy Losses

Turn-Off Switching Loss Model

The simulation model for the IGBT’s turn-off switching energy losses E_{IswOff} had been designed analogous to the aforementioned IGBT turn-on switching losses. The only difference between both models is the model property of not using a delayed turn-off detection signal input. As indicated in the MATLAB signal output in the top right corner of Figure 3-22, the turn-off detection occurs simultaneously to the last non-zero conduction current value I_C before the switch is turned off. Therefore, the turn-off switching energy loss can be calculated at the exact same time when a turn-off event is detected. The detailed model is presented in Figure 3-22.

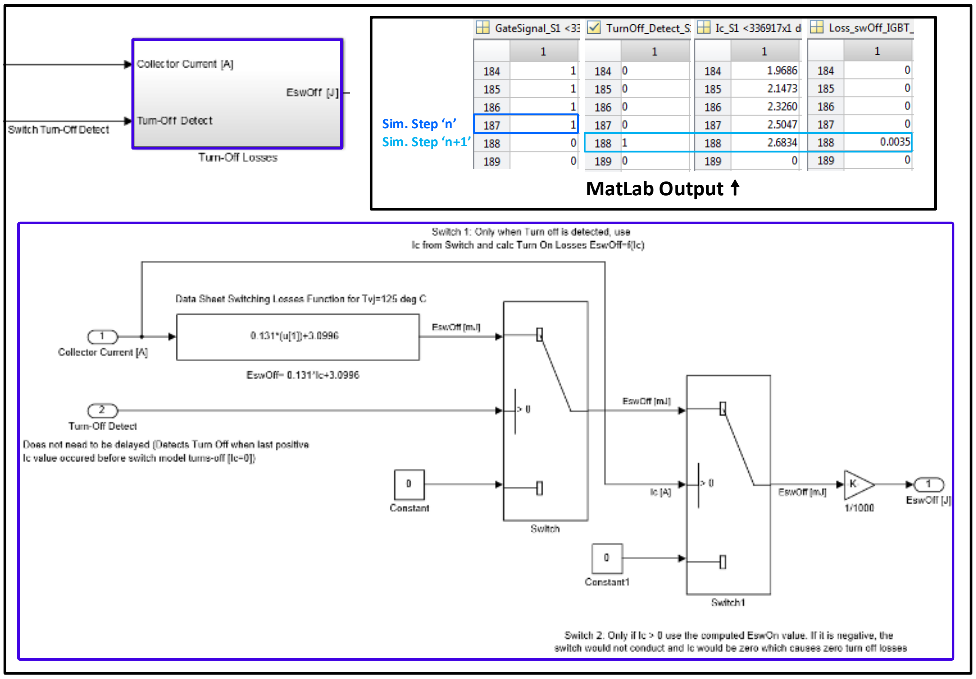

	GateSignal_S1 <33	TurnOff_Detect_S	Ic_S1 <336917x1 d	Loss_swOff_IGBT_
	1	1	1	1
184	1	0	1.9686	0
185	1	0	2.1473	0
186	1	0	2.3260	0
187	1	0	2.5047	0
188	0	1	2.6834	0.0035
189	0	0	0	0

Figure 3-22 – MATLAB Simulink Model: IGBT Turn-Off Energy Losses

Figure 3-23 displays the results of a switch loss model test. Eight different switching events are shown together with their respective switching energy losses. In this example the switches collector current i_c in conduction mode equals to roughly 340 A. The available switching loss information from the selected

Infineon switch (Figure 3-17) demands that the turn-off switching losses must greater than the turn-on losses for collector currents below 1100 A. Since the target operating range for the switch is below 700 A peak current, the switch model must always return higher turn-off than turn-on switching energy losses. When the test results below are considered it can be seen that the switch satisfies this criteria.

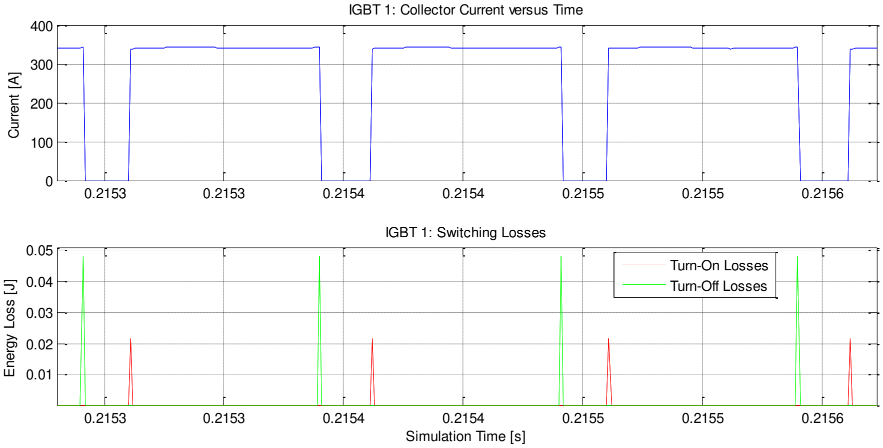

Figure 3-23 - Model Testing Results: IGBT 1 Switching Losses

From the simulation outcomes, displayed in Figure 3-23, it becomes apparent that the loss model works as desired. The magnitudes of the switching losses equal to the information that is provided by the manufacturer's loss data. This confirms the proper operation of the loss model. For collector currents of approximately 340 A, the energy loss for a turn-on event must be less than 25 mJ and below 50 mJ in case of a turn-off event.

(Anti-Parallel) Diode Conduction Losses

The anti-parallel diode's conduction losses have been modeled in the exact same way as the IGBT conduction losses, which were presented previously. The necessary data, required to estimate the conduction losses, was taken from the chosen switches data sheet [95]. Since the chosen switch module contains two IGBT and anti-parallel diode sets, the diode's performance specification are also obtainable from the IGBT module's data sheet. In other application the switch must not necessarily provide information on the anti-parallel diode. In these cases, a proper diode needs to be selected preliminary of deriving the conduction loss estimation equation. The diode's forward characteristic, which contains information on how the voltage drop is related to the diode's operating conditions, is depicted in Figure 3-24. The loss model relates the conduction losses only to the current that flows through the diode, similar to what was presented in the case of determining IGBT conduction losses. This diode's current is also called forward current I_F. The operating temperature of the diode was assumed to be constant at 125 °C.

The detailed derivation of the voltage drop function can be found in the Appendix, section Switch Loss Model. The resulting mathematical expression to estimate the diode's voltage drop is presented in eq. (53):

$$v_f = \left(1.745 \cdot 10^{-3} \frac{V}{A}\right) \cdot i_f + 0.86\, V \tag{53}$$

The instantaneous conduction power loss p_{Dc} is then obtainable by multiplying the voltage drop v_F with the instantaneous forward current i_F.

$$p_{Dc} = v_F \cdot i_F$$

$$p_{Dc} = r_{Dc} \cdot i_F^2 + V_{F0} \cdot i_F$$

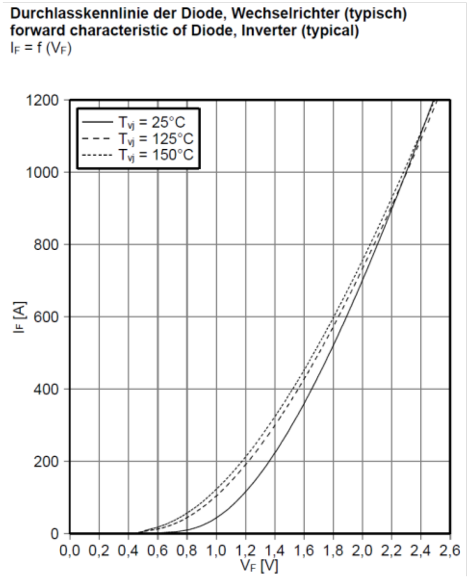

Figure 3-24 – Infineon IGBT FF600R12ME4C: Diode Forward Characteristics

For the selected switch, the diode's conduction power loss estimation resulted in:

$$p_{Dc} = \left(1.745 \cdot 10^{-3} \frac{V}{A}\right) \cdot i_F^2 + 0.86\, V \cdot i_F \ . \tag{54}$$

Lastly, it is important to note that the conduction losses only occur while the diode is in the on-state.

Diode Conduction Loss MATLAB Simulink Model

The major difference between the IGBT and diode's conduction loss model is the fact that the diode is an uncontrolled switching device, which does not operate on the basis of a logic turn-on or turn-off signal. Therefore the conduction loss evaluation will not be triggered by the instantaneous switches gate signal but by the momentary forward current i_f.

Apart from this loss evaluation trigger modification, both conduction loss models, for the IGBT and the diode, are similar to each other. The diode's conduction power loss model is displayed in Figure 3-25.

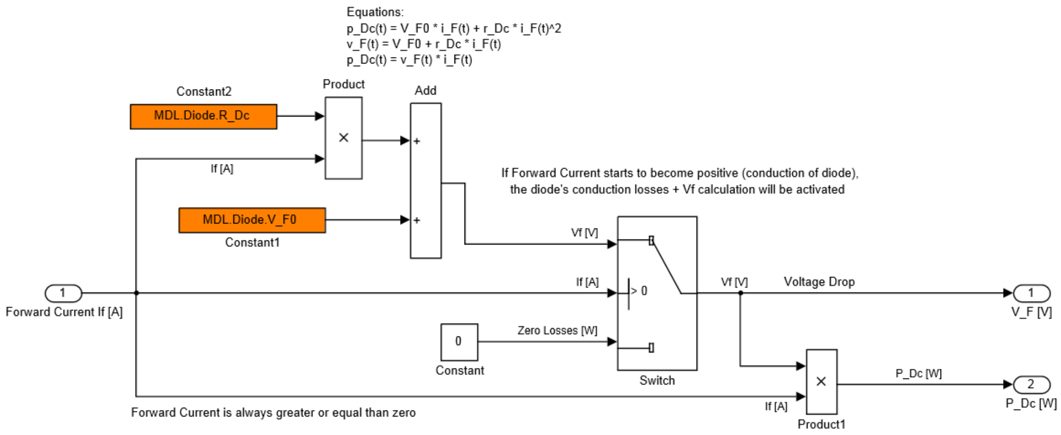

Figure 3-25 – MATLAB Simulink Model: Diode Conduction Losses

The results from a test simulation, which are presented in Figure 3-26, confirm that the conduction loss model is capable to reproduce the voltage drop numbers that are given in the switches data sheet [92]. The chosen switch features a voltage drop of almost 1.5 V for forward currents equivalent to 350 A, which was calculated from the loss model as well.

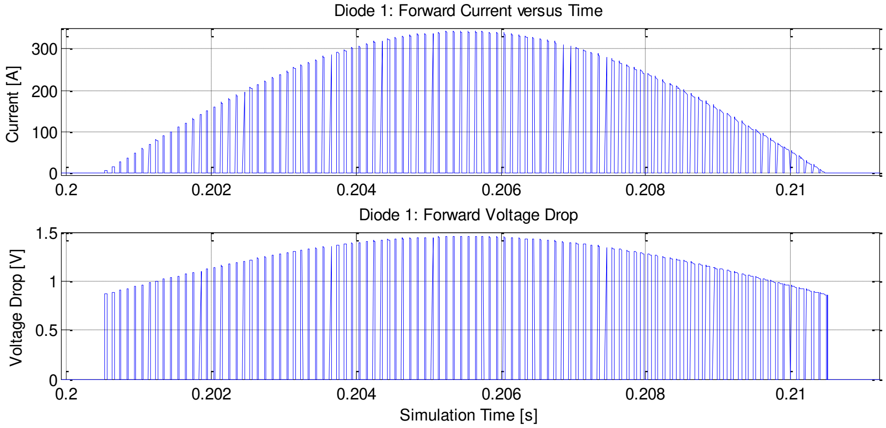

Figure 3-26 - Diode Conduction Losses: Test Results

Diode Reverse Recovery Losses (Turn-Off Losses):

The anti-parallel diode's switching loss calculation follows a similar approach as the presented IGBT switching loss estimation. Based on the given diode's energy loss behavior, indicated in the switches data sheet, a relationship between turn-off, also called reverse recovery, energy loss E_{rec} and instantaneous forward current i_f can be established. The designed switch simulation model allows sensing the forward current at any time, which makes it very convenient to compute the reverse recovery losses of the diode.

Initially it is important to mention that the diode's turn-on switching loss E_{DswOn} is negligibly compared to the turn-off loss $E_{DswOff} = E_{rec}$ [70]. This behavior differs from the IGBT's switching losses, where two different graphs for turn-on and turn-off events were presented in the data sheet. Hence, the total diode switching losses E_{Dsw} were approximated by only considering the reverse recovery losses E_{rec}.

$$E_{Dsw} \approx E_{DswOff} = E_{rec}$$

As it was done before, the loss data of the diode, while operating at a chosen virtual junction temperature T_{vj} of 125 °C, was digitized and curve fitted. The outcome of this process is a polynomial function that directly relates the instantaneous forward current i_F to corresponding reverse recovery energy losses E_{rec}. The process of digitizing the diode's loss is detailed in Figure 3-27.

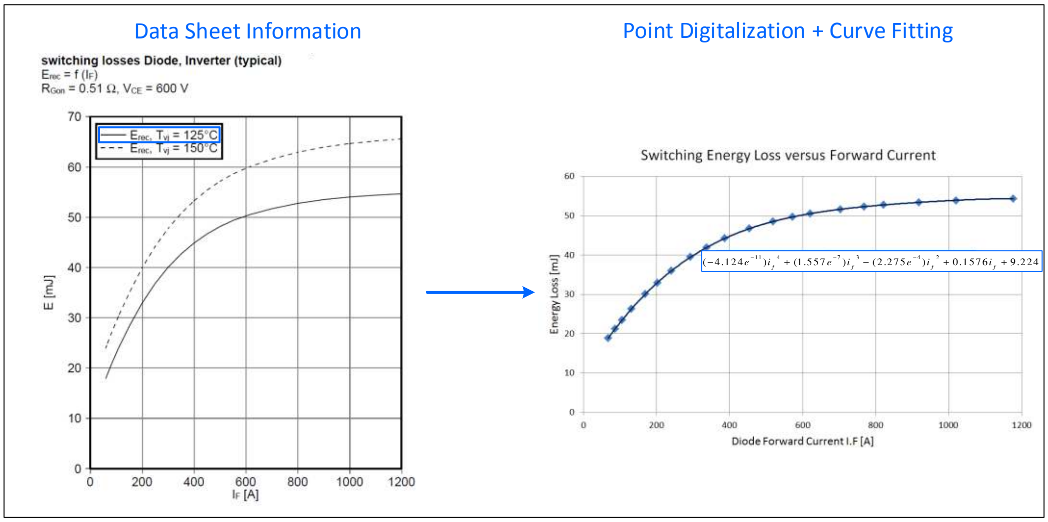

Figure 3-27 - Diode Switching Loss: Digitalization and Curve Fitting Process

In the end, a fourth-order polynomial fit led to a satisfying reverse recovery loss representation.

$$E_{rec} = (-4.124 \cdot 10^{-11}) \cdot i_F^4 + (1.557 \cdot 10^{-7}) \cdot i_F^3 - (2.275 \cdot 10^{-4}) \cdot i_F^2 + 0.1576 \cdot i_F + 9.2294 \tag{55}$$

Note, that the diode’s switching energy losses E_{rec} in equation (55) are presented in Millijoules [mJ].

Diode Reverse Recovery Loss MATLAB Simulink Model

It is important to detect the turn-off events of the diode to trigger the reverse recovery energy loss calculation. To do so, a turn-off detection subsystem has been designed that allowed proper turn-off sensing.

The overall logic behind sensing a diode’s turn-off event, which marks the end of the diode’s conduction phase, is similar to the logic that was implemented for sensing the IGBT’s switching events. The only difference in the diode’s turn-off detector system is the trigger signal. The turn-off detector inputs the instantaneous forward current i_f, whereas the IGBT's switching event detector used the gate signal. The logic is presented in Figure 3-28.

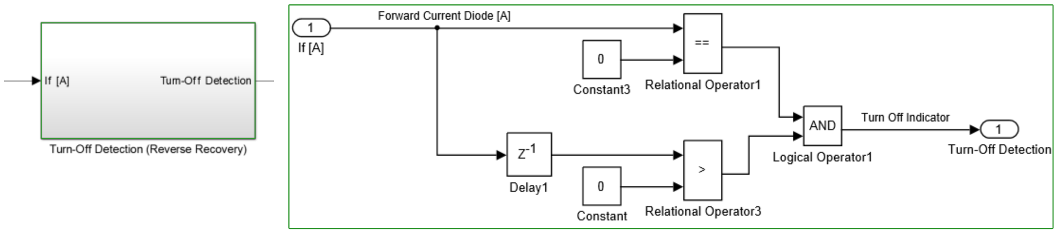

Figure 3-28 - MATLAB Simulink Model: Diode Turn-Off Logic

The turn-off indicator observes a turn-off event only if two events are successfully sensed:

1. The forward current i_f at simulation step “k” equals to zero,
2. The forward current i_f at the previous simulation step “k-1”.

The designed and implemented reverse recovery loss model is shown in Figure 3-29. This model only calculates the diode's energy loss when the turn-off detector records a turn-off event. The forward current must be delayed by one simulation step, since the turn-off detector reports the diode's turn-off with a delay of one simulation step. To ensure that the correct forward current value I_F, last value before turn-off, is used to compute the losses , the forward current must be delayed.

Since the losses are computed in Millijoules, a conversion to Joules is implemented at the loss model's output. Finally, before leaving the system a “fall-back” block has been inserted to ensure that only positive loss values will be produced. This last block is optional and was only added to protect the simulation model from possible errors, which might occur when the whole inverter model is simulated on a dynamic load; a traction motor for instance. The simulation output in the top right corner of Figure 3-29 proves that the loss model works as intended.

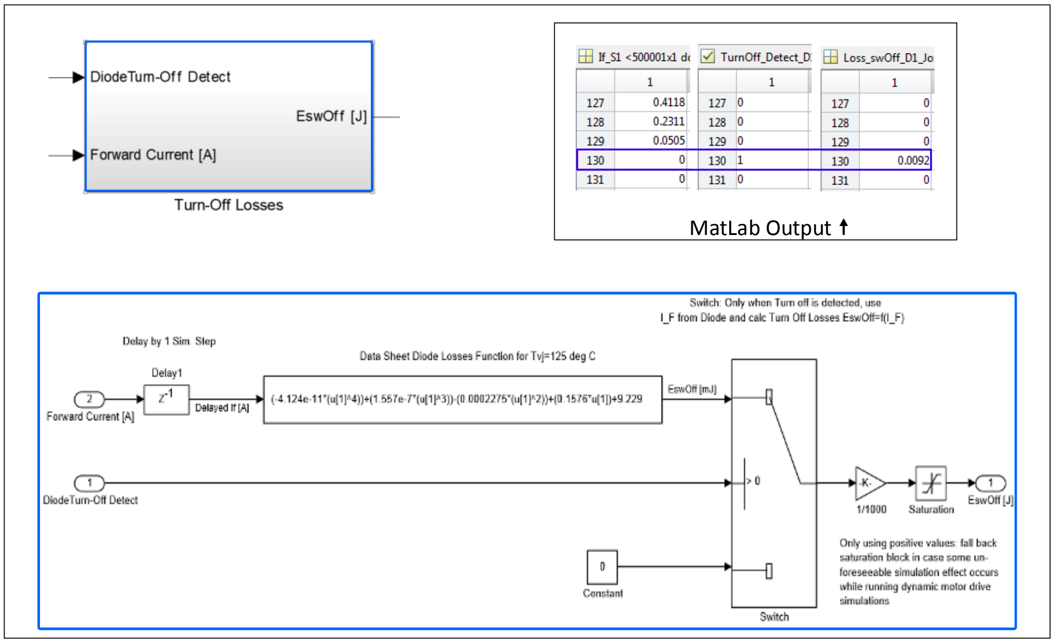

If_S1 <500001x1 d	1
127	0.4118
128	0.2311
129	0.0505
130	0
131	0

TurnOff_Detect_D	1
127	0
128	0
129	0
130	1
131	0

Loss_swOff_D1_Jo	1
127	0
128	0
129	0
130	0.0092
131	0

Figure 3-29 - MATLAB Simulink Model: Diode Reverse Recovery Losses

3.3 Inverter Efficiency Evaluation

At this point the inverter model is able to provide the desired output phase voltages and frequencies, allowing a three phase machine to operate at different speeds with its desired performance output. Furthermore, the inverter is now also capable to provide information on the losses that occur while the inverter operates. In this section, the motor drive model will be introduced and the inverter's efficiency map will be evaluated when controlling an electric machine. In this study the electric machine will be an axial flux permanent magnet (AFPM) motor.

3.3.1 Torque Controlled Motor Drive Model

The proposed Airbus A321 ETS powertrain demands that the motor drive needs to control the PMSM's output torque. Since the complete ETS powertrain model, which was introduced in chapter 2, sends a torque demand to the motor drive subsystem to match the drive cycle trajectory properly, the AFPM machine needs to be torque controlled. This in turn requires that the AFPM's output torque demand will be processed by the inverters SVPWM controller in order to control the inverter's switches in a way that the required machine performance can be achieved.

Since torque generation of PMSMs depends on motor parameters and the stator (phase) currents, the torque demand can be translated into a stator current reference. The inverter must then output phase output currents that are equivalent to the current references to ensure that the electric machine operates as demanded. A called "torque transducer" subsystem, shown in Figure 3-30, will convert the AFPM's output torque demand to a stator current request. This current reference can be processed by the inverter's SVPWM controller only if the input side of the controller will be modified slightly.

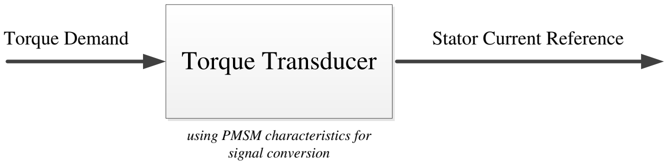

Figure 3-30 - Motor Drive Model: Torque - Stator Current Transducer

The previously introduced inverter model, and more precisely its SVPWM controller, requires a target phase voltage reference to ensure that the desired inverter output phase voltages can be produce. To allow the inverter model to operate as intended, a conversion from the stator current reference signal to a stator current voltage reference signal is required.

In electric machine controls it is common to not use the actual three phase stator current signal. Instead, a transformation from three phase quantities into a two phase representation is commonly used. The representation of three phase currents as two phase quantities has shown significant advantages when the motor's control complexity is considered. It also allows controlling the magnetic field and the torque generation of the PMSM separately from each other, which is highly desirable for PMSM control applications [74]. It was found that the stator currents can be expressed as two stationary (not oscillating) quantities. One quantity, called the quadrature axis current I_q, represents the torque generating part of the stator currents and the other quantity, which is referred to as the direct axis current I_d, describes the part of the stator currents that generate the magnetic field. This transformation is commonly declared as the Park transformation. A detailed description on the Park transformation which converters the three-phase oscillating stator current signal, represented in a stationary coordinate reference frame, to a two phase stationary current signal, represented in a rotating reference frame, is available in [99].

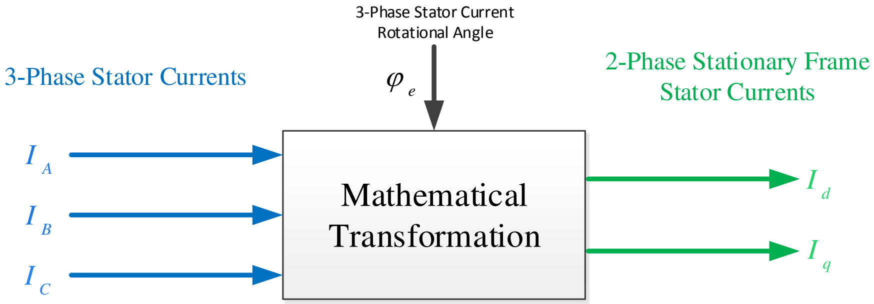

Figure 3-31 - Park Transformation Schematic

The convenience of using the two phase rotational frame representation for the PMSM stator currents, simply called dq representation, becomes directly apparent when the torque transducer system from Figure 3-30 is considered. Due to the separation of the stator currents in a torque and magnetic field generating component, the torque demand can be translated directly into a quadrature axis current I_q reference. This current reference can then be used to control the PMSM's output torque.

Equation (56) describes the motor's output torque T_e dependency on the d- and q-axis currents of the stator i_d, i_q [70].

$$T_e = \frac{3}{2} p \left[\lambda \cdot i_q + \left(L_d - L_q \right) i_d \cdot i_q \right] \tag{56}$$

When the motor is designed as a round rotor-type machine, which is the case for the proposed ETS AFPM machine, the second term in the torque equation will cancel out. The reason for this is that the d-and q-axis inductances for round rotor machines are equivalent ($L_d = L_q$) [100]. For reference the all AFPM system level specifications are listed in the Appendix section AFPM Machine Simulation Parameters.

Considering the AFPM motor's design, the output torque of the round rotor-type machine can be reduced to a proportional relationship to the stator's q-axis current i_q [74]:

$$T_e = \frac{3}{2}\, p\, \lambda \cdot i_q \ . \tag{57}$$

The variable p stands for the machine's number of pole pairs, for the given machine: $p = 5$, and λ stands for the flux linkage that is established by the rotor's permanent magnets as viewed from the phase windings of the stator [70]. Since p and λ are constant values, the torque output of the AFPM machine T_e will dependent linearly on the q-axis current i_q. Inserting equation (57) in the Torque Transducer subsystem block in Figure 3-30, allows translating any instantaneous demanded AFPM output torque into a required momentary q-axis current. The implemented PMSM's torque transducer is displayed in Figure 3-32.

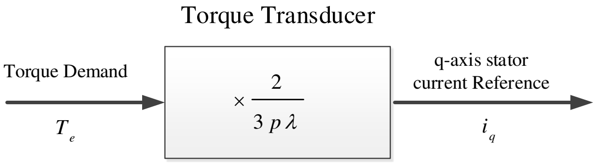

Figure 3-32 Torque to Q-Axis Current Transducer for PMSM Torque Control

At this point the characteristic PMSM's stator phase current relationship could be used to translate the q-axis and d-axis current references into their corresponding d,q-axis representations of the stator phase voltages v_A, v_B, v_C,which are denoted v_d and v_q.

$$v_d = R_s\, i_d + \frac{d}{dt}(L_d\, i_d + \lambda) - \omega_e\, L_q\, i_q \tag{58}$$

$$v_q = R_s\, i_q + \frac{d}{dt} L_q\, i_q + \omega_e (L_d\, i_d + \lambda) \tag{59}$$

Here, R_s is the stator phase resistance of the PMSM, L_d, L_q are the stator d,q-axis inductances, and ω_e denotes the electrical rotational speed of the stator phase currents in electrical radians per second. A more precise description on the equations above is available in [70] or any other appropriate literature on PMSM control and design.

However, this direct translation of the d,q-axis currents into respective PMSM stator phase voltage references, as it was presented in equations (58) and (59), is commonly not the preferred choice for accurate machine control. Such a control sequence would demand a certain voltage from the machine purely on the knowledge of a current reference input, but it would not be capable to assess if the stator currents actually manage to reach their desired reference. Such “open-loop” control systems, as they are called in control systems engineering, have the severe disadvantage of being unable to compensate any disturbances within the control system [101]. Applied to the motor control task of this controller, using an open loop torque control scheme, does not necessarily ensure that the AFPM motor can reach its performance demands.

Today, the translation of d,q-axis current reference signals into proper d,q-axis stator voltage references is done by feedback controllers, or closed loop controllers, which automatically output the needed d,q-axis voltage references to the SVPWM controller system. These closed-loop control systems overcome the disadvantages of open-loop systems and allow highly accurate control of the electric machine due to their sensitivity to disturbances [101].

For motor control applications the most common way to implement a feedback controller is by using a so called three-phase, or proportional-integral-derivative; short: PID, controller. An in-depth analysis on PID controllers and their operational principles is available in [101]. In the following only the general idea and the implementation of two similar PID controllers will be covered; one for d-axis current and the second for q-axis current control. It is important to mention that the PID controller for the d-axis and the q-axis current control will be exactly the same. Therefore, only the q-axis controller operational principles are described below.

Applied to the given application the PID controller is fed by the difference between q-axis reference current and actual q-axis current, which is supplied to the machine by the inverter's output phases. This difference is called the q-axis current tracking error e_q. Only if the q-axis current in the AFPM machine's stator i_{qPMSM} is equivalent to the demanded q-axis current i_{qRf}, the tracking error e_q will equal to zero. If $i_{qPMSM} \neq i_{qRef}$, then the error will be greater of smaller than zero. A deviation between the desired and the actual q-axis current exists, if the q-axis tracking error does not equal zero. The tracking error e_q is then put into the PID controller which in turn outputs a corresponding voltage reference signal V_{qRf}. This voltage reference signal interfaces with the SVPWM controller's input, allowing the three-phase voltage-source inverter to operate properly. Furthermore, the voltage reference V_{qRf} will ensure that the actual q-axis current, in the electric machines rotor I_{qPMSM}, matches with its momentary reference current I_{qRf}.

Figure 3-33 shows the representative control scheme for a q-axis feedback control. The d-axis current would be controlled similarly. In the full inverter model both, the q-axis and d-axis, reference voltages would be fed to the SVPWM controller of the inverter.

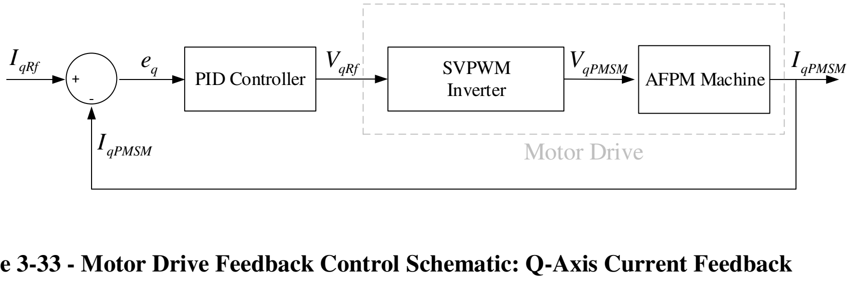

Figure 3-33 - Motor Drive Feedback Control Schematic: Q-Axis Current Feedback

By adding two equivalent PID controllers in front of the SVPWM control system, which then controls the three-phase inverter's switches as discussed previously, it is possible to create an adequate three phase voltage reference. The voltage reference signals ensure that the machine achieves the desired performance. Because of the closed loop current control, the inverter will be able to produce the required phase output currents, which will ultimately ensure that the right output torque will be generated.

At any time it should be remembered that the d,q-axis currents or voltages are simply a different representation of the respective three phase currents and voltages. The d,q-representation is only used to simplify the control of the desired AFPM machine.

The final motor drive control system, that has been created to realize torque control of the ETS AFPM machine, is outlined in Figure 3-34.

The presented torque controlled ETS motor drive model was realized in MATLAB Simulink by the use of a PMSM model from the Simulink/ Simscape/ SimPower Systems/ Machines library. All AFPM model parameters that were used in the PMSM model are listed in the Appendix section "AFPM Machine Simulation Parameters".

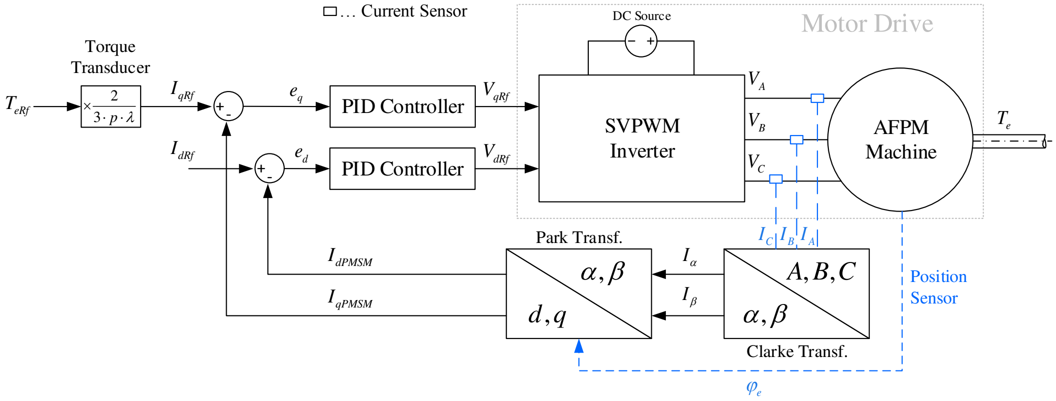

Figure 3-34 – MATLAB Simulink Model: Torque-controlled ETS Motor Drive

ETS Motor Drive Simulation Test

Before a reference torque can be implemented and a test simulation of the motor drive can be conducted, it is important to understand the relationship between an electric machine's output torque T_e and the corresponding change in rotational speed of its rotor ω_m.

For every electric machine the change in angular velocity $\frac{d}{dt}\omega_m$ depends on the sum of all applied rotor torques $\sum_i T_i$ and the magnitude of the rotor inertia J.

$$J\,\frac{d}{dt}\omega_m = \sum_i T_i \tag{60}$$

Applied to an electric machine that produces a torque output T_e that counteracts a load torque T_{load}, a Coulomb friction T_C and a viscous load torque T_v, one finds:

$$J\,\frac{d}{dt}\omega_m = T_e - Resistances$$

$$J\,\frac{d}{dt}\omega_m = T_e - (T_{load} + T_C + T_v)\,. \tag{61}$$

In cases where T_e is greater than all resistances, the machine will accelerate. This will be seen by a positive change in the rotor's angular velocity $\frac{d}{dt}\omega_m$. In cases where the resistances overcome the machine's output torque, the machine will decelerate, shown by a negative value for $\frac{d}{dt}\omega_m$. Finally, steady state rotation is reached when all resistances equal to T_e. Steady state in this context means that the electric machine will not increase its angular speed anymore; it keeps revolving with a constant angular velocity $\left(\frac{d}{dt}\omega_m = 0\right)$.

The MATLAB Simulink motor drive model assumed no Coulomb or viscous friction T_C, T_v; only the load torque was defined to control the speed of the machine. Therefore equation (61) could be reduced to:

$$J_{AFPM} \cdot \frac{d}{dt}\omega_m = T_e - T_{load} \ . \tag{62}$$

In order to run a test simulation where the rotor speed can be controlled, without allowing the machine to spin up to angular velocities that it cannot handle, the load torque T_{load} was implemented as a linear function that increases constantly until it reaches a user-defined angular velocity ω_{target}. At the target angular velocity, the load torque will equal the requested PMSM's output torque T_{eRf}.

$$T_{load} = \frac{T_{eRf}}{\omega_{target}} \cdot \omega_m(t) \tag{63}$$

Since the angular velocity $\omega_m(t)$ is not commonly used, equation (63) was rewritten in terms of the machine's rotational speed $n_m(t)$. This can be done, since the rotational speed is linearly dependent on the angular velocity; $\omega_m = 2\pi\, n_m$:

$$T_{load} = \frac{T_{eRf}}{n_{target}} \cdot n_m(t)\,. \tag{64}$$

This load torque equation was implemented into the simulation model as the AFPM machine's load. In a last step the motor drive model was tested to ensure its desired operation.

Motor Drive Simulation Test:

Simulation Parameter [Unit]	**Value / Description**
Simulation Time [s]	0.5
Fixed Step Solver Type	ode4 (Runge-Kutta)
Fixed Step Solver Step Size [-]	1e-6
Inverter Switching Frequency [Hz]	1e4
DC Bus Voltage Input to Inverter [V]	540 V_{DC}
Q-Axis reference Current [A]	Depending on Te reference (constant)
D-Axis reference current [A]	0
Te-Reference: T_e [Nm]	800 Nm (constant)
PID Gains: Kp-Ki (chosen for Model 08 PMSM from Simulink)	20-7500
Used PMSM Model for Test	ETS AFPM machine (see parameters in Appendix)
Motor Model Load Mechanical Torque (Tm) [Nm]	$T_{load} = \frac{T_e}{600\ rpm} \cdot Rotor\ Speed\ [rpm]$
Target Rotor Speed (due to Load Torque)	600 rpm

Load Torque System:

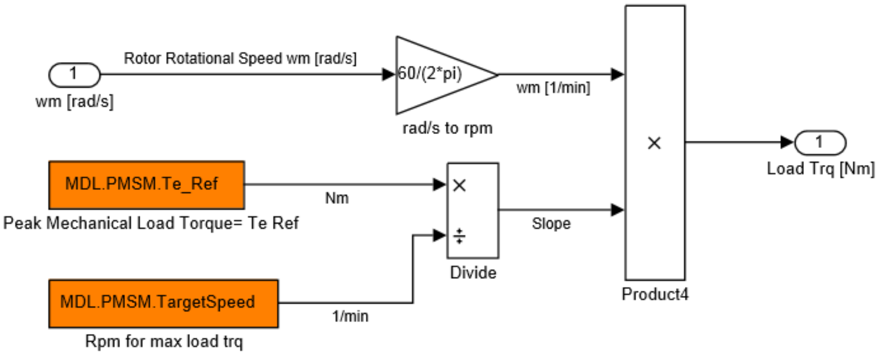

Figure 3-35 – MATLAB Simulink Model: PMSM Load Torque System

Results:

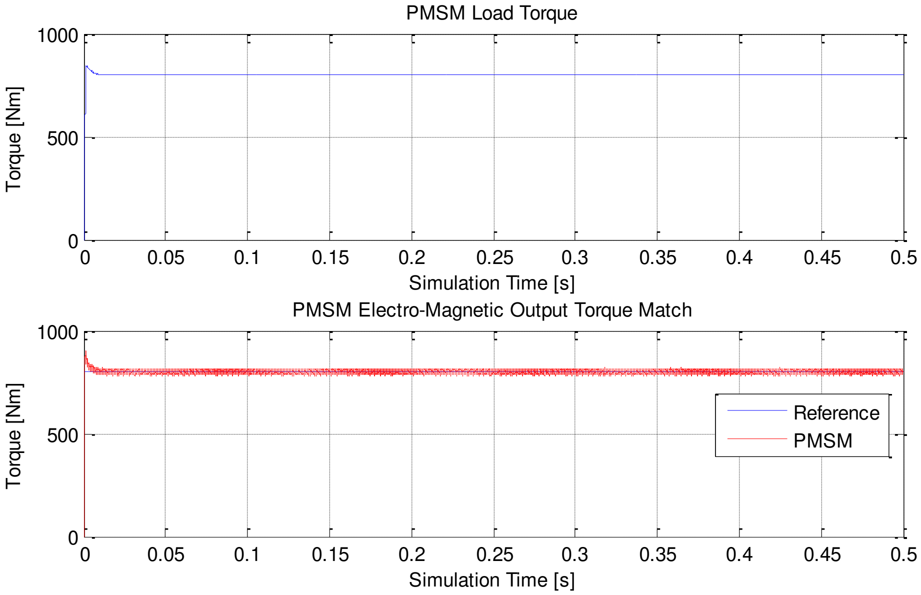

Figure 3-36 - ETS Motor Drive Simulation Results: Torque Match

Figure 3-36 and Figure 3-37 demonstrate that the designed ETS motor drive model operates as intended. The machine is supposed to operate at a constant torque of 800 Nm which is realized by the AFPM model. Additionally, the motor model is able to hold the demanded torque level while operating at a steady state target rotor speed of 600 rpm.

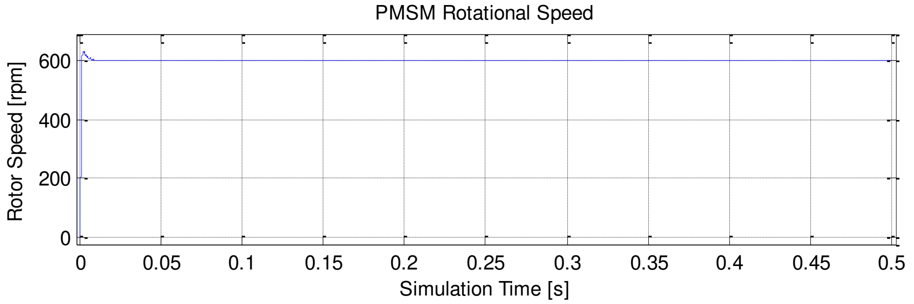

Figure 3-37 - Motor Drive Simulation Results: Rotor Speed [rpm]

A complete inverter loss evaluation calculated an average input power P_{in} of 52.113 kW, and a total inverter power loss $P_{LossTot}$, due to switching and conduction losses of the six IGBTs and anti-parallel diodes, of 1.442 kW.

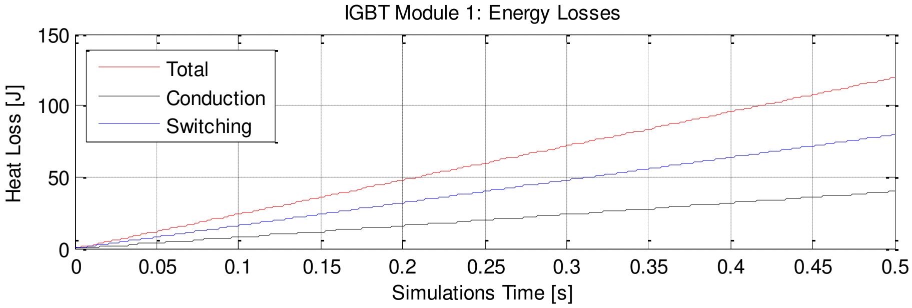

Figure 3-38 –Motor Drive Simulation Results: Inverter IGBT 1 Losses

As a result, the loss evaluation yielded an average inverter efficiency η_{avg} of 97.233 %.

$$\eta_{avg} = \left(1 - \frac{P_{LossTot}}{P_{in}}\right) 100\% = 97.233\ \%$$

This test demonstrates that the designed simulation model works as desired and that the inverter is capable to supply the machine with the correct current in order to produce an output torque equivalent to the reference torque. Furthermore, it demonstrates feasibility to determine reasonable high losses for a given machine's operating point; here 800 Nm torque output at a speed of 600 rpm.

3.3.2 Simulation-based Efficiency Map for ETS Inverter

The final step in the model based ETS inverter design is the evaluation of the system's efficiency map when controlling the target AFPM motor. An efficiency map can only be created when different PMSM output torque – rotor speed combinations are evaluated. One of these operating states, a certain speed at a given output torque, is also called "operating point" of an electric machine.

Thus, the final objective was the generation of an efficiency profile for all possible ETS AFPM machine's operating points.

An efficiency evaluation of the inverter requires the knowledge of the total inverters power loss P_{ILoss} and the input/ output power of the power converter P_{in}, P_{out}. Hence, the inverters input power needed to be calculated.

Since the current on the DC source side shows many ripples due to the frequent switching events that occur while the inverter operates, the input power P_{in} was determined on the basis of the input average current I_{inAvg} and the DC source voltage V_{DC} of the electrical energy storage system [68].

$$P_{inAvg} = V_{DC} \cdot I_{inAvg} \tag{65}$$

$$I_{inAvg} = \frac{1}{T} \int_{t_0}^{t_0+T} |i_{in}(t)| \, dt \tag{66}$$

The average inverter's power loss $P_{ILoss}$was calculated as the sum of all conduction E_{Lc} and switching energy losses E_{Lsw} divided by the respective loss evaluation time interval T. According to the Switching Device Loss Model section, the switching losses for the IGBT and the diode were already computed as energy losses in Joules. However, the conduction losses for the diode and the IGBT were determined as power losses. To converter the conduction power P_{Lc} to energy losses E_{Lc}, the power loss was integrated over the desired loss evaluation period T.

$$E_{Lc} = \int_{t_0}^{t_0+T} P_{Lc}(t) \, dt \tag{67}$$

Finally the total inverter's average power loss, within a chosen loss evaluation interval T, resulted in:

$$P_{ILoss} = \frac{E_{Lc} + E_{Lsw}}{T} \ . \tag{68}$$

The average efficiency for a chosen efficiency evaluation time window T was then determined by the following expression:

$$\eta_{avg} = \left(1 - \frac{P_{ILoss}}{P_{inAvg}}\right) 100\% \ . \tag{69}$$

It was found that the loss evaluation time T only delivers trusted efficiency numbers, when T is selected in a way that it analyses a multiple number $i = [1; 2; 3 \dots]$ of electrical cycles of the stator currents at a given rotor speed n_m. The electrical frequency n_e of the stator currents I_A, I_B, I_C is directly related to the instantaneous rotor speed n_m by multiplication of the electric machine’s pole pair number p. Therefore, the electrical frequency n_e of the stator currents is known for any machines operating point.

$$n_e = p \cdot n_m \tag{70}$$

With a pole pair number p of 5 for the given Axial Flux PMSM, equation (70) results in:

$$n_{elect} = 5 \cdot n_{mech} \tag{71}$$

This yield a period duration t_e for one electrical cycle of:

$$t_e = \frac{1}{n_e} \ . \tag{72}$$

Finally the desired loss evaluation time interval T can be obtained by multiplying a chosen integer i with the period duration for one electrical cycle of the stator currents t_e.

$$T = i \cdot t_e \tag{73}$$

For the efficiency evaluation $i = 5$ had been chosen, which means that five electrical cycles will be considered for the inverter’s loss calculation.

Efficiency Evaluation Time Example:

Assuming that the rotor spins at 600 rpm (n_m) and five electrical cycles ($i = 5$) should be evaluated, yields to the following results:

$$n_m = \frac{600 \frac{1}{min}}{60 \frac{s}{min}} = 10 \frac{1}{s} = 10\ Hz$$

$$n_e = 5\ \cdot n_m = 50\ Hz$$

$$t_e = \frac{1}{n_e} = \frac{1}{50 \frac{1}{s}} = 0.02\ s$$

$$T = 5 \cdot t_e = 0.1\ s\ .$$

The example above demonstrates that a time interval T of 0.1 seconds must be evaluated to analyze the efficiency of five electrical cycles in a machine spinning at constant 600 rpm.

An evaluation timing table for a majority of rotor speed operating points that were object of this efficiency evaluation, for a selected number of five electrical cycles evaluation time, is presented in the Appendix, Inverter Efficiency Evaluation Timing Table section.

ETS Inverter Efficiency Map

With the known evaluation times T and the presented load torque T_{load} model that allows to control the speed of the machine at a certain demanded reference torque T_e, the inverter’s efficiency map was calculated.

The motor designer supplied the peak torque-speed profile of the axial flux PMSM, which was used to define the maximum allowable torque T_{em} output of a machine for a chosen rotor speed n_m; the peak torque output versus rotor speed profile of the proposed AFPM machine is displayed in Figure 3-39.

In order to produce the efficiency map for the electric taxiing system's inverter that controls the AFPM motor, the load torque T_{load} equation was used to evaluate different machine torque outputs at fixed rotor speeds. Starting with a rotor speed of 100 rpm, the machine's output torque was continuously increased in 50 Nm increments until the AFPM's peak torque T_{em} for the given evaluation speed was reached; see torque-speed map in Figure 3-39. For a speed of 500 rpm the motor can produce up to 1215 Nm, but for higher speeds, such as 2500 rpm, the maximum available peak torque is less than 1215 Nm since the machine will operate in its maximum power region instead of its constant torque region.

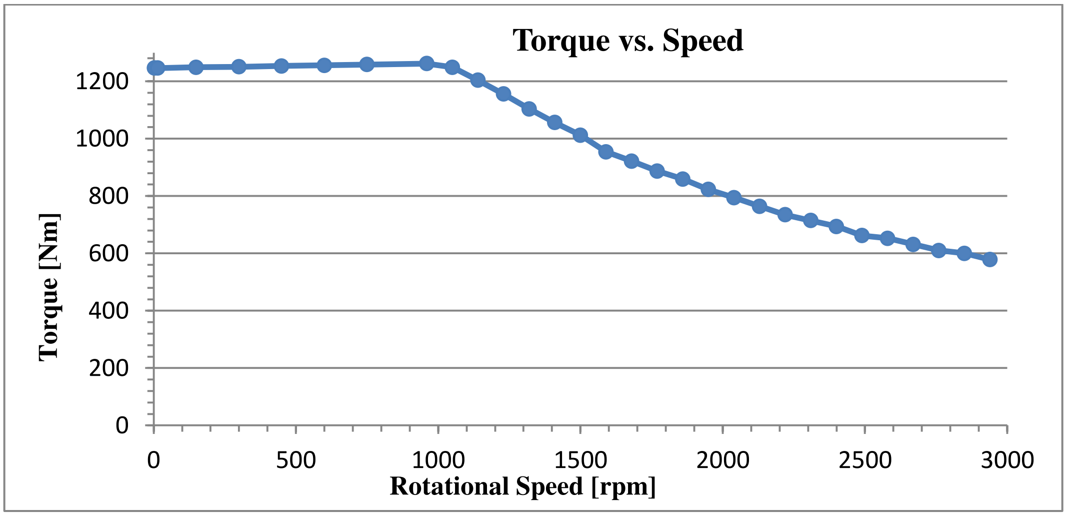

Figure 3-39 - ETS AFPM motor: Peak Torque versus Rotor Speed

Once the peak torque for a given speed was reached, the machine's speed was increased by a defined increment and the entire torque evaluation process was repeated. 100 rpm speed increments were selected to obtain a satisfactory efficiency map distribution.

For every single speed-torque combination a separate simulation was conducted and the inverters efficiency, while controlling the AFPM machine, was computed. In the end, a matrix was created where the efficiency results for every analyzed machine's operating point were stored. Between evaluation points, the efficiencies were interpolated linearly. The results of the efficiency evaluation for the ETS inverter, controlling the target AFPM machine, are presented in Figure 3-40.

A comparison with the three phase VSI efficiency map of the 2010 Toyota Prius, which was created on a real test bench setup by Oak Ridge National Laboratory [84], shows that the ETS inverter efficiency distribution and the range of efficiency magnitudes across the chosen PMSM's operating range appear realistic for a simulation based efficiency map prediction. The inverter efficiency map of the 2010 Toyota Prius is displayed in Figure 3-41 below.

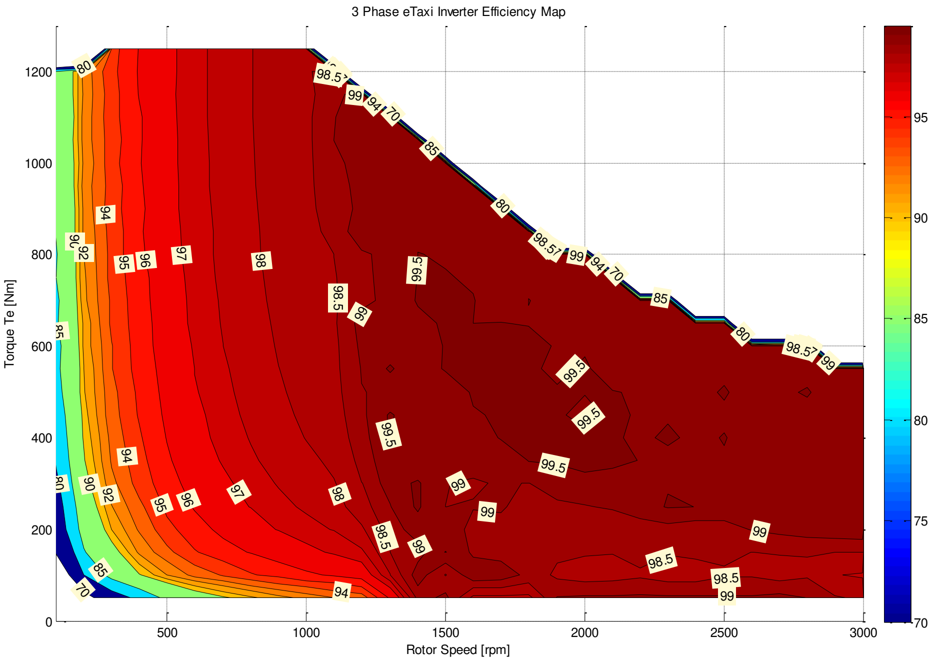

Figure 3-40 - ETS Inverter: Calculated Efficiency Map

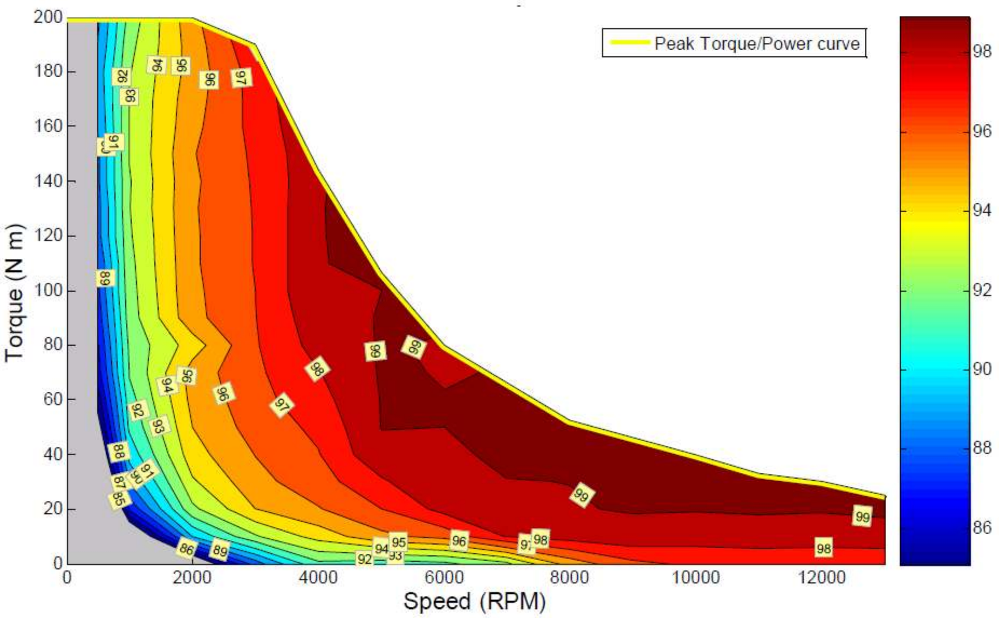

Figure 3-41 - 2010 Toyota Prius: Inverter Efficiency Map controlling a PMSM [84]

4 ETS POWER AND ENERGY MANAGEMENT ANALYSIS

In the former chapter a three-phase voltage source inverter (VSI) for the electric taxiing system was designed by the use of MATLAB Simulink. Furthermore, its efficiency map was derived by analyzing the total inverters power loss while controlling the target ETS AFPM machine.

As mentioned in the introduction of the former chapter, the possession of component specific efficiency maps allows implementing more realistic component behavior which yields more reliable powertrain simulation results. Applied to the scope of this study, the implementation of the inverters efficiency map will improve the top level ETS performance predications such as the energy consumption. In addition, it provides more accurate component specific information that support the subsequent design and building process of the actual component, i.e. heat loss distribution, operation points, average and peak performance numbers to only name a few.

Additionally to the implementation of the inverters efficiency map into the ETS powertrain simulation model, which was detailed in the Electric Taxiing System Sizing chapter, an estimated efficiency map for the desired AFPM machine was utilized as well. By implementing the inverter and the electric machine's efficiency maps into the simulation, a more realistic motor drive behavior will be incorporated into the ETS simulation model.

The efficiency map for the AFPM motor could only be estimated on the basis of a high performance axial flux PMSM, since the target ETS AFPM machine was still in the design finalization phase at the time where this project terminated. Therefore, no simulation based efficiency evaluation of the ETS traction motor was conducted.

The AFPM motor efficiency map estimation was done by scaling up an efficiency map from a high performance, high torque density axial flux permanent magnet machine from the UK-based company YASA motors [64]. The efficiency map of the YASA-400 motor was scaled up to the desired ETS motor performance specifications that were stated in Table 2-14 and Table 2-15. In numbers, the map was scaled to a peak torque of 1215 Nm, a top rotor speed of 2970 rpm and a peak power rating of 130 kW. The resulting efficiency map estimation for the Airbus A321 ETS traction motor is presented in Figure 4-1.

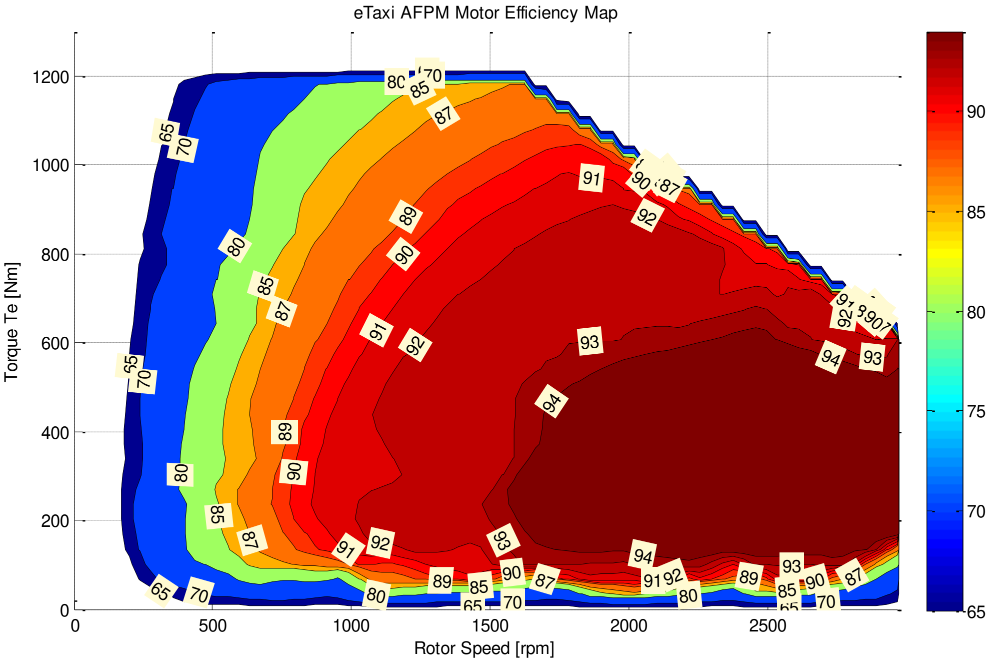

Figure 4-1 – ETS Traction Motor: Estimated Efficiency Map

With the inverter and the traction motors efficiency maps, the ETS powertrain simulations from the Electric Taxiing System Sizing chapter were repeated and the impact on the energy consumption of the powertrain due to the increased models fidelity was analyzed.

Revised ETS Powertrain Simulation Results

The revised powertrain model, with varying motor drive efficiencies, was again tested across every available drive cycle. The comparison with the two most demanding driving profiles in terms of peak power taxiing performance and maximum acceleration among all drive cycles, Hamilton TO 1 and Frankfurt TO 1, indicate that the ETS powertrain is still capable to meet the drive cycle performance demands; shown in Figure 4-2 and Figure 4-3. The drive cycle match with the Munich L1 driving profile is not displayed in this section, since this driving profile demands less challenging peak accelerations and less peak torque than the Hamilton and Frankfurt takeoff drive cycles. Because the ETS could not reach the top taxiing velocity of the Munich driving profile at the first simulation run, no improvements concerning the taxi top speeds can be expected due to the system's top speed limitation of 58 km/h.

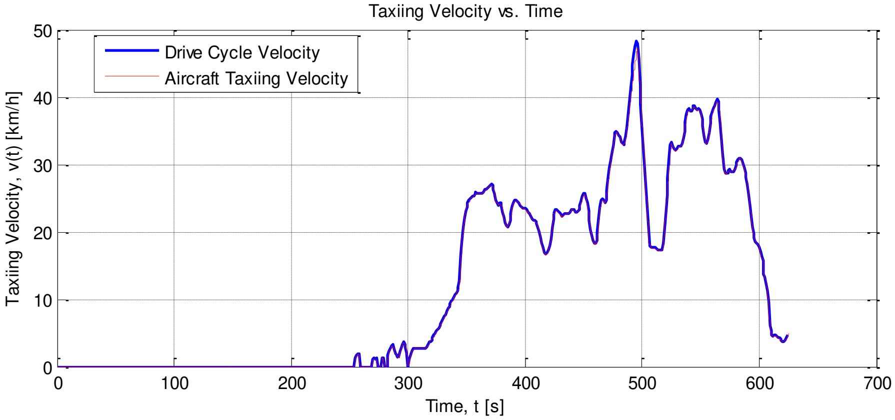

Figure 4-2 - Revised ETS Simulation Results: Frankfurt TO 1 Drive Cycle Match

The results for the total energy consumption and the regenerated energy across the three most demanding driving cycles- Munich L 1, Hamilton TO 1, and Frankfurt TO 1,- are listed in Table 4-1.

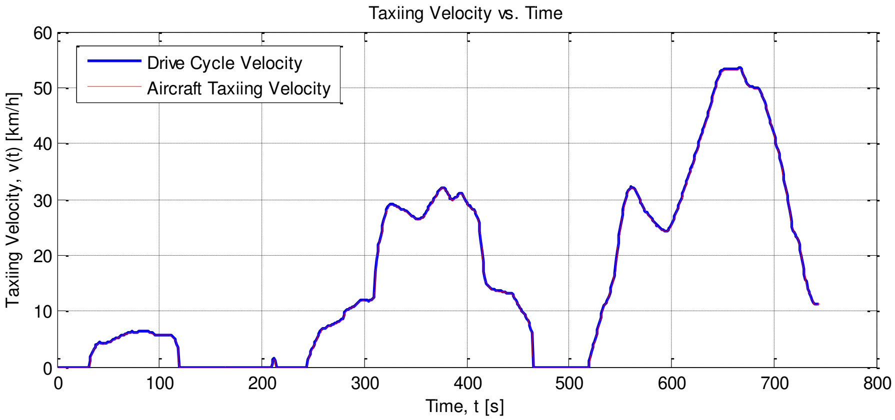

Figure 4-3 – Revised ETS Simulation Results: Hamilton TO 1 Drive Cycle Match

As it was mentioned previously, the time varying efficiency profiles, allow to estimate the motor drive losses more realistically. An example, of how the efficiency of the motor drive system varies with the simulation time, depending on the operation point of the motor drive system, for the Hamilton Takeoff 1 cycle, is displayed in Figure 4-4.

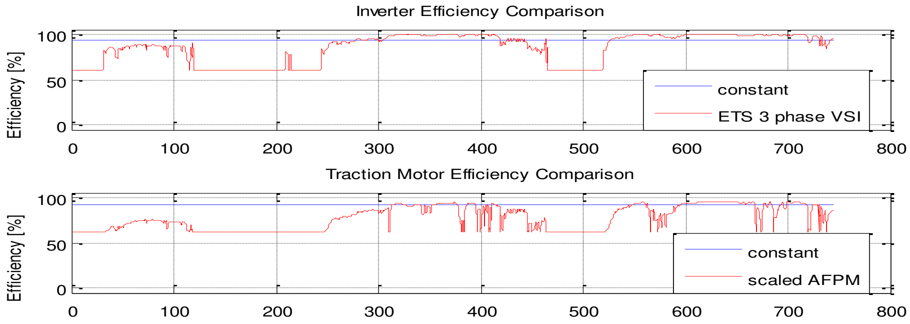

Figure 4-4 - Revised ETS Simulation Results: Hamilton TO 1 Motor Drive Efficiencies

From the simulation results it was found that the ETS motor drive system operates more efficient than the former assumed constant efficiency motor drive system when the powertrain operates at high speed taxi operations; where the traction machines rotor speed is above 1200 rpm. For low speed operations, rotor speed less than approximately 1000 rpm, the ETS operates less efficient than the initially assumed constant efficiency ETS powertrain. Therefore, the ETS will cause higher losses, which are dissipated as heat, under low speed operations. These findings can be justified by looking at the assumed traction motor and the inverter efficiency map, since both reveal high efficiency operation under high speed operating conditions.

Considering the simulation outcomes for the revised powertrain, that are presented in Table 4-1, it can be concluded that the initial simulation results for the constant efficiency ETS powertrain were already very close to the, at this point, more accurate simulation outcomes.

Table 4-1 –ETS Powertrain Results II: Using Motor Drive Efficiency Maps

Drive Cycle	**Energy Used [kWh]**	**Recovered Energy [kWh]**	**Energy Recovery [%]**	**RBF [%]**	**Average System Power [kW]**
Munich L 1	11.6	4.96	29.9	53	130.1
Frankfurt TO 1	8.05	2.69	25.1	88.3	46.4
Hamilton TO 1	10.89	1.53	12.3	99.3	52.6
Average of Takeoff Cycles	10.26	1.55	12.8	95.7	41.4
Average of Landing Cycles	6.37	2.66	27.5	72.1	83.6
Average of all Drive Cycles	9.89	1.66	14.2	93.4	45.4

The numbers for the ETS's energy consumption only increase slightly from 9.79 kWh to 9.89 kWh used energy, indicating that the initial guess on the inverter's and traction motor's constant efficiency was unexpectedly accurate for the given system and the available drive cycle profiles. A more accurate analysis on some noticeable differences between the initial ETS powertrain model and the revised model is presented in the following.

Takeoff Cycles:

When the results of all takeoff taxi missions are taken into account, it was detected that the revised ETS consumes 0.17 kWh more energy than the initial ETS, which equals to an energy consumption increase of 1.69 % compared to the former results. Even though the exact same amount of energy could be recovered, the energy used to move the aircraft has increased due to the implementation of a more realistic motor drive model into the powertrain simulation model. This yields finally to 0.2 % less energy recovery. The amount of regenerative braking compared to the total required braking power across all takeoff driving profiles could be almost maintained with the new powertrain model; 0.1 % lower RBF. Finally, the average system power could be reduced by 0.6 kW to 41.4 kW on average when compared to the previous average power result of 42 kW.

These results are very satisfying especially when the former statement on lower powertrain efficiencies at low speed ETS operations are factored in. Commonly, takeoff driving profiles show lower average speeds than landing taxi operations due to their frequent stop and go events while driving from the gate to the runway.

Landing Cycles:

Due to the higher average taxi speeds on landing cycles it was assumed that the revised ETS would improve the simulation results from the initial, constant efficiency ETS simulation model.

The simulation results confirm the expectations and provide improved energy consumption numbers, higher energy recovery numbers, and a lower average ETS power consumption.

The used energy was reduced by 0.56 kWh from 6.93 kWh to 6.37 kWh which equals a reduction in used energy on average of almost 8.1 % when compared to the initial prediction. The overall amount of recovered energy was improved by overall 0.8 %. This once again, shows the high potential of the energy recuperation even though the average RBF value decreased by 1.5 % from 73.6 % to 72.1 %. Additionally, the revised ETS was capable to cut the average electric taxiing power by almost 6.7 % from 89.6 kWh to 83.6 kW.

When all results are combined, it was shown that the implementation of a more realistic motor drive system achieved similar predictions for the energy use and energy recovery than the initial simulation model. The RBF decreased slightly by 0.2 % from 93.6 % to 93.4 % and the average electric power use across all drive cycles was decreased by 1.1 kW, which equals an average power reduction of almost 2.4 %, from 45.5 kW to 45.4 kW.

5 CONCLUSION AND DISCUSSION

This thesis addresses electric taxiing systems (ETSs) as one possible solution to improve modern aircraft on-ground operations. Such systems allow increasing the gate autonomy of modern planes, can reduce fuel consumption, and cut emissions, such as CO_2, NO_x, and noise, which could yield reduced operational costs and facilitate greener commercial aerospace operations.

An ETS is proposed that explores the upper performance envelope for modern electric taxiing systems for midsize aircraft's on ground operations. The presented system intends to deliver the same performance that was seen in multiple real conventional taxi operations between the years 2013, 2014, and 2015. A data set containing multiple GPS-recorded landing and takeoff driving profiles was used to size the ETS. The taxi system sizing process yields all major powertrain component specifications that are required to deliver an equivalent performance as it was seen by the recorded driving profiles. These component specific top level performance specifications can then be used as the input for further detailed component designs.

Based on these top-level ETS component ratings, a powertrain simulation model in MATLAB Simulink was developed to estimate the energy consumption of the predicted ETS.

In order to improve the validity of the ETS performance predictions the power converter, also referred to as the motor controller, was designed. The power converter is considered the center of the electric powertrain's energy management and was designed inside the physical modeling and simulation environment of MATLAB/ Simulink. Different design and topology considerations were discussed and the most appropriate solutions for the given application were selected to control a high torque, high power density permanent magnet machine (PMSM).

After the motor controller was developed and the desired operation of controlling the electric machine within the ETS powertrain was proven, a loss model for all occurring losses within the motor controller was developed. After the loss model demonstrated the desired loss predication capabilities, the loss model was used to evaluate the efficiency map of the power converter while controlling the target electric machine through its whole torque and rotational speed range.

In a final step, the derived motor controller efficiency map and an estimated, operating point dependent, efficiency profile for the ETS's traction machine were implemented into the previous, idealized ETS simulation model.

A revised analysis across all available real takeoff and landing taxi driving cycles showed that the initially predicted performance numbers could be refined slightly. Additionally, more accurate ETS performance predictions could be obtained with the integration of a more realistic motor drive behavior into the ETS powertrain simulation model.

5.1 Suggested Next Steps

Suggested next steps which could be undertaken to improve the proposed ETS powertrain model could be the development of a mechanical transmission model that inputs the delivered traction machine's output torque and the momentary rotor speed. It would be desirable that such model could predict transmission losses while operating in the proposed ETS powertrain.

Furthermore, a proper electrical energy storage system (ESS) could be selected that suits the power and energy requirements of the presented ETS. After such ESS topology selection it would be beneficial to create a characteristic loss model of this system. If applicable, an appropriate control algorithm for the energy storage system could be developed to ensure the desired and optimal operation of the energy source.

A final improvement of the simulation model could be accomplished by increasing the complexity of the aircraft's tire dynamics model. This model could also expand on modeling the rolling friction more accurately. In this case study a constant rolling friction was assumed to estimate the rolling friction's impact on the aircraft on-ground dynamics. In reality, the rolling friction depends on various factors such as the wheel speed, the tire pressure, the road conditions and the temperature, etc. [61] Thus, in order to increase the modeling complexity, more research could be conducted in the field to model the rolling friction more accurately as a dependent resistance on the aircraft's taxi velocity, the temperature, the tire pressure and further influencing factors.

Furthermore, the simulation results presented in this study can be further improved by implementing runway elevation data for the recorded driving profiles.

For validation purposes, it would be required to proceed with the individual electrical and mechanical component design for the inverter and axial flux PMSM. Once the designs were completed, a test bench efficiency evaluation is suggested as a logic next step to determine the actual efficiency maps of the proposed ETS powertrain components. This step would finally reveal the deviation between the predicated and the actual efficiency maps for the ETS motor drive system; including the inverter and the traction machine. A comparison of the predicated and actual efficiency profiles of the inverter would allow assessing the quality and accuracy of the self-derived easy-to-use loss model.

5.2 Discussion

A comprehensive electric taxiing system limitation and weight sensitivity analysis was already published in [51]. The following paragraphs will summarize the discussion points of this indicated publication and expand in certain selected areas.

Scope of this Thesis:

This thesis presents a case study on electric taxiing. It is not claimed that the ideal application for future ETSs is the integration in the MLG of a modern midsize aircraft such as the chosen Airbus A321 commercial airplane. The scope of this case study was to explore the upper performance envelope for modern and future ETSs to match modern conventional, main engine-based, taxiing. The study presents an insight in the system requirements definition process, the top level powertrain sizing procedure and presents a tool that can be used to estimate the energy consumption for any ETS topology; no matter what aircraft is selected and where the ETS is integrated. Additionally, it presents a model-based approach to obtain efficiency maps for power electronic converters due to an easy to use switching device loss model. Since the mechanical design as well as the integration of the proposed ETS was not part of this study, it remains to be seen if such a high performing ETS will actually be a viable option in the future.

Another important contribution of this presented work is the provision of real drive cycle data that can be used to design and size future ETSs.

ETS Application Limitation:

Electric taxiing systems will not be a viable option for every particular aircraft type due to the amount of mass that needs to be added to the existing aircraft. The longer a certain aircraft remains in the actual flight phase, the less beneficial becomes the implementation of an ETS due to the increased in-flight fuel consumption that results from the additional systems mass. Thus, it is required to carefully analyze the benefit of such a greener on-board taxi system to ensure that fuel consumption savings can be achieved. Studies on this topic were conducted and the general opinion as of today is that these novel ETSs are only usable for short-haul flight operations that are less than roughly three hours of flight duration. Electric taxiing systems are also only beneficial for aircraft that are no larger than single-aisle midsize airplanes such as the Airbus A320, A321 or the Boeing B737 to name a few prominent examples [19], [39], [102].

Regenerative Braking Limitations at Touchdown:

Regenerative braking capabilities of the ETS were only used for the taxi operation and no regenerative braking capabilities for the actual touchdown operation were considered. The reason for this was the studies scope, which attempted to move the aircraft completely independent of the main engines on the ground at speeds only up to 60 km/h. A system which uses electric traction motors that still provide the high torque capabilities, as they are required to taxi the aircraft on-ground, and also allow to recapture braking power at touchdown speeds of around 200 km/h are currently not available. Therefore a trade-off was made which resulted in focusing on the main goal of this project which was called independent electric taxiing of commercial midsize aircraft. Additionally, using the proposed system for touchdown energy recovery would dramatically increase the technical complexity of the motor drive design. Furthermore, critical and limiting factors for regenerative braking after touchdown might be the cooling requirements when recuperating braking power after touchdown as well as the energy storage system’s capability to capture large amounts of energy in a very short time. Also, high speed traction motor operations after touchdown might yield uncontrollable motor controller operating conditions due to the magnitude of generated back electromagnetic force (back EMF) as it is a function of the traction motors rotor speed. All these factors led to the decision to not consider regenerative braking during touchdown in this study.

ETS Weight Sensitivity:

Previously it was mentioned that the additional ETSs weight will influence the operating range of such system for the application in commercial aircraft. Indeed, the lighter such modern on-board propulsion systems are, the greater will be the impact on fuel savings and the application range; a lighter aircraft could then travel a greater distance while still achieving reductions in fuel consumption when compared to an operation without an on board ETS.

One thing which has not been taken into account in this study is effect of additional weight for structural supporting the proposed ETS in the chosen aircraft. A common rule of thumb assumes an additional kilogram of mass for structural supports for every kilogram that is being added to an aircraft. Assessing the actual systems mass of the proposed system, would allow to further improve the energy consumption predications.

An ETS weight sensitivity analysis for a smaller ETS system with a total estimated system mass of 800 kg was conducted in [51]. In this study the systems weight was modified by $\pm 25\,\%$ and the effect on the powertrain component specifications as well as the predicted energy consumption of the ETS across all available driving cycles was observed. It was found that the component specifications for the traction motor's peak power and the demanded energy storage system's peak power output changed by not even 0.3 %. The same findings applied to the predicated energy consumption which varied by less than 0.25 %. The weight sensitivity analysis demonstrated clearly that the predicted performance numbers and component ratings are almost unaffected by the ETS's mass. These findings can be understood if the total airplane's mass is compared to the mass of the proposed ETS. The chosen aircraft has a total estimated weight of above 90.54 tons compared to the ETS's mass of 1.14 tons as seen in Table 2-3. This indicates that the mass of the ETS accounts for less than 1.3 % of the selected plane's mass. With this little contribution on the total mass, the small effect of the ETS mass variation on the simulation results becomes apparent.

Motor Controller - Switch Loss Model Limitations:

Certainly the simplification of reducing the diode's as well as the IGBT losses to only one parameter, which in all cases was the current, will not allow an exact dynamic calculation of the actual losses of the chosen switching devices. When the scope of this study is considered, which is to design a powertrain model that mimics the real behavior of an electrical on-ground taxi propulsion system, the loss approximation based on the selected switch data sheet information yields reasonably close estimates of the real inverter's loss characteristics. Therefore, no transient loss model was developed by the author.

Additionally, the loss model did not implement a model for the instantaneous operating temperature. A constant operating temperature of 125 ˚C, which is close to the temperature rating of the chosen switching device, was selected to conservatively estimate the switching and conduction losses of the inverters switches. Even though these compromises were made, the loss model still achieved usable conservative loss predications and can be used as a convenient tool to estimate losses for any other power converter that makes use of semiconductor switching devices such as IGBTs, diodes and MOSFETs.

ETS Electric Machine Model:

In this case study, the traction and the generator operation of the electric machine simulation model were assumed to be equivalent; the curves follow the same torque-speed profile but in generator mode the profile will apply a torque with a reverse sign when compared to the traction torque. Such a model simplification of the motor model's behavior is a common choice for full powertrain models since the motoring and generating performance usually show similar absolute torque values for a given speed. However, in reality the absolute values of the motor's regenerative peak torque-speed profile will slightly differ from the traction torque-speed curve. This will ultimately impact the simulation outcomes and could therefore be improved in the proposed powertrain model.

Furthermore, this case study approximated the electric machine's efficiency map by the efficiency map of the YASA 400 AFPM machine from YASA motors [66]. To ensure that the performance parameters of the YASA 400 match the proposed motor characteristics, the YASA's efficiency map was scaled up to the desired performance; such as peak torque, peak power, rated speed and top speed. The efficiency profile of the actual target AFPM machine for the presented Airbus A321 ETS, which was designed in this research collaboration project, would show a different efficiency distribution. This different distribution would change the simulation outcomes, i.e. energy consumption, amount of recuperated energy from regenerative braking, etc. However, it was assumed that the YASA motor efficiency profile yields comparably high efficiencies as well as a good efficiency map approximation for the ETS motor that allow implementing a more realistic traction motor behavior when compared to a constant motor efficiency model.

ETS Power and Torque Ratings:

The presented system pushed for a high performance ETS which is above everything that has been published, tested, or proposed before. Naturally, such an ETS will be challenging to implement into existing aircraft which makes retro-fitting to existing midsize planes hardly possible. Furthermore, the mechanical, electrical and thermal design aspects were not executed. However, these design aspects are critical factors for the feasibility of the proposed ETS; especially the traction motor mechanical and thermal design. Additional design challenges include the planetary gearbox in the hub of the airplane’s main landing gear wheels, which is a very ambitious project that remains to be seen feasible.

Drive Cycle Altitude/ Elevation Data Limitation:

The energy consumption predications that were obtained from the powertrain simulations are ideal simulation outcomes which were produced for taxi operations of the ETS under dry conditions and perfectly flat ground (zero percent grade). Since no elevation was assumed, the simulation results can only serve as orientation results for the maximum achievable energy consumption under ideal braking energy regeneration. It was found that the taxiway elevation has the greatest influence on the energy consumption predications when compared to the two other motion resistances such as aerodynamic drag and rolling friction. Thus, the validity of the ETS performance predications can be increased by the implementation of accurate ground elevation profiles for the recorded driving profiles. However, the integration of such elevation profiles for each particular driving profile is not a simple task and requires a long lasting analysis as well as the access to an appropriate altitude data base. This resource must be available to provide accurate ground elevation numbers to the respective GPS positions across all airports where drive cycles were recorded. The complexity behind such process for the purpose of determining accurate ground elevation profiles for each drive cycle led to the decision to assume constant ground elevations for the complete ETS’s system simulation. However, the derivation of respective elevation data would be something to look into in the future to increase the energy consumption estimation accuracy.

Besides all the mentioned model limitations the author is confident that the presented work and the self-derived circuit-based ETS simulation tool provide valuable information and a solid foundation within the modern field of electric on-ground taxi systems. The provided resources can be used as a convenient starting point for future designs and for model development on different ETS powertrain architectures. The tools provided primarily target the application of supporting the early system and component design phase within a project to estimate the final systems behavior and derive accurate component design requirements.

REFERENCES

[1] M. Ehsani, Y. Gao and A. Emadi, Modern Electric, Hybrid Electric, and Fuel Cell VehiclesVehicles: Fundamentals, Theory, and Design, Second Edition, Boca Raton, FL, USA: CRC Press Taylor & Francis Group, LLC, 2009.

[2] United Nations, "Kyoto Protocol of the United Nationes Framework Convention on Climate Change," Kyoto, Japan, 1998.

[3] M. T. E. Heinrich, F. Kelch, P. Magne and A. Emadi, "Investigation of Regenerative Braking on the Energy Consumption of an Electric Taxiing System for a Single Aisle Midsize Aircraft," in *Industrial Electronics Society, IECON 2014 - 40th Annual Conference of the IEEE , vol., no., pp.3023,3029*, Dallas, TX, United States of America, Oct. 29, 2014-Nov.1, 2014.

[4] B. Bilgin and A. Emadi, "Electric Motors in Electrified Transportation: A step toward achieving a sustainable and highly efficient transportation system," *IEEE Power Electronics Magazine,* vol. 1, no. 2, pp. 10, 17, June 2014.

[5] B. Bilgin, P. Magne, P. Malysz, Y. Yang, V. Pantelic, M. Preindl, A. Korobkine, W. Jiang, M. Lawford and A. Emadi, "Making the Case for Electrified Transportation," *IEEE Transactions on Transportation Electrification,* vol. 1, no. 1, pp. 4, 17, June 2015.

[6] International Civil Aviation Organization, "ICAO Environment Report 2010," Environmental Branch of the International Civil Aviation Organization (ICAO), 2010.

[7] European Comission Directorate General for Mobility and Transport, "Flightpath 2050 - Europe's Vision for Aviation," Publications Office of the European Union, Luxembourg, 2011.

[8] A. Emadi, M. Ehsani and J. M. Miller, Vehicular Electric Power Systems: Land, Sea, Air, and Space Vehicles, New York: Marcel Dekker, ISBN: 0-8247-4751-8, December 2003.

[9] X. Roboam, B. Sareni and A. D. Andrade, "More Electricity in the Air: Toward Optimized Electrical Networks Embedded in More-Electrical Aircraft," *IEEE Industrial Electronics Magazine,* pp. vol. 6, no. 4, pp. 6,17, Dec 2012.

[10] CAST/ ICAO Common Taxonomy Team (CICTT), "Phases of Flight - Definitions and Usage Notes," April 2013. [Online]. Available: http://www.intlaviationstandards.org/. [Accessed April 2015].

[11] EGTS International, "EGTS Environmental Benefits (Overview)," Safran S.A. and Honeywell Aerospace, 2014.

[12] Airport Cooperative Research Program (ACRP), "Deriving Benefits from Alternative Aircraft-Taxi Systems," International Air Transport Association (IATA), Aircraft Taxiing Systems Conference, Cadmus Day 1 , Feb. 3, 2015.

[13] Delta Virtual Airlines, *Airbus A320 Aircraft Operations Manual (First Edition),* Global Virtual Airlines Group, August 31, 2009 .

[14] EGTS International, "EGTS Environmental Benefits (ENVISA Whitepaper)," Safran S.A. and Honeywell Aerospace, July 2014.

[15] J. A. Rosero, J. A. Ortega, E. Aldabas and L. Romeral, "Moving Towards a More Electric Aircraft," *IEEE A&E Systems Magazine,* p. ??, March 2007.

[16] C. Wenping, B. C. Mecrov, G. J. Atkinson, J. W. Bennett and D. J. Atkinson, "Overview of Electric Motor Technologies Used for More Electric Aircraft (MEA)," *IEEE Transactions on Industrial Electronics,* pp. vol. 59, no. 9, pp. 3523,3531,2360, Sept. 2012.

[17] A. Tenconi and P. W. Wheeler, "Introduction to the Special Section on The More Electric Aircraft: Power Electronics, Machines, and Drives," *IEEE Transactions on Industrial*

Electronics, pp. vol. 59, no. 9, pp. 3521,3522, Sept 2012.

[18] F. Re, "Viability and State of the Art of Environmentally Friendly Aircraft Taxiing Systems," in *Electrical Systems for Aircraft, Railway and Ship Propulsion (ESARS)*, vol., no., pp. 1,6, Oct. 2012.

[19] Honeywell Aerospace and Safran S.A., "egts - electric taxiing system (product brochure)," Safran/ Messier-Bugatti-Dowty and Honeywell Aerospace, June 2014.

[20] Lufthansa Technik AG, "Innovative TaxiBot now used in real flight operations (press release)," Lufthansa Technik AG, 20 02 2015. [Online]. Available: http://www.lufthansa-technik.com/. [Accessed 05 2015].

[21] TaxiBot, "TaxiBot Product Homepage," TaxiBot, 2013. [Online]. Available: http://www.taxibot-international.com/. [Accessed 05 2015].

[22] Lufthansa Technik AG, "For a green apron - Alternative mobility concepts for taxiing and towing of aircraft," Deutsche Lufthansa AG, [Online]. Available: http://www.lufthansa-technik.com/emobility. [Accessed 05 2015].

[23] TaxiBot, *Green Revolution in Airplane Taxiing - The only certified & operational alternative taxiing solution,* Product Brochure: Israel Aerospace Industries (IAI), 01/2015.

[24] Lufthansa LEOS, "Lufthansa LEOS signs development contract for eSchlepper," Luchthansa Technik AG, 09 10 2013. [Online]. Available: http://www.lufthansa-technik.com/. [Accessed 05 2015].

[25] Airbus, "Smarter Skies - Low Emission Ground Operations," Airbus S.A.S., 2015. [Online]. Available: http://www.airbus.com/innovation/future-by-airbus/smarter-skies/low-emission-ground-operations/. [Accessed 05 2015].

[26] Trace TowBots, "Trace Towbots Product Homepage," Trace Engines, 2015. [Online].

Available: http://www.tracetowbots.com/. [Accessed May 2015].

[27] United Labels, SE , "WheelTug Testy Praha 2010 (Online Video)," 20 January 2011. [Online]. Available: https://www.youtube.com/. [Accessed May 2015].

[28] WheelTug plc, "WheelTug Homepage," WheelTug plc, 2014. [Online]. Available: http://www.wheeltug.gi/. [Accessed May 2015].

[29] T. Raminosoa, T. Hamiti, M. Galea and C. Gerada, "Feasibility and Electromagnetic Design of Direct Drive Wheel Actuator for Green Taxiing," in *Energy Conversion Congress and Exposition (ECCE), 2011, IEEE, vol., no., pp.2798,2804*, Phoneix, AZ, USA, 17-22 Sept. 2011.

[30] WheelTug plc Youtube Channel, "WheelTug June 2012 Prague Tests (Online Video)," 5 July 2012. [Online]. Available: https://www.youtube.com/. [Accessed May 2015].

[31] Honeywell Aerospace and Safran/ Messier-Bugatti-Dowty, "Electric Green Taxiing System (EGTS) Homepage," Honeywell International Inc. and Safran S.A., [Online]. Available: http://www.greentaxiing.com/. [Accessed May 2015].

[32] Airbus S.A.S., "Airbus S.A.S. Homepage," 2015. [Online]. Available: http://www.airbus.com/. [Accessed March 2015].

[33] Magnet Motor GmbH, "Magnet Motor Aerospace Applications Homepage," L-3 Communications Magnet-Motor GmbH, 2015. [Online]. Available: http://www.magnet-motor.de/. [Accessed May 2015].

[34] M. Schier, F. Rinderknecht and H. Hellstern, "Electric Wheel Hub Motor for Aircraft Application," in *International Journal of Renewable Energy Research, IJRER, vol.1, no.4, pp.298-305*, 2011.

[35] Delos Aerospace, "Delos Aerospace Homepage," Delos Aerospace, L.L.C., 2011. [Online].

Available: http://delosaerospace.com/. [Accessed May 2015].

[36] S. Sullivan, "Method and Apparatus for Braking and Maneuvering". United States Patent US 2008/0179146 A1, 31 July 2008.

[37] S. Sullivan, "Landing Gear Method and Apparatus for Braking and Maneuvering". United States Patent US 7237748 B2, 3 July 2007.

[38] S. Sullivan, "Landing Gear Method and Apparatus for Braking and Maneuvering". United States Patent US 7226018 B2, 5 June 2007.

[39] A. Teo, K. Rajashekara, J. Hill and B. Simmers, "Examination of Aircraft Electric Wheel Drive Taxiing Concept," in *SAE Technical Paper 2008-01-2860*, Nov. 2008.

[40] International Air Transport Association (IATA), "New IATA Passenger Forecast Reveals Fast-Growing Markets of the Future (Press Release No.: 57)," 16 Oct. 2014. [Online]. Available: http://www.iata.org/. [Accessed May 2015].

[41] F. Kelch, "Investigation of System Requirements and Design of an Axial Flux Permanent Magnet Machine for an Electric Taxiing System for a Commercial Midsize Aircraft," M.A.Sc. thesis, Mechanical Engineering Department, McMaster University, Hamilton, Ontario, Canada, August 2015.

[42] R. Lopez, "Rival e-taxi developers stake their positions (article)," IHS, 7th May 2015. [Online]. Available: http://www.ihsairport360.com/. [Accessed June 2015].

[43] L-3 Magnet-Motor GmbH, "Green Taxi - Electric Drive for Aircraft Taxiing (Product Brochure)," 2015. [Online]. Available: http://www.magnet-motor.de/. [Accessed June 2015].

[44] AquipAviation, "Aircraft Spare Parts and Components - Goodyear Aircraft Tires Table," AquipAviation, 2013. [Online]. Available: http://www.aquipaviation.com/. [Accessed

November 2014].

[45] Lufthansa Technik AG, "Aircraft tires: More than just 'rubber on steel'," Lufthansa Technik, Germany, [Online]. Available: http://www.lufthansa-technik.com/. [Accessed November 2014].

[46] Airbus S.A.S., "A321/ Dimensions & key data," Airbus S.A.S., 2014. [Online]. Available: http://www.airbus.com/aircraftfamilies/passengeraircraft/a320family/a321/specifications/. [Accessed 07 11 2014].

[47] Airliners.Net, "Aircraft Data - The Boeing 737-500," Demand Media, Inc., 2014. [Online]. Available: http://www.airliners.net/. [Accessed 07 11 2014].

[48] Boeing, "Technical Characteristics - Boeing 747-400," Boeing, 2014. [Online]. Available: http://www.boeing.com/. [Accessed 07 11 2014].

[49] The Goodyear Tire and Rubber Company, "Aircraft Tire Data Book," Goodyear Aviation, Akron, OH, USA, October 2014. [Online]. Available: http://goodyearaviation.com/. [Accessed November 2014].

[50] A. A. Al roqi and W. Wang, "Torque of Rotating Device Prior an Airplane Landing," *International Journal of Engineering Research and General Science (IJERGS), vol. 2, issue 2,* pp. 214-222, Feb.-Mar, 2014.

[51] M. Heinrich, F. Kelch, P. Magne and A. Emadi, "Regenerative Braking Capability Analysis of an Electric Taxiing System for a Single Aisle Midsize Aircraft," *IEEE Transactions on Transportation Electrification (TTE),* p. Accepted for Publication (June 2015).

[52] U.S. DRIVE, "Electrical and Electronics Technical Team Roadmap," U.S. Department of Energy, June 2013.

[53] U.S. DRIVE, "Electrochemical Energy Storage Technical Team Roadmap," U.S.

Department of Energy, June 2013.

[54] P. Fajri, R. Ahmadi and M. Ferdowsi, "Equivalent Vehicle Rotational Inertia Used for Electric Vehicle Test Bench Dynamic Studies," in *IECON 2012 - 38th Annual Conference of the IEEE Industrial Electronics Society*, Montreal, QC, Canada, Oct. 25-28, 2012.

[55] The Goodyear Tire and Rubber Company, "Global Aviation Tires," Goodyear Aviation, Akron, OH, USA, Oct. 2014. [Online]. Available: http://www.goodyearaviation.com/.

[56] F. De Gernon, M. La Vecchia and A. Rigaldo, "Performance and Design of the Airbus A320 – Analysis of a Subsonic Aircraft," Department of Aerospace and Vehicle Engineering, Royal Institute of Technology, Stockholm, Sweden, Dec. 2009.

[57] MathWorks, "MathWorks Homepage," The Mathworks, Inc., 2015. [Online]. Available: http://www.mathworks.com/. [Accessed July 2015].

[58] The Engineering Toolbox, "Friction and Coefficients of Friction," [Online]. Available: http://www.engineeringtoolbox.com/. [Accessed 25 03 2014].

[59] K. Walus and Z. Olszewski, "Analysis of Tire-road Contact Under Winter Conditions," *Proceedings of the World Congress on Engineering (WCE 2011),* vol. III, no. ISBN: 978-988-19251-5-2, ISSN: 2078-0966 (Online), 2011.

[60] O. Grigore-Müller and M. Barbelian, "Regenerative braking for aircraft landing roll phase using an electric machine," in *Optimization of Electrical and Electronic Equipment (OPTIM), 2012, 13th International Conference, vol., no., pp. 584.593*, 24-26 May 2012.

[61] R. N. Jazar, Vehicle Dynamics - Theory and Application, 2nd Edition, New York: Springer New York Heidelberg Dordrecht London, 2014.

[62] Transport Canada - Air Navigation System Requirements Branch, "Aerodrome Standards and Recommended Practices - 4th Edition," March 1993, revised 03/2005. [Online].

Available: http://www.tc.gc.ca/. [Accessed 04 02 2014].

[63] W. Steinhiler and B. Sauer, Konstruktionselemente des Maschinenbaus 2 - Grundlagen von Maschinenelementen fuer Antriebsaufgaben (in German), 5th Edition, Kaiserslautern: Spinger-Verlag Berlin Heidelberg, ISBN-13 978-3-540-29629-4, 2005.

[64] YASA Motors Ltd., "YASA Motors Product Homepage," YASA Motors Ltd., Oxfordshire, UK, 2015. [Online]. Available: http://www.yasamotors.com/products/.

[65] GKN plc, "GKN eDrive Systems - eMachines," GKN plc, England, [Online]. Available: http://www.gkn.com/driveline/our-solutions/edrive-systems/eMachines/Pages/default.aspx. [Accessed 11 07 2014].

[66] YASA Motors Ltd., "YASA 400 - Axial Flux Electric Motor (Datasheet)," 2015. [Online]. Available: http://www.yasamotors.com/products/yasa-400/. [Accessed June 2015].

[67] A. Emadi, Advanced Electric Drive Vehicles, Boca Raton London New York: CRC Press, Taylor & Francis Group, 2014.

[68] D. W. Hart, Power Electronics, New York: McGraw-Hill, 2010.

[69] B. Ozpineci, *Introduction to Power Electronics - A Tutorial,* Oak Ridge National Laboratory, U.S. Department of Energy.

[70] D. Ward, I. Husain, C. Castro, V. Volke and M. Hornkamp, Bridging Theory into Practice - Fundamentals of Semiconductors for Hybrid-Electric Powertrain, Livonia: Infineon Technologies North America Corporation, 2013.

[71] Z. Yu, "Space-Vector PWM With TMS320C24x/F24x Using Hardware and Software Determined Switching Patterns (Application Report SPRA524)," Texas Instruments Incorporated, March 1999.

[72] J. F. Gieras, R.-J. Wang and M. J. Kamper, Axial Flux Permanent Magnet Brushless Machines (2nd Edition), ISBN 978-1-4020-6993-2: Springer Netherlands, 2008.

[73] S. Rafa, A. Larabi, L. Hocine and L. Barazane, "Control techniques for permanent magnet synchronous motor drive," in *Control & Automation (MED), 2010 18th Mediterranean Conference on , vol., no., pp.1115,1120*, Marrakech, 23-25 June 2010.

[74] Freescale, *Beyond Bits - Motor Control Edition (Issue 8),* Austin, TX, USA: Freescale Semiconductor, Inc., 2012, 2013.

[75] Y. Li and D. Gerling, "The Comparison of Control Strategies for the Interior PMSM Drive used in the Electric Vehicle," in *The 25th World Battery, Hybrid and Fuel Cell Electric Vehicle Symposium & Exhibition*, Shenzhen, China, Nov. 5-9, 2010.

[76] A. A. AbdElhafez and A. J. Forsyth, "A Review of More-Electric Aircraft," in *13th International Conference on Aerospace Sciences and Aviation Technology (ASAT)*, Military Technical College, Cairo, Egypt, May 26 - 28, 2009.

[77] J. Faucher, H. Piquet and N. Roux, "Analytical Approach of the AC-DC Interactions in Aerospace Electric Power Networks," *IEEE Transactions on Aerospace and Electronic Systems,* vol. 48, no. 2, pp. 1451, 1465, April 2012.

[78] A. Brockschmidt, "Electrical Environments in Aerospace Applications," in *Proceedings of the Electric Machines and Drives, 1999. International Conference IEMD '99*, pp. 719-721, Seattle, WA, USA, 1999.

[79] D. Wu, R. Todd and A. Forsyth, "Advanced energy management control for Energy Storage System," *7th IET International Conference on Power Electronics, Machines and Drives (PEMD 2014),* pp. 1, 6, April 2014.

[80] R. Todd, D. Wu, J. dos Santos Girio, M. Poucand and A. Forsyth, "Supercapacitor-based energy management for future aircraft systems," *Proceedings of the 2010 Twenty-Fifth Annual IEEE Applied Power Electronics Conference and Exposition (APEC),* pp. 1306,

1312, Feb. 2010.

[81] R. Todd and A. Forsyth, "HIL emulation of all-electric UAV power systems," *Proceedings of the IEEE Energy Conversion Congress and Exposition, 2009. ECCE 2009,* pp. 411, 416, Sept. 2009.

[82] T. A. Burress, C. L. Coomer, S. L. Campbell, L. E. Seiber, L. D. Marlino, R. H. Staunton and J. P. Cunningham, "Evaluation of the 2007 Toyota Camry Hybrid Synergy Drive System (ORNL/TM-2007/190)," Oak Ridge National Laboratory, Oak Ridge, Tennessee, United States of America, April 2008.

[83] Infineon Technologies, "Automotive IGBT Discretes," Infineon Technologies AG, 2015. [Online]. Available: http://www.infineon.com/. [Accessed May 2015].

[84] T. A. Burress, S. L. Campbell, C. L. Coomer, C. W. Ayers, A. A. Wereszczak, J. P. Cunningham, L. D. Marlino, L. E. Seiber and H. T. Lin, "Evaluation of the 2010 Toyota Prius Hybrid Synergy Drive System (ORNL/TM-2010/253)," Oak Ridge National Laboratory, Oak Ridge, Tennessee, United States of America, March 2011.

[85] AVL (Anstalt fuer Verbrennungskraftmaschinen List), "Universal Inverter," AVL List GmbH, 2015. [Online]. Available: https://www.avl.com/. [Accessed May 2015].

[86] BMW Group, "Power Electronics. Electric Boost Performance.," Bayerische Motoren Werke Aktiengesellschaft (BMW AG), 2015. [Online]. Available: http://www.bmwgroup.com/powertrain/en/electric_components/electronics.html. [Accessed June 2015].

[87] Infineon Technologies, "Products - Power - IGBT Homepage," Infineon Technologies AG, 2015. [Online]. Available: https://www.infineon.com/. [Accessed February 2015].

[88] Mitsubishi Electric, "Products - Semiconductors & Devices Homepage," Mitsubishi Electric Corporation, 2014. [Online]. Available: http://www.mitsubishielectric.com/. [Accessed

March 2015].

[89] Semikron, "Products - Product Classes - IGBT Modules Homepage," Semikron International GmbH, 2015. [Online]. Available: http://www.semikron.com/. [Accessed February 2015].

[90] International Rectifier, "Products- IGBTs Homepage," International Rectifier, 2015. [Online]. Available: http://www.irf.com/. [Accessed March 2015].

[91] IXYS Corporation, "Product Portfolio - Power Devices Homepage," IXYS Corporation, [Online]. Available: http://www.ixys.com/. [Accessed March 2015].

[92] Infineon Technologies, "FF600R12ME4C - EconoDUAL 3 IGBT module - data sheet," 5 November 2013. [Online]. Available: http://www.infineon.com/. [Accessed February 2015].

[93] Infineon Technologies, *Application Note AN 2008-02 V1.3 Feb. 2011 - Evaluation Driver Boards for EconoDUAL 3 and EconoPACK modules,* Warstein, Germany: Infineon Technologies AG, February 2011.

[94] D. Graovac and M. Puerschel, *IGBT Power Loss Calculation Using the Data-Sheet Parameters - Application Note, V 1.1,* Infineon Technologies AG, January 2009.

[95] Infineon Technologies AG, *Technical Information - IGBT Module - FF600R12ME4C (Data Sheet),* Infineon Technologies AG, 2013.

[96] Infineon Technologies AG, *ANIP9931E - Calculation of Major IGBT Operating Parameters,* Infineon Technologies AG, August 1999.

[97] A. Rohatgi, "WebPlotDigitizer," 2015. [Online]. Available: http://arohatgi.info/WebPlotDigitizer/. [Accessed 04 2015].

[98] MathWorks, *MATLAB Help Browser - MATLAB/ Data and File Management/ Data Import and Export/ Spreadsheets/ Read Microsoft Excel speadsheet file (xlsread),* The MathWorks,

Inc., 2012.

[99] Microsemi Corporation, "Park, Inverse Park and Clarke, Inverse Clarke Transformations MSS Software Implementation - User Guide (pdf document)," 2013. [Online]. Available: http://www.microsemi.com/. [Accessed October 2014].

[100] The MathWorks, Inc. , "MathWorks Help Library - Permanet Magnet Synchronous Machine," [Online]. Available: http://www.mathworks.com/help. [Accessed February 2015].

[101] N. S. Nise, Control Systems Engineering - 6th Edition, John Wiley & Sons, Inc., 2011.

[102] F. Re, "Assessing Environmental Benefits of Electric Aircraft Taxiing through Object-Oriented Simulation," *SAE International Journal of Aerospace,* vol. 5, no. 2, pp. 503-512, 2012.

APPENDIX

A. Drive Cycle Analysis Results

Conventional Taxiing - Drive Cycle Parameter				
Takeoff Cycles	max. Acceleration a_{max}[m/s²]	max. Velocity v_{max} [km/h]	Max. Traction Force F_{TM} [kN] net	Max. Traction Power P_{TM} [kW] net
London 1	0.75	48.102	68.4	268.96
Frankfurt 1	1.03	48.4	93.73	**584.77**
Berlin 1	0.445	30.703	40.6	260.7
Hamilton	**1.14**	53.602	**104**	494.2
Toronto 1	0.805	27.5	73.5	325.7
Toronto 2b	0.777	48.5	70.94	361.2
Toronto 3	0.5	28.7	45.77	165.29
Dallas 1	0.83	38.2	76.01	336
Calgary 1	0.95	45.1	86.4	286.1
Munich 1	0.42	46.2	38	382.33
Berlin 2	0.306	41.102	27.94	159.04
Toronto 4	0.445	32.3	40.62	196.31
Dallas 2a	0.42	**61.8**	38.1	227.22
Toronto 5	0.862	24.1	78.67	308.15
London 2	0.42	48.2	38.05	190.23
Berlin 3	0.39	44.9	35.47	181.14
Toronto 6	0.471	19.2	43	126.98
Washington 1	0.92	35.2	83.62	204.3
Berlin 4	0.389	33.3	35.47	128.84

Conventional Taxiing - Drive Cycle Parameter				
Landing Cycles	max. Acceleration a_{max}[m/s²]	max. Velocity v_{max} [km/h]	Max. Traction Force F_{TM} [kN] net	Max. Traction Power P_{TM} [kW] net
Berlin 1	0.278	24.3	25.4	117.7
Munich 1	**1.083**	**67.6**	**98.9**	363.54
Calgary 1	0.42	60.102	38	209.22
Vancouver 1	0.224	43.797	20.4	164.845
Vancouver 2	0.97	48.1	88.77	475.84
Dallas 1	0.86	35.2	78.47	366.13
Toronto 1	0.7	41.3	63.41	234.2
Frankfurt 1	0.916	52.4	83.6	499.4
Dallas 2	0.36	53.9	33.1	345.64
Toronto 2	0.5	67.4	45.6	**539.92**
London 1	0.584	45.4	53.3	102.73
Berlin 2	0.334	33	30.52	220.4
Brussels 1	0.252	51.3	22.985	212.75
Seattle 1	0.306	35.5	27.94	98.6
Frankfurt 2	0.39	32.4	35.47	179.35
Munich 2	0.139	43.1	12.68	147.24
Brussels 2	0.113	27.5	10.3	76.42

B. Switch Loss Model

Turn On and Turn Off Detection Analysis Results

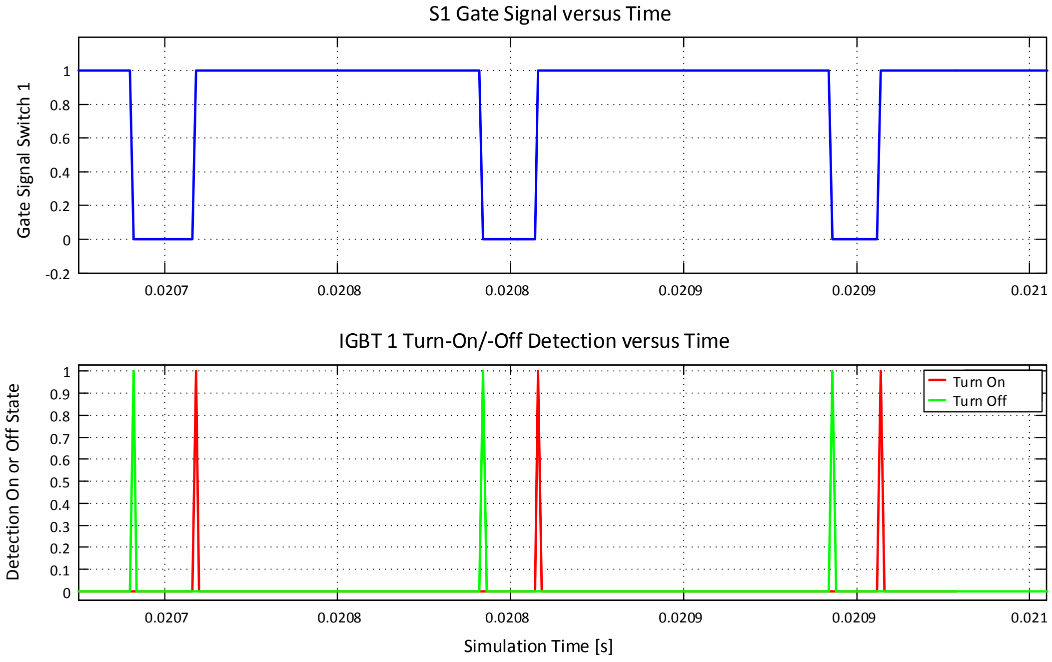
S1 Gate Signal versus Time

IGBT 1 Turn-On/-Off Detection versus Time

Figure 0-1 - IGBT Model - Turn On and Turn Off Detection for Switching Loss Calculation

Diode Conduction Losses (Voltage Drop Derivation)

Two points P_1, P_2 from the graph in Figure 3-24 for a virtual junction temperature of $T_{vj} = 125\ ℃$ within the targeted switches operational area $I_F =]0\ A\ ; 636.4\ A]$ had been picked. With these two points a linear function has been constructed that relates the diode's conduction voltage drop v_F to the momentarily forward current i_F.

The slope will be determined based off the two points P_1, P_2 that had been selected from the data sheet to digitalize the diode's forward characteristic.

$$P_1 = (V_{F1}, I_{F1}) = (1.167\ V, 175.829\ A)$$

$$P_2 = (V_{F2}, I_{F2}) = (1.564\,V, 403.318\,A)$$

Computing the slope r_{Dc}, also called diode conduction resistance, for within the targeted operational area:

$$r_{Dc} = \frac{\Delta\, V_F}{\Delta\, I_F} = \frac{V_{F2} - V_{F1}}{I_{F2} - I_{F1}}$$

$$r_{Dc} = \frac{1.564\,V - 1.167\,V}{403.318\,A - 175.829\,A} = 1.745 \cdot 10^{-3} \frac{V}{A}$$

The zero forward current voltage drop (x-axis intercept) was derived to be 0.86 V.

$$V_{F0} = 0.86\,V$$

With the x-axis intercept V_{F0} and the diode's conduction resistance r_{Dc} the desired mathematical expression for the diode's forward voltage drop v_F according to the instantaneous diode's forward current i_D can be established.

$$v_F = r_{Dc} \cdot i_F + V_{F0}$$

$$v_F = \left(1.745 \cdot 10^{-3} \frac{V}{A}\right) \cdot i_F + 0.86\,V$$

C. AFPM Machine Simulation Parameters

The parameters below are a summary of used AFPM machine system level specifications that have been obtained from the motor designer of the indicated electric machine. These parameters were implemented in the simulation PMSM model to derive the inverters efficiency map.

Table 0-1 - ETS Powertrain: Axial Flux Permanent Magnet Machine Specifications

Specification/ Parameter [unit]	Value
Motor Topology	AFPM
Detailed AFPM Topology	Yokeless and Segmented Armature
Peak Torque [Nm]	1215
Peak Power [kW]	130
Rated Speed [rpm] (point where maximum power is reached)	1022
Maximum Rotational Speed [rpm]	3000
Number of Stator Phases	3
Back EMF waveform	Sinusoidal
Rotor Type (round or salient pole)	Round
Stator Resistance [Ω]	$6.821 \cdot 10^{-3}$
Stator (Armature) Inductance [H]	$9.34 \cdot 10^{-4}$
Flux Linkage (established by magnets) [Vs]	0.48869 peak (rms: 0.365)
Pole Pair Number	5

Additional MATLAB Simulink parameters that were used to implement a corresponding AFPM (PMSM) model by utilization of the “Permanent Magnet Synchronous Machine” MATLAB Simulink model (Simscape/ SimPower Systems/ machines Library) are summarized in the table below.

Additional Simulation Parameters [unit]	**Value**
Configurations Tab	
Mechanical Input	Tm
Present Model	No
Parameters Tab	
Specify	Flux linkage established by magnets (V.s)
Inertia J [kg.m^2]	0.004
Viscous Damping F [N.m.s]	0 (has been neglect)
Static Friction Torque Tf [N.m]	0 (has been neglect)
Initial Condition wm [rad/s]	0
Initial Condition thetam [deg]	0
Initial Condition ia [A]	0
Initial Condition ib [A]	0
Advanced Tab	
Sample Time	-1 (inherited)
Rotor flux position when theta=0	Aligned with phase A axis (original Park)

D. PID Controller System (ETS Motor Drive Model)

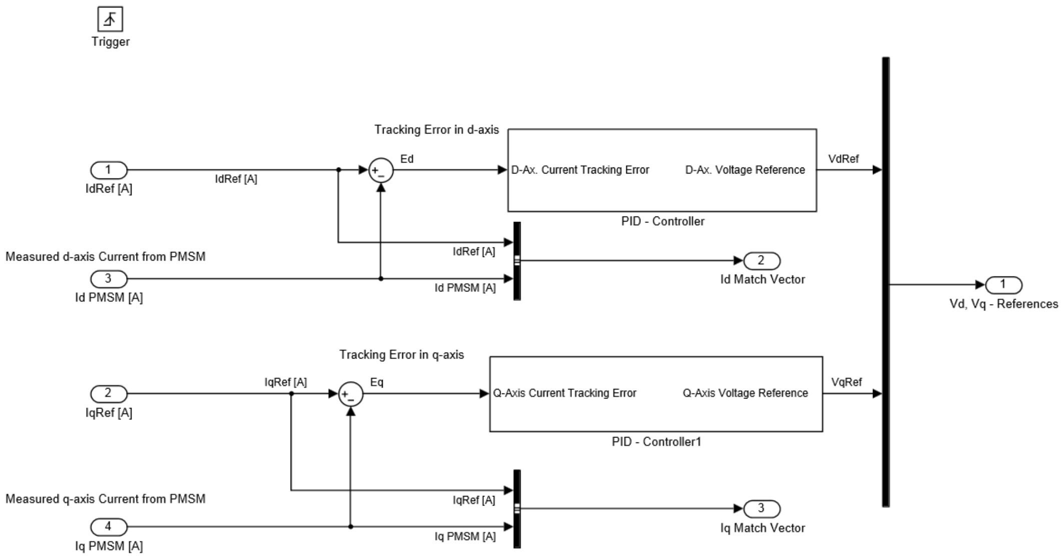

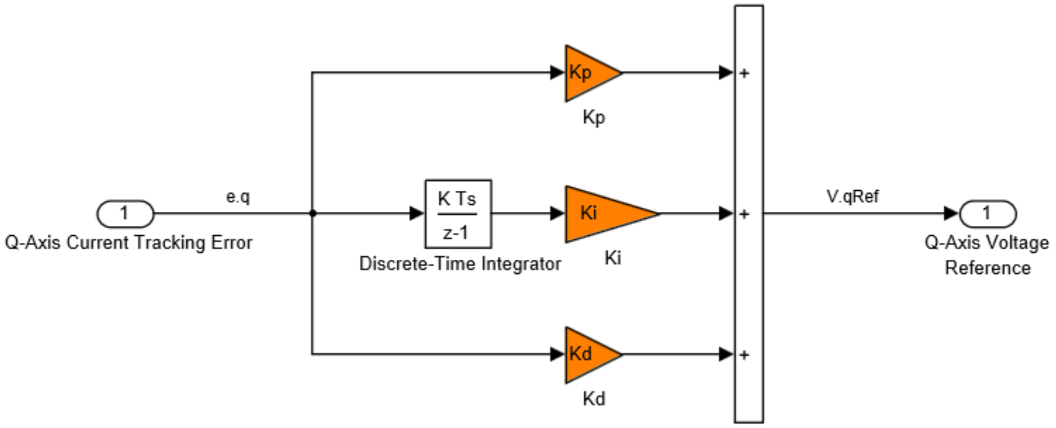

E. Inverter Efficiency Evaluation Timing Table

Rotor Speed Mech. n_m [rpm]	**Electrical Speed n_e [rpm]**	**Electrical Frequency n_e [Hz=1/s]**	**Electrical Cycle Period Time t_e [s]**	**Evaluation Time Interval T [s]**
100	500	8.3	0.12	0.6
200	1000	16.7	0.06	0.3
300	1500	25	0.04	0.2
400	2000	33.3	0.03	0.15
500	2500	41.7	0.024	0.12
600	3000	50	0.02	0.1
700	3500	58.3	0.017142857	0.085714286
800	4000	66.7	0.015	0.075
900	4500	75	0.013333333	0.066666667
1000	5000	83.3	0.012	0.06
1100	5500	91.7	0.010909091	0.054545455
1200	6000	100	0.01	0.05
1300	6500	108.3	0.009230769	0.046153846
1400	7000	116.7	0.008571429	0.042857143
1500	7500	125	0.008	0.04
1600	8000	133.3	0.0075	0.0375
1700	8500	141.7	0.007058824	0.035294118
1800	9000	150	0.006666667	0.033333333
1900	9500	158.3	0.006315789	0.031578947
2000	10000	166.7	0.006	0.03
2100	10500	175	0.005714286	0.028571429
2200	11000	183.3	0.005454545	0.027272727
2300	11500	191. 7	0.005217391	0.026086957
2400	12000	200	0.005	0.025
2500	12500	208.3	0.0048	0.024
2600	13000	216.7	0.004615385	0.023076923
2700	13500	225	0.004444444	0.022222222
2800	14000	233.3	0.004285714	0.021428571
2900	14500	241. 7	0.004137931	0.020689655
3000	15000	250	0.004	0.02